

AD-A201 606

DTIC FILE COPY



② ARO 25544.3-EG

Brown University

DIVISION OF ENGINEERING

PROVIDENCE, R.I. 02912

DTIC  
ELECTE  
S OCT 20 1988 D  
E

This document has been approved  
for public release and sale its  
distribution is unlimited.

88 10 20 009

**THE EFFECTS OF TEMPERING AND  
TEST TEMPERATURE ON THE  
DYNAMIC FRACTURE INITIATION  
BEHAVIOR OF AN AISI 4340 VAR STEEL**

by

**Y.C. Chi, S.H. Lee, K. Cho, and J. Duffy  
Division of Engineering, Brown University  
Providence, R.I. 02912**

Army Research Office  
ARO Contract No. DAAL03-88-K-0015  
Report No., 2

Materials Research Laboratory  
Brown University  
August, 1988

**DTIC  
ELECTE  
S OCT 20 1988 D  
E**

This document has been approved  
for public release and sale; its  
distribution is unlimited.

## REPORT DOCUMENTATION PAGE

1a. REPORT SECURITY CLASSIFICATION <b>Unclassified</b>		1b. RESTRICTIVE MARKINGS	
2a. SECURITY CLASSIFICATION AUTHORITY		3. DISTRIBUTION/AVAILABILITY OF REPORT  Approved for public release; distribution unlimited.	
2b. DECLASSIFICATION/DOWNGRADING SCHEDULE		5. MONITORING ORGANIZATION REPORT NUMBER(S)  <b>ARO 25544.3-EG</b>	
4. PERFORMING ORGANIZATION REPORT NUMBER(S)  #2		7a. NAME OF MONITORING ORGANIZATION  U. S. Army Research Office	
6a. NAME OF PERFORMING ORGANIZATION  BROWN UNIVERSITY		7b. ADDRESS (City, State, and ZIP Code)  P. O. Box 12211 Research Triangle Park, NC 27709-2211	
6b. OFFICE SYMBOL (if applicable)		9. PROCUREMENT INSTRUMENT IDENTIFICATION NUMBER  <b>DAAL03-88-K-0015</b>	
8a. NAME OF FUNDING/SPONSORING ORGANIZATION  U. S. Army Research Office		10. SOURCE OF FUNDING NUMBERS	
8b. OFFICE SYMBOL (if applicable)		PROGRAM ELEMENT NO.	PROJECT NO.
8c. ADDRESS (City, State, and ZIP Code)  P. O. Box 12211 Research Triangle Park, NC 27709-2211		TASK NO.	WORK UNIT ACCESSION NO.
11. TITLE (Include Security Classification)  "The Effects of Tempering and Test Temperature on the Dynamic Fracture Initiation Behavior of an AISI 4340 VAR Steel"			
12. PERSONAL AUTHOR(S)  Y.C. Chi, S.H. Lee, K. Cho, and J. Duffy			
13a. TYPE OF REPORT  Technical		13b. TIME COVERED FROM TO	
14. DATE OF REPORT (Year, Month, Day)  August 1988		15. PAGE COUNT  88	
16. SUPPLEMENTARY NOTATION  The view, opinions and/or findings contained in this report are those of the author(s) and should not be construed as an official Department of the Army position policy or decision, unless so designated by other documentation.			
17. COSATI CODES		18. SUBJECT TERMS (Continue on reverse if necessary and identify by block number)	
FIELD	GROUP	SUB-GROUP	
			fracture, dynamic effects,
			4340 VAR steel, temperature effects,
			fracture toughness, microstructural effects. J2
19. ABSTRACT (Continue on reverse if necessary and identify by block number)  An investigation was conducted into the effect of tempering, test temperature and loading rate on the fracture initiation behavior of an AISI 4340 VAR steel. The fracture initiation tests were conducted by stress wave loading of a prefatigued circumferential crack in a notched round bar. The geometry provides for plane strain conditions at the fracture site, and the instrumentation gives records of average stress at the fracture site and of crack opening displacement, both as functions of time. A stress intensity rate, $\dot{K}_I$ , of about $2 \times 10^6$ MPa m s <sup>-1</sup> is attained by this technique, and a comparison is presented with results obtained in static loading with the same geometry. Finally, the dynamic and quasi-static stress-strain behavior in shear was determined by loading <sub>3</sub> a thin-walled <sub>4</sub> tube specimen in a torsional Kolsky bar. The strain rates were $\dot{\gamma} = 10^3$ sec <sup>-1</sup> and $\dot{\gamma} = 10^4$ sec <sup>-1</sup> . In addition, Charpy specimens of the various tempers were tested. Tempered martensite embrittlement was observed in the Charpy specimens of 350°C temper.  (cont. on other side)			
20. DISTRIBUTION/AVAILABILITY OF ABSTRACT  <input type="checkbox"/> UNCLASSIFIED/UNLIMITED <input type="checkbox"/> SAME AS RPT. <input type="checkbox"/> DTIC USERS		21. ABSTRACT SECURITY CLASSIFICATION  Unclassified	
22a. NAME OF RESPONSIBLE INDIVIDUAL  J. Duffy		22b. TELEPHONE (Include Area Code)   22c. OFFICE SYMBOL	

UNCLASSIFIED

SECURITY CLASSIFICATION OF THIS PAGE

Block #19 (continued)

However, in the plane strain fracture initiation test the embrittlement trough was observed only in tests conducted below room temperature. Extensive quantitative fractography was performed on the plane strain fracture specimens to identify the dominant mode of fracture initiation for each temper at the different rates and test temperatures.

Accession For	
NTIS GRA&I	
DTIC TAB	
Unannounced <input type="checkbox"/>	
Justification	
By	
Distribution/	
Availability Codes	
Dist	Avail and/or Special
A-1	



August, 1988

The Effects of Tempering and Test Temperature on the  
Dynamic Fracture Initiation Behavior of an AISI 4340 VAR Steel

by

Y.C. Chi<sup>1</sup>, S.H. Lee<sup>2</sup>, K. Cho<sup>3</sup>, and J. Duffy<sup>4</sup>**ABSTRACT**

An investigation was conducted into the effect of tempering, test temperature and loading rate on the fracture initiation behavior of an AISI 4340 VAR steel. The fracture initiation tests were conducted by stress wave loading of a prefatigued circumferential crack in a notched round bar. The geometry provides for plane strain conditions at the fracture site, and the instrumentation gives records of average stress at the fracture site and of crack opening displacement, both as functions of time. A stress intensity rate,  $\dot{K}_I$ , of about  $2 \times 10^6 \text{ MPa}\sqrt{\text{m}} \text{ s}^{-1}$  is attained by this technique, and a comparison is presented with results obtained in static loading with the same geometry. Finally, the dynamic and quasi-static stress-strain behavior in shear was determined by loading a thin-walled tube specimen in a torsional Kolsky bar. The strain rates were  $\dot{\gamma} = 10^3 \text{ sec}^{-1}$  and  $\dot{\gamma} = 10^{-4} \text{ sec}^{-1}$ . In addition, Charpy specimens of the various tempers were tested. Tempered martensite embrittlement was observed in the Charpy specimens of 350°C temper. However, in the plane strain fracture initiation test the embrittlement trough was observed only in tests conducted below room temperature. Extensive quantitative fractography was performed on the plane strain fracture specimens to identify the dominant mode of fracture initiation for each temper at the different rates and test temperatures.

<sup>1</sup> Research Assistant, Division of Engineering, Brown University.

<sup>2</sup> Assistant Professor, Department of Materials Science, Pohang Institute of Science & Technology, Korea. Formerly Research Associate, Brown University.

<sup>3</sup> Research Associate, Division of Engineering, Brown University

<sup>4</sup> Professor of Engineering, Division of Engineering, Brown University, Providence, RI 02912

## TABLE OF CONTENTS

<b>I. INTRODUCTION</b> . . . . .	<b>4</b>
<b>II. DESCRIPTION OF EXPERIMENTS</b> . . . . .	<b>7</b>
II.1 Material . . . . .	7
II.2 Fracture Specimens. . . . .	7
II.3 Description of the Fracture Initiation Experiment . . . . .	8
(a) Dynamic Tests . . . . .	8
(b) Quasi-Static Tests . . . . .	11
(c) Measurement of Displacement in the Dynamic Fracture Test by means of MTI Photonic Sensor . . . . .	12
II.4 Static and Dynamic Stress-Strain Behavior . . . . .	13
II.5 Metallography and Microscopy . . . . .	15
II.6 Determination of Void Initiation Strains. . . . .	15
<b>III. RESULTS AND DISCUSSION</b> . . . . .	<b>16</b>
III.1 Stress-Strain Behavior in Shear . . . . .	16
III.2 Charpy Impact Toughness . . . . .	19
III.3 Plane Strain Fracture Initiation Toughness . . . . .	20
III.4 Microstructure . . . . .	26
III.5 Void Initiation Strains. . . . .	32
III.6 Fracture Model. . . . .	33
<b>IV. CONCLUSIONS.</b> . . . . .	<b>38</b>
<b>V. REFERENCES.</b> . . . . .	<b>41</b>
<b>VI. TABLES AND FIGURES</b> . . . . .	<b>44</b>

## I. INTRODUCTION

This report presents a study of dynamic fracture initiation toughness and dynamic stress-strain behavior of an AISI 4340 VAR (vacuum arc remelted) steel of three different tempers tested over a range of temperatures. In the experiment an explosive charge is detonated to produce a tensile stress wave to initiate the fracture. The recorded data allows for a calculation of  $K_{Id}$ , the critical dynamic stress intensity factor of the material. Results are compared with corresponding quasi-static values and with results obtained by other investigators.

AISI 4340 steel is a widely used martensitic low-alloy steel that provides an advantageous combination of strength, ductility, and toughness. By subjecting this steel to a vacuum arc remelt process the concentration of sulfur and phosphorus, which are detrimental to fracture toughness, are reduced. Furthermore, different tempers can be employed to transform the martensite to cementite and ferrite, and to lower the yield stress and hardness of the steel. As the yield stress drops, the fracture toughness increases making it possible to produce a steel with a very high yield stress and high hardness, and yet preserving some ductility.

The fracture initiation tests described in the present report were performed by stress wave loading of a prefatigued circumferential crack in a notched round bar. The technique was introduced at Brown University in 1977 [1] and has been employed since in a number of investigations [2,3,4]. Stress wave loading has also been employed by other investigators using specimens of similar geometry [5] or employing single-edged-notched strip specimens [6]. It provides for a stress intensity rate,  $\dot{K}_I$  of about  $2 \times 10^6 \text{ MPa}\sqrt{\text{m}} \text{ s}^{-1}$ , which is somewhat faster than attained in the Charpy test. However, the principal advantages of the present technique over the Charpy test lie elsewhere. For instance, it provides accurate measures of the average stress at the

fracture site and of crack opening displacement, both as functions of time. These results in turn can be interpreted to give a reliable value of  $K_{Id}$  at the instant of fracture initiation, or of  $J_{Id}$  for a more ductile fracture [7,8]. In contrast, the Charpy test gives only an overall energy value, which may include other sources of energy than fracture initiation. The most obvious is perhaps the kinetic energy imparted to the fractured sections of the specimen. In some tests, fracture may initiate in a ductile mode that quickly changes to cleavage. Under these conditions, the Charpy energy will include both fracture modes. In contrast, the stress wave loading technique is sensitive only to the initiation mode of fracture, since all measurements are made at that instant. Lastly, because of the geometry adopted in the present test, fracture occurs during initial passage of the tensile pulse with no reflections from free surfaces. The incident tensile pulse is sufficiently large so fracture occurs on the rising pulse while plane strain conditions obtain at the fracture site, at least for the stress field in the near crack tip region. The results of the present tests show that the dynamic fracture toughness of this steel is consistently greater than for quasi-static loading at all temperatures for all three tempers, the only exception being for the 425°C temper in the transition temperature regime.

Since most investigations on mechanical properties include Charpy results, Charpy specimens of the various tempers were tested, providing results in close agreement with those of other investigators [9,10]. Tempered martensite embrittlement was observed in the 350°C temper steel. In the plane strain fracture initiation test no embrittlement trough was observed at room temperature and above, in spite of clear indication of the formation of cementite precipitates known to cause embrittlement. This may be explained in terms of the role of residual impurities [10,11], or else may be simply due to the different method of testing. An



embrittlement trough does occur in the plane strain test for specimens tempered at 350°C once the testing temperature is set below the ductile-to-brittle transition temperature. We note also that the dynamic loading rate produces a more pronounced embrittlement trough.

The dynamic stress-strain behavior in shear of this material was determined by loading a thin-walled tube specimen in a torsional Kolsky bar. The technique followed is described in [12,13]. By this means a stress-strain curve is obtained representing material behavior at a strain rate on the order of  $10^3 \text{ sec}^{-1}$ . A comparison with quasi-static results indicates that there is a considerable loss in ductility at the highest rate. Furthermore, a higher strain rate generally results in a higher yield stress while an increase in testing temperature decreases the yield stress somewhat. Just as an increase in tempering temperature decreases the hardness, so it decreases the yield stress for deformation at either rate. The initial yield stress in shear may be converted to a corresponding tensile value and then used to check the validity of the fracture toughness criterion employed.

In addition, the void initiation strain was determined from tensile testing of short circumferentially notched specimens. Extensive quantitative fractography was performed on the plane strain fracture specimens to find the dominant mode of fracture initiation, and transmission electron microscopy was employed to establish the nature and distribution of the particles after tempering.

The plan of this report is as follows. In the next section a brief description is presented of the experimental methods employed. In Section III the results are presented with some discussion and an attempt at modeling the fracture behavior. In the last section conclusions are drawn.

## II. DESCRIPTION OF EXPERIMENTS

### II.1 Material

The material tested was an AISI 4340 VAR steel provided by Republic Steel Company as a single billet, heat no 3841687, and later rolled into round bars of 2.54 cm diameter. Its chemical composition is given in Table 1. AISI 4340 is a low alloy martensitic steel that can be heat treated to provide a wide range of hardness values. Other studies have shown that most of the inclusions in 4340 steel are MnS particles [14]. However, their concentration is considerably reduced by the vacuum arc remelt (VAR) process [15]. The heat treating cycle employed for the present tests is given in Table 2. It consisted of three steps; (1) normalizing for 1 hour at 900°C, then air cooling; (2) austenitizing for 1 hour at 845°C, followed by an oil quench; and (3) one of three tempers: 1 hour at 350°C or at 425°C followed by an oil quench, or else tempering at 200°C and air cooling. The resulting hardnesses, as measured on the Rockwell C scale are 55, 49, and 45, respectively, for the 200°C, 350°C, and 425°C tempers, Fig. 1. These values are in close agreement with those obtained by other investigators with a similar steel [9, 15].

### II.2 Fracture Specimens

The stress wave loading technique employed requires the use of a very long specimen in the shape of a round bar with a 2.54 cm diameter, Fig. 2. A circumferential notch with a sharp root is machined in the bar, 78 cm from the loading end, and a uniform fatigue crack is grown in from the root of the notch, leaving an unfractured ligament about 0.76 cm in diameter. After machining, all specimens are heat treated in a tube furnace.

## II.3 Description of the Fracture Initiation Experiment

### (a) Dynamic Tests

The dynamic fracture initiation test employed in this study was introduced by Costin et al. [1] and subsequently used in a number of experiments [2, 3, 4]. Essentially, the test consists in loading to fracture a prefatigued notched round bar of 2.54 cm diameter, as shown in Fig. 3. Dynamic loading is imposed by a rapidly rising tensile pulse resulting from an explosive detonation initiated at one end of the bar to produce a loading rate at the fracture site of  $\dot{K}_I = 2 \times 10^6 \text{ MPa } \sqrt{\text{m}} \text{ s}^{-1}$ . To initiate the tensile pulse, the explosive charge is placed against a mass bolted to the end of the bar, and so arranged that detonation of the charge tends to pull the mass away from the bar, thus creating a tensile pulse that travels to the prefatigued section. This tensile pulse is monitored by a set of strain gages as it travels toward the precracked section of the bar, since it is essential that its amplitude be large enough so fracture occurs on the rising portion of the pulse. To avoid possible damage to the instrumentation, the end of the bar with the explosive charge is contained within a vacuum chamber.

A second set of gages monitors the pulse transmitted through the precracked section, thus providing a measure of average stress at the fracture site in accordance with the principle behind Kolsky's split-Hopkinson bar [16]. The instant of fracture initiation is determined from observations of the transmitted and reflected pulses. Crack opening displacement is measured optically by an adaptation of the moiré technique in which a glass slide is mounted to span the notch in the bar but cemented only to one side of the notch. A grid of 33 lines/mm is deposited photographically on the bar and a matching grid on the glass slide. As the crack opens the two grids slide past each other, and their relative displacement is determined from changes in the interference pattern using a photodiode. Thus, the instrumentation provides measures of average stress at the fracture site and of crack

opening displacement, each as a function of time. These are used for calculating a critical stress intensity factor  $K_{Ic}$ , or  $J_{Ic}$  when the metal is more ductile. A common zero time point is established between the two curves by considering the trigger times of the oscilloscopes and taking into account the time delays between the arrival of the pulse at the various data recording positions on the specimen. Once a common zero is established, time is eliminated between the two plots, resulting in a load-displacement curve for the dynamic fracture test. A check on results obtained by means of the moire technique is provided by more conventional instrumentation, as described in (c) below. For tests at low or elevated temperatures an environmental chamber encloses the notched section of the bar.

For a nominally brittle material the parameter of interest is  $K_{Ic}$ . The plane strain fracture toughness is calculated, according to Tada et al. [17], as

$$K_I = \frac{P}{\pi R^2} \sqrt{\pi R} F(2R/D) \quad (1)$$

where  $R$  is the radius of the remaining circular ligament after fatiguing,  $P$  is the applied load,  $D$  is the outer diameter of the bar, and  $F(2R/D)$  is a size function equal to about 0.49 in the present experiment. The load  $P$  used in calculating  $K_{Ic}$  from Equation (1) is determined from the load-displacement curve in accordance with the American Society for Testing and Materials standards by using the 5 percent offset procedure. In order to apply linear fracture mechanics concepts, the size of the crack tip plastic zone must be small compared with the nominal dimensions of the specimen. As a criterion for a valid  $K_{Ic}$  test

$$R \geq 2.5 \left[ \frac{K_{Ic}}{\sigma_y} \right]^2 \quad (2)$$

is used, where  $\sigma_y$  is the initial yield stress of the material determined at a strain rate comparable to that achieved near the crack tip region during the fracture test. The

required flow stress for each temper is determined using a torsional Kolsky bar in order to obtain both quasi-static and dynamic values. The specimens used for this purpose were first machined and then heat treated in batches of six to insure uniformity. Details of this torsion test are described in the next section.

When testing more ductile materials, the specimen size may not be adequate to contain the plastic zone within the limit imposed by Equation (2). In this case, a J-integral approach is adopted. Paris [18] has suggested that a possible criterion for a valid  $J_{Ic}$  test is

$$R \geq 50 \frac{J_{Ic}}{\sigma_y} \quad (3)$$

and this criterion was used in determining the validity of present results. Rice et al. [19] have shown that the value of  $J$  for notched round bars may be determined from a load-displacement curve according to

$$J_I = \frac{1}{2\pi R^2} \left[ 3 \int_0^{\delta_c} P d\delta_c - P\delta_c \right] \quad (4)$$

where  $\delta_c$  is the load-point displacement due to the presence of the crack. For present purposes, use of the notch opening displacement at the bar surface was taken for the load-point displacement. This is justified in view of the analysis of this experiment presented by Nakamura et al. [7].

Once  $J$  is determined, an equivalent  $K_{Ic}$  can be calculated from

$$K_{Ic}^e = \left[ \frac{E J_{Ic}}{1-\nu^2} \right]^{1/2} \quad (5)$$

where  $K_{Ic}^e$  may be interpreted as the value of the plane-strain fracture toughness one would measure had a large enough specimen been used to achieve a valid test according to Equation (1).

The final parameter of interest in dynamic testing is  $\dot{K}_I$  which is defined usually as

$$\dot{K}_I = \frac{K_{Ic}}{t} \quad (6)$$

where  $t$  is some characteristic time of the test. Here  $t$  is taken as the time required to load the crack from the unstressed condition up to the critical value of  $K_{Ic}$ . Records show that for a dynamic test  $t$  is approximately  $25\mu s$ , whereas for a static test  $t$  is usually on the order of 60 to 90 seconds.

### (b) Quasi-Static Tests

The static fracture initiation tests were performed with a prefatigued notched round bar having the same geometry as the specimens used in the dynamic tests and subjected to the same heat-treatments. Tension to fracture was supplied by a 120,000 pound capacity Riehle universal testing machine, equipped with a load cell; an environmental chamber was used for tests at low or elevated temperatures. In the static tests, the notch opening displacement was measured optically by employing an MTI photonic sensor. This is an optical technique that makes use of a fiber optic tube and a target mirror to convert reflected light to an electrical signal. As shown in Fig. 4, a probe is attached to the transmitter side of the bar spanning the notch and almost in contact with the target mirror on the incident side. The probe itself consists of a "random" arrangement of transmitter and receiving fibers. The response of the apparatus is sensitive to the distance separating probe and mirror. Initially, the probe is so near the mirror that the light carried by the transmitter fibers cannot be reflected back into the receiving fibers. As the probe begins to withdraw from the mirror, reflected light gradually covers a greater area of the ends of the receiving fibers, thus gradually increasing the sensor output. As may be seen in Fig. 5a, the millivolt output is approximately a linear function of

the separation between probe and mirror until this distance attains about 120 microns. All present experiments make use of this linear range only. Beyond that range the response of the MTI probe reaches a maximum and then gradually falls off.

As shown in Fig. 6, the instant at which fracture initiated was determined by a measurement of electrical resistivity. A DC current was furnished by a 6 volt power supply connected to the bar at two points 10 cm to either side of the crack. In principle, the resistivity between these two points increases linearly with increasing load as long as the crack does not extend. A departure from linearity is used to provide the value of the load and hence of the instant of fracture initiation.

The reliability of the procedure was examined by Couque et al. [20] in tests with a plain carbon steel. Their goal was to distinguish experimentally between crack blunting and the initiation of a microcrack at the crack tip. For this purpose they loaded specimens to a predetermined level either sufficient for initiation of a microcrack at the crack tip or slightly below the required value. Their technique involved placing wedges within the opened crack of a specimen under load to preserve the loaded geometry and later be able to examine the crack tip microscopically and determine positively whether a microcrack had initiated. Their results, in general, showed that the electrical sensitivity method properly used provides reasonably dependable values for the instant of crack initiation.

#### **(c) Measurement of Displacement in the Dynamic Fracture Test by Means of the MTI Photonic Sensor**

In a number of the room-temperature dynamic tests, the measurement of crack opening displacement was checked by employing an MTI Photonic Sensor, along with the moire technique. The MTI 1000 Photonic Sensor has a frequency response of 1MHz, which is adequate for the present tests as shown in a calibration against the

moire technique. Use of this instrument also requires that the mass of the mirror, etc., be reduced to a minimum and attached firmly to the bars. This is the reason for the grooves shown in Fig. 4a.

For a comparison between displacements measured by the photonic sensor and the moire technique both devices were mounted on the specimens and tested. The response from the photonic sensor were nearly the same if not quicker than the response from the moire technique for all tests. Two of the results are presented in Fig. 5b.

The room temperature dynamic stress intensity factors of 425 temper specimens with the displacement values obtained from the moire technique was  $148 \text{ MPa}\sqrt{\text{m}}$  whereas that using the photonic sensor was  $150 \text{ MPa}\sqrt{\text{m}}$ .

#### II.4. Static and Dynamic Stress-Strain Behavior

The static and dynamic stress-strain behavior of specimens of the three tempers was determined to help characterize fully the material and, in particular, to provide the value of dynamic flow stress needed for use in Equations (2) and (3). Specimens were tested in the torsional Kolsky bar first described by Duffy et al. [12] and later modified by Costin et al. [13]. A schematic diagram of the experiment is shown in Fig. 7a. The specimen consists of a short thin-walled tube mounted in the bar by means of a pair of flanges, Fig. 7b. A heat treatment similar to that used by Tanimura and Duffy [21] was used here: the specimens were placed in groups of six at the center of a 61 cm long tube-furnace. An argon atmosphere that first passed over copper coils was used to prevent oxidation. The heat treating cycle consisted of three steps: (1) normalizing for 1/2 hour at  $900^{\circ}\text{C}$ , then cooling in argon; (2) austenitizing for 1/2 hour at  $845^{\circ}\text{C}$ , followed by an oil quench; (3) tempering for 1/2 hour. Specimens tempered at  $350^{\circ}\text{C}$  and  $425^{\circ}\text{C}$  were oil quenched; specimens tempered at  $200^{\circ}\text{C}$  were argon cooled. Their hardness was measured as



HRC 55, 49 44 for the 200°C, 350°C and 425°C tempers, respectively, which correspond closely with the hardness values obtained for the notched round bar used in the fracture initiation tests.

To obtain a dynamic stress-strain curve, a torque is stored between pulley A and clamp B, shown in Fig. 7a. Upon sudden release of the clamp by the fracture of a breaker piece within the clamp, a torsional loading pulse with an amplitude half as great as that stored propagates down the bar toward the specimen, while an unloading pulse of equal magnitude propagates from the clamp toward pulley A. Upon reaching the specimen, part of the pulse is transmitted and part is reflected. Strain gages are mounted on the bar to either side of the specimen and, following Kolsky's original technique [16], it can be shown that the transmitted pulse gives a measure of shear stress in the specimen as a function of time while the reflected pulse provides a measure of shear strain rate. Calibration of the gage outputs is described in [12] and [13]. The stress-strain curve is obtained by integrating the reflected pulse to give shear strain and by eliminating time between the stress-time and strain-time signals. By means of this apparatus a stress-strain curve is obtained representing material behavior at a strain rate of about  $10^3 \text{ s}^{-1}$ . The same apparatus is employed to obtain a static stress-strain curve. For this purpose the pulley at D is rotated slowly against the fixed clamp by employing a variable speed drive. A pair of direct current differential transformers measures the rotation of the bar to either side of the specimen, while strain gages on the bar provide a measure of torque. Thus, a static stress-strain curve is established in shear at a strain rate of about  $10^{-4} \text{ s}^{-1}$  using specimens of identical geometry with the dynamic specimens. Tests at elevated temperature are performed by enclosing the specimen in a radiant heating clam shell furnace, while the temperature is measured by a thermocouple attached to the flange of the specimen. An environmental chamber with a controlled flow of nitrogen gas from a liquid nitrogen bottle is used to attain the cold temperatures.

## II.5 Metallography and Microscopy

Standard quantitative metallographic techniques were used to determine the grain size and the average spacing of the principal inclusions, i.e. of the MnS particles. Thin foils were obtained from the fractured specimens for examination by transmission electron microscopy (TEM). They were taken from within the homogeneously heat treated portion of the specimen adjacent to the fracture zone. Slices about 0.3 mm thick were cut longitudinally with a 0.3 mm thick silicon carbide wheel under flood cooling to avoid tempering. These slices were thinned chemically to about 0.1 mm in 10% HF-H<sub>2</sub>O<sub>2</sub> solution and then discs with diameters of 3 mm were prepared by punching. Final polishing was carried out using a Fischione automatic twin jet electropolisher at room temperature in a solution of 50 ml perchloric acid + 450 ml acetic acid with a voltage range of 30 to 40 volts and a current range of 50 to 60 milliamps. Microscopic examination of the foils was carried out with a Philips EM420 electron microscope operated at 120 KV.

An AMR-1000A scanning electron microscope (SEM) operated at 20KV was used to study the fracture surfaces of the tensile and fracture toughness specimens. Immediately after testing, the fracture surfaces were sprayed with "Rust-Vito", a corrosion resistant compound. Since this coating dissolves readily in acetone using an ultrasonic cleaner it was not removed until immediately before microscopic examination. An EDAX (energy dispersive analysis of X-rays) unit was used in conjunction with SEM to analyze the inclusion chemistry.

## II.6 Determination of Void Initiation Strains

A separate set of experiments was used to determine the strain at which voids initiate in ductile fracture. In these experiments a high triaxial stress field is imposed by loading in tension the notched specimens shown in Fig. 8. The local

strains and strain gradients were determined at various points along the axes of these specimens starting at the point of minimum radius. This was effected by depositing carbon evaporated grids on the specimen's surfaces. The plastic strain,  $\epsilon_z$ , in the cross-section cut parallel to the tensile axis prior to fracture can be obtained from the neck geometry. By comparing the current diameter  $D_z$ , measured along the tensile axis at a distance  $Z$  from the center of the necked region, with the original diameter  $D_0$ , one obtains

$$\epsilon_z = 2 \ln (D_0/D_z) \quad (7)$$

After testing, the specimens were cross-sectioned and detailed metallographic studies were conducted using scanning electron microscopy at a magnification of 800 times. Voids were observed to initiate at submicron carbide particles, and a measurement was made of the percentage of submicron carbide particles associated with voids.

### III. RESULTS & DISCUSSION

#### III.1 Stress-Strain Behavior in Shear

Fig. 9-11 show the stress-strain behavior in shear of specimens of the three tempers at the quasi-static and dynamic strain rates. Tests were conducted at three temperatures:  $-100^\circ\text{C}$ , room temperature and  $+100^\circ\text{C}$ . For the  $350^\circ\text{C}$  and  $425^\circ\text{C}$  tempers the influence of strain rate on the flow stress is very small, although there appears to be an initial upper and lower yield point under dynamic deformation. For the  $200^\circ\text{C}$  temper, a quasi-static strain rate requires a higher flow stress than a dynamic rate although the initial yield stress is somewhat lower at the quasi-static

rate. For all three tempers the influence of the strain rate is seen most strongly in the greater ductility at the lower rate. Thus, while fracture occurs between 10% and 20% strain under dynamic conditions, statically it never occurs before a 40% strain is imposed.

Since an important goal of this study is a better understanding of fracture initiation under dynamic loading, the dependence of the dynamic flow stress on temper and on testing temperature are presented together in Fig. 12. Table 3 lists values of the initial yield stress  $\sigma_y$  at a 0.2% offset as determined dynamically in shear with the torsional Kolsky bar. The conversion of the flow stress values in shear to the corresponding tensile values is effected by using the Mises criterion and by assuming incompressibility of the material during plastic deformation so that  $\sigma = \sqrt{3} \tau$  and  $\epsilon = \gamma/\sqrt{3}$ . It also gives values of the flow stress at  $\gamma = 0.05$  and of the ultimate tensile stress. We also included a power law strain hardening index  $n$ , defined in uniaxial tension as  $\sigma/\sigma_y = (\epsilon/\epsilon_y)^n$  where  $\sigma_y$  and  $\epsilon_y$  are the yield stress and strain, respectively, and  $\alpha$  is a material constant. The values of  $\sigma_y$  from this table were used to check the validity of the fracture toughness calculated on the basis of Eqns. (2) and (3). Fig. 13 presents initial yield stress in shear  $\tau_y$  at a 0.2% offset for three different tempers as a function of testing temperatures. In general, a higher strain rate results in a higher yield stress while an increase in testing temperature decreases the yield stress. However, the dependence on strain rate and test temperature are not very great in the range tested. Kendall & Davidson [22] observed a monotonic increase of 6% in the yield stress at an 0.2% offset over the strain-rate ranging from  $10^{-4}$  to  $10 \text{ s}^{-1}$ , for fine grain 4340 steel produced by austenitizing at  $843^\circ\text{C}$  and tempering at  $552^\circ\text{C}$ . An increase in tempering temperature also decreases the yield stress for both strain rates. There are two exceptions to this trend. The first occurs for the  $200^\circ\text{C}$  temper at  $-100^\circ\text{C}$  and at

+100°C where the dynamic yield stress appears to be lower than the quasi-static. However, the differences are small and lie within experimental error. In addition, at 100°C the dynamic yield stress is lower for the 200°C temper than for the 350°C temper, although the differences again are small. Fig. 14 shows the ultimate stress for three different tempers at the three testing temperatures, and Fig. 15 the flow stress at a shear strain of 5%. The trend in the last figure is similar to that observed for the axial yield stress,  $\sigma_y$ .

It should also be mentioned that in static testing at 100°C discontinuous yielding occurred with all three tempers, Fig. 9-11. This effect was most pronounced in specimens tempered at 200°C. A similar result has been seen by many investigators with different steels, going back to Manjoine [23] who conducted a series of tests on mild steel to determine the effects of strain rate and temperature on the flow stress. He noted (1) that when the flow stress vs. strain rate curve has a negative slope, discontinuous yielding can be expected in the stress-strain curve, and (2) that the fluctuations of load which occur during discontinuous yielding decrease in amplitude as the strain rate is increased. Our experimental result for the 200°C temper specimens, Fig. 16, shows a drop in flow stress with an increase in strain rate. It is therefore consistent with Manjoine's observations that the serrations be most pronounced with this steel. One should also note that the quasi-static strain rate in the present tests was approximately the same as in those of Manjoine, making our results generally consistent with his.

### III.2 Charpy Impact Toughness

Fig. 17 presents the results of a series of Charpy impact tests for the three different tempers of the VAR 4340 steel as a function of test temperature. The Charpy fracture toughness for the three test temperatures as a function of temper is presented in Fig. 18. It is evident that the CVN energy is lower for the 350°C temper than for the 200°C and 425°C tempers implying the existence of an embrittlement trough. Although present results are not extensive, they compare quite closely with the Charpy results of Banerji et al. [9], for an "aircraft quality" 4340 VAR steel (Heat B1) and of Materkowski and Krauss [10] who tested a 4340 steel with 0.003 w/o phosphorous. Materkowski and Krauss performed both Charpy tests and plane strain fracture tests, and their results showed an embrittlement trough in the Charpy test but not in the plane strain fracture results.

### III.3 Plane Strain Fracture Initiation Toughness

Fig. 19 presents the results of the fracture initiation tests performed with the notched round bar specimens of Fig. 2. The quasi-static and dynamic values of the stress intensity factor,  $K_{Ic}$  and  $K_{Id}$ , are given as functions of temperature over the range of  $-140^{\circ}\text{C}$  to  $+100^{\circ}\text{C}$ . Some tests did not satisfy the ASTM requirement for minimum specimen thickness, as specified by Equation (2). In these instances a J integral approach is employed through the use of Equation (4), and an equivalent value of the fracture toughness,  $K_{Ic}^*$ , is determined by using Equation (5). Results of these tests are also plotted in the figure and identified by the letter E.

It is evident that, when plotted as a function of temperature, the stress intensity factor follows the expected trend from a lower to an upper shelf. The results indicate that for quasi-static fracture these two levels are fairly well established, as is therefore the quasi-static transition temperature. Dynamically, the lower shelf level again seems well established for each temper but the upper shelf is not as clearly determined, although the transition temperature range seems fairly clear. In any case, this steel is generally tougher dynamically than quasi-statically, and indeed at the higher temperatures, the difference becomes quite large. The only exception appears to occur in the  $425^{\circ}\text{C}$  temper tested at  $-50^{\circ}\text{C}$ , for which the transition temperature appears to be somewhat lower dynamically than statically.

For the  $350^{\circ}\text{C}$  temper, in the range from room temperature to  $+100^{\circ}\text{C}$ , the fracture initiation mode is mostly fibrous for either quasi-static or dynamic loading. However, the dynamic fracture toughness is about 40 percent greater at room temperature and more than twice as great at  $+100^{\circ}\text{C}$  test than the corresponding quasi-static values. This is a trend that has been observed in other steels, for instance in the work of Couque et al. [4], and may be attributed to the higher flow stresses that prevail at the higher strain rates. Dynamic fracture initiation toughness is consistently higher than quasi-static fracture toughness at all test temperatures for

both the 200°C temper and the 350°C temper (Fig. 20 & 21). However, in the case of the 425°C temper, the  $K_{Ic}$  and  $K_{Id}$  curves cross each other twice within the test temperature range. This reflects the fact that the dynamic transition temperature is higher than the quasi-static (Fig. 22). The lines first cross between -100°C and -50°C where  $K_{Ic}$  jumps to an apparent upper shelf, and cross again between -50°C and room temperature where  $K_{Id}$  is now in the transition temperature range for dynamic loading rate.

Fig. 23 presents the values of the dynamic fracture initiation toughness as a function of test temperature for the three different tempers. There is an apparent lower shelf toughness that extends up to about -50°C for the 350°C and 425°C tempers. Thereafter, fracture toughness increases abruptly to an apparent upper shelf that is reached in the neighborhood of +100°C. However, for the 200°C temper, there is a gradual increase in  $K_{Id}$  from about 47 MPa $\sqrt{m}$  at -140°C to 69 MPa $\sqrt{m}$  at room temperature and a noticeable increase to 94 MPa $\sqrt{m}$  at +100°C. Thus,  $K_{Id}$  for the 200°C temper varies almost linearly over the entire temperature range leaving some doubt as to the level of the upper and lower shelves.  $K_{Id}$  for the 350°C temper, both at room temperature and at +100°C, lies between the  $K_{Id}$  values for the 200°C and the 425°C tempers. The increase in toughness as tempering temperature is raised is more pronounced at higher temperatures. But at a temperature of -50°C and below, a higher tempering temperature does not necessarily produce a higher dynamic fracture toughness, i.e. the value of  $K_{Id}$  for the 425°C temper is slightly lower than for the 200°C temper, and  $K_{Id}$  for the 350°C temper is even lower than for the 425°C temper. The ductile to brittle transition appears to occur at a lower test temperature, and with a steeper slope, for the higher tempering temperature. It should be mentioned that dynamic fracture experiments were conducted on specimens of the same steel at an even higher loading rate by Ravichandran and Clifton [24]. Using a plate impact technique they attained a value



of  $K_{Ic} = 10^8 \text{ MPa}\sqrt{\text{m}} \text{ s}^{-1}$ , i.e., a value that is almost two orders of magnitude greater than in the present experiments. The specimens employed by Ravichandran and Clifton are larger than those used in the present tests; their diameter is about 5 cm. The heat treatment employed in [24] consisted of the following: austenitization at  $870^\circ\text{C}$  for two hours, followed by an oil quench and a temper at  $100^\circ\text{C}$  for two hours, followed by air cooling. The resulting hardness measured at the specimen's center was  $R_c = 52$ , and in the plate impact tests the value of the critical stress intensity factor was  $62 \text{ MPa}\sqrt{\text{m}}$  at room temperature. This value of  $K_{Ic}$  is somewhat lower than the  $69 \text{ MPa}\sqrt{\text{m}}$  measured in the present tests, even though the hardness of the specimens in the present tests is somewhat greater ( $R_c = 55$ ) and the loading rate is considerably lower. This apparent discrepancy prompted us to repeat the present tests supplementing the grid system for measuring crack opening displacement with a more conventional technique, as described below. The fracture results remain substantially unchanged. However, as pointed out by Godse et al. [25], there are significant differences in the microstructures of the two steels. The principal one is the existence of upper bainite in the steel tested by Ravichandran and Clifton [24] as shown in Fig. 24. In contrast, our specimens reveal only a martensitic microstructure with no evidence of upper bainite, Fig. 24. This difference is consistent with the more rapid quench rate expected in a specimen of smaller dimensions. Upper bainite has a lower hardness and a lower tensile strength than the martensitic structure. Godse et al. also point out that microcrack nucleation in the tests described in [24] initiate in the bainite, and that this seems to be the first stage of macrocrack propagation in this steel. The microcracking is followed by shear localization within the martensite between the cracked bainite sites. Hence, the presence of bainite, by serving as a microcrack nucleation site, has an embrittling effect that presumably reduces the toughness of the steel specimen tested by Ravichandran and Clifton, thus providing a reason for the higher fracture initiation

toughness observed in the present tests.

The quasi-static fracture toughness  $K_{IC}$  is presented as a function of temperature in Fig. 25. It is evident that the 425°C temper provides a tougher material than either of the other tempers for all test temperatures. In addition, the transition temperature is lower than in the other two. For the 350°C temper, the values of  $K_{IC}$  increase gradually up to -50°C and then somewhat more sharply up to room temperature, where it appears that the upper shelf has been reached. For the 200°C temper, there is an apparent lower shelf below -100°C and a transition range between -100°C and room temperature. At +100°C,  $K_{IC}$  drops slightly as the material enters the dynamic strain aging region, known as the blue brittle range, which is associated with the occurrence of serrations in the stress-strain curve. It should be noted that within this temperature range the difference in  $K_{IC}$  at room temperature and +100°C also reflects a difference in yield stress. In fact, serrations in the shear stress-shear strain curve is observed consistently for all three tempers tested at +100°C at a quasi-static strain rate (Fig. 9-11).

Qualitative transmission electron micrography was performed to study tempered martensite embrittlement (TME) in the steel specimens tempered at 350°C. The micrograph clearly shows the formation of platelike  $Fe_3C$  precipitates along the martensite lath boundary, Fig. 26. However, the embrittlement trough, characteristic of tempered martensite embrittlement, is absent in the plane strain fracture toughness testing at room temperature, Fig. 27. It may be recalled that the Charpy test results did show a trough, although a shallow one, for this temper. It appears that in plane strain testing the trough is absent, although the difference in toughness between the 425°C temper and the 350°C temper is considerable. This increase is generally attributed to matrix softening [26]. The absence of an embrittlement trough at a tempering temperature of 350°C, in spite of a clear indication of the formation of carbide precipitates along the lath boundaries, leads one to conclude that the carbides

are not the only cause of the loss in toughness. The results of Briant and Banerji [11], obtained in Charpy tests performed at room temperature, showed practically no embrittlement trough for a fine grained AISI 4340 steel (ASTM grain size 8) doped with 0.01% phosphorous. Materkowski and Krauss [10] found that the plane strain fracture toughness of an AISI 4340 steel with a higher phosphorous content (0.03 wt %) gave stronger evidence of TME than with a lower phosphorous content (0.003 wt %).  $K_{Ic}$  for the lower phosphorous content steel increased with increasing tempering temperature even in the TME range, a result explained by the formation of a narrow zone of ductile fracture adjacent to the fatigue precrack during fracture toughness testing. Materkowski and Krauss [10] attributed the embrittlement mechanisms to a combination of phosphorous segregation and grain boundary carbide formation during tempering in the critical range. It is possible also that the type of test, i.e. plane strain as opposed to Charpy, influences TME behavior. This would be consistent with the present results. Finally, it should be remembered that the present plane strain test is a fracture initiation experiment, i.e. the value of  $K_{Ic}$  is set by the peak in the transmitted pulse, which occurs at the start of the fracture process. In contrast, Charpy results give the total energy, i.e. the energy required for initiation, propagation across the specimen and any extraneous remaining kinetic energy.

In spite of the absence of TME at room temperature, the results presented in Fig. 27 show that when this steel is tested at lower temperatures, between  $-50^{\circ}\text{C}$  and  $-140^{\circ}\text{C}$ , the troughs become apparent for the specimens tempered at  $350^{\circ}\text{C}$ . Here, it is interesting to note that the trough is very shallow for the static test, whereas it is pronounced for the dynamic test. Briant and Banerji [11] found the ductile-to-brittle transition temperature for the fine grain specimen (ASTM grain size 8) to be slightly above  $0^{\circ}\text{C}$ , and observed that the embrittlement trough becomes apparent once the test

temperature is below the ductile-to-brittle transition temperature in specimens tempered near 350°C. Fig. 28 presents the ductile-to-brittle transition temperature as a function of tempering temperature determined in the plane strain fracture initiation tests. As expected, the transition temperature is shifted to a higher temperature as the loading rate is increased. Due to this shift in the transition temperature, the lower shelf is more clearly defined for dynamic loading whereas the upper shelf is more clearly defined for quasi-static loading, for the temperature range of -140°C to +100°C. Present results also show that a higher tempering temperature consistently lowers the transition temperature for both loading rates. The transition temperature is near room temperature for the 350°C tempered specimen for dynamic loading conditions, and about -50°C under quasi-static loading conditions. Hence, the embrittlement trough becomes apparent only when testing at -50°C or below. Kula and Anctil [27] showed that low temperature tests are necessary to study embrittlement in an AISI 4340 steel. Present data indicate that a lower testing temperature and a higher loading rate increase the tendency to tempered martensite embrittlement. Despite the effects of tempered martensite embrittlement, the dynamic fracture toughness is higher than the quasi-static fracture toughness at all tempering temperatures, with the exception of the 425°C temper in the transition temperature regime.

### III.4 Microstructure

#### a. Optical Microscopy

The heat treatment adopted for the present tests and described in Table 2 produces an average prior austenite grain size of 10 to 20 $\mu$ m (ASTM No. 10 to 11). As in other AISI 4340 steels [28], the microstructure of this quenched and tempered steel consists almost entirely of fine lath martensite having different lath sizes and orientations. An EDAX analysis shows that the present steel contains inclusions of manganese sulfide, (MnS). Their volume fraction varied from specimen to specimen, as well as within each of the bars tested. The average spacing of the MnS particles was measured to be approximately 90 $\mu$ m for the 4340 VAR steel tested. This is quite large when compared for instance with the 52 $\mu$ m for the commercial 4340 steel tested by Lee [29].

#### b. Transmission Electron Microscopy

Thin foils of this martensitic steel were studied in detail by direct transmission electron microscopy to establish the nature of the structural changes and of the dislocation distribution associated with the three tempering processes employed.

The quenched structure within the martensite laths shows extremely high dislocation densities and some microtwins. The presence of films of retained austenite was confirmed by employing the selected area diffraction pattern technique. Upon tempering to 200°C, epsilon carbide resolution begins with an attendant precipitation of cementite. The structure within the martensite laths is almost unresolvable, as shown in Fig. 29. In some regions, a high density of cementite carbide precipitates is also seen.

Drastic differences are seen to occur in the microstructure of specimens tempered at 350°C. Fig. 26 shows all carbides, those along the lath boundaries or within the laths, and dislocation recovery. At this tempering temperature retained austenite no longer exists because it decomposes into stringers of interlath carbides. It is clear from Fig. 26 that epsilon carbides were replaced by cementites which have {012} Widmanstätten arrangement. The selected area diffraction (SAD) pattern obtained from Fig. 30a is shown in Fig. 30c. Analysis of the diffraction pattern, as illustrated in Fig. 30d, shows the orientation relationship between martensite and cementite. The dark field image using one of these cementite spots is shown in Fig. 30b. The results of the present study support the conclusions reported in [29] that most of the interlath austenite was decomposed to be replaced by interlath films of cementite and that epsilon carbide was replaced by interlath cementite. Precipitation of cementites on the microtwins is also observed in this structure (Fig. 26). Similar effects are observed at 425°C, as shown in Fig. 31. At this last tempering temperature, however, recovery, carbide growth, and agglomeration reduced some of the internal strains, resulting in somewhat decreased dislocation density. The first evidence of spheroidal carbide precipitate is also seen at this point.

Transmission electron microscopy on carbon extraction replicas was also performed in the structures tempered at 200°C. The average spacing of particles in the size range of approximately 0.1  $\mu\text{m}$  were found to be about 3  $\mu\text{m}$  as measured by a method based on one, two, or more nearest neighbor pairs of point particles in a plane. According to Carlson et al. [30], who analyzed by observation of diffraction patterns, particles of this nature are undissolved alloy carbides (predominantly  $\text{M}_7\text{C}_3$ ).

### c. Fractography

Microscopic observations were made of the fracture surface to help identify quantitatively the fracture modes active during initiation for the two loading rates, and over the temperature range. Since this study concentrates on the fracture initiation process the initiation zone was defined as to extend over a distance of one crack opening displacement from the fatigue annulus and all observations were made within this zone. Fig. 32 shows the fracture surface of a specimen with a 350°C tempered microstructure tested quasi-statically at room temperature. The features observed in this micrograph are typical of most of the fracture surfaces. The pre-fatigue zone is clearly distinguished from the mostly fibrous monotonic fracture initiation zone. Other micrographs reveal that at temperatures below room temperature the fracture initiation zone is characterized by a mixed fracture mode, i.e. fibrous, quasi-cleavage, and intergranular. At higher test temperatures, in particular at +100°C, the initiation zone is mixed fibrous and intergranular.

Figs. 33a-c are typical SEM fractographs of the initiation zones observed in specimens tempered at 200, 350 and 425°C and tested quasi-statically at room temperature. The fracture mode of these tempered specimens was mostly transgranular microvoid coalescence, but small, cleaved faces likely to be prior austenite grain boundaries were also observed for the specimens tempered at 350°C and 425°C.

The trends in the mode of fracture toughness, including the transition with increasing temperature from intergranular to fibrous fracture can be correlated by quantitative fractography. These modes of fracture initiation are tabulated according to microstructure, testing temperature, and loading condition in Table 4. The fracture initiation mode is indicated qualitatively by the letters "F", "Q", or "I" depending upon whether the dominant mode of initiation is by fibrous, quasi-cleavage, or intergranular mechanisms. To help visualize the trends, the

percentage of each fracture initiation mode is plotted in Fig. 34 as a function of testing temperature. As can be seen the dominant fracture mode depends strongly on the temper and on the testing temperature. In contrast, any change in appearance at a higher loading rate is relatively subtle. In general, the percentage of fibrous fracture decreases continuously as the testing temperature decreases for either dynamic or quasi-static loading. Below a temperature of  $-100^{\circ}\text{C}$ , quasi-cleavage is the dominant mode for the  $200^{\circ}\text{C}$  temper whereas a combination of quasi-cleavage and intergranular fracture are dominant in the initiation zone as fibrous microvoid coalescence diminishes. Once the fracture toughness value lies on the upper shelf region the dominant mode of initiation is almost entirely fibrous, Fig. 35. For specimens tempered at  $350^{\circ}\text{C}$  and tested under dynamic loading condition, at temperatures of  $-50^{\circ}\text{C}$  and below, i.e. below the ductile-to-brittle transition temperature, a markedly higher percentage of intergranular fracture occurs. This is in agreement with the results of Bandyopadhyay and McMahon [32]. As a result,  $K_{Id}$  is reduced to a value considerably below that obtained in the fracture of a specimen tempered at  $200^{\circ}\text{C}$  (see Figs. 19 & 36). This behavior appears to be typical of steels susceptible to tempered martensite embrittlement [9, 31].

The relative frequency of particular dimple sizes within the fracture initiation zone is given in Fig. 37 for the  $200^{\circ}\text{C}$  temper specimens. The average dimple sizes were computed to be  $3.8 \pm 2.3\mu\text{m}$  for quasi-static loading and  $4.0 \pm 2.6\mu\text{m}$  for dynamic loading. It is also observed that when the fracture mode is fibrous the dimple size for each temper is consistent within the statistical spread of the size distribution. It was noted earlier that the measured dimple spacings correlated with the measured spacings of carbide particles in the size range of approximately  $0.1\mu\text{m}$ . For the specimens tempered at  $200^{\circ}\text{C}$  the average dimple sizes are somewhat larger than the measured particle spacings, but the two sets of sizes overlap within the statistical spread of the size distribution.



Chemical analysis of particles found on the fracture surface confirms that some of the particles responsible for voids are small MnS particles. Examples of MnS particles, identified by EDS are indicated in Fig. 38. The dimples associated with MnS inclusions are generally on the large end of the dimple size distributions.

#### **d. Secondary Microcracks**

Dynamic fracture in the case of the more brittle steels can produce interior secondary microcracks that appear under the fracture surface. These are seen, for instance, in the 200°C temper tested at room temperature, Fig. 39, but were not seen in static fracture of the same or any other steel.

The presence of these microcracks is revealed by sectioning the specimen along a plane perpendicular to the fracture surface and parallel to a diameter. In order to minimize damage during the sectioning process an electro-discharge machine (EDM) was employed.

Typically, the secondary microcracks are seen starting at the fracture surface and running into the specimen roughly parallel to its axis. They originate at a point in the fracture surface about 0.5 or 1.5 mm in from the tip of the fatigue precrack, an indication that perhaps they originate after the start of the fracture process on the main fracture plane and thus do not influence measured values of load or displacement at fracture initiation. Their length in Fig. 39 appears to be about 1.5 mm to 3 mm, but observations with SEM at higher magnification show that microcracks extend further in and may be distributed along prior austenite grain boundaries in the region. Presumably, observations on planes parallel to other diameters would show that the cracks are approximately cylindrical in shape.

The location of these vertical microcracks is within a region where both shear and tensile stresses are present. It is obvious that at any stage of the fracture process the transmitted load acts through the remaining ligament tending to elongate it and, because of Poisson's ratio effects, tending to reduce its diameter. The latter pulls the material within the ligament inward, thus creating a radial tension between the ligament material and an outer annulus not directly under the applied tensile load. The presence of these radial tensile stresses between the ligament and the outer annulus makes the secondary fractures more likely whenever the steel tested is more brittle, as for instance in the 200°C temper and at lower test temperatures. Furthermore, the radial tensile stresses are probably greater under dynamic than under static conditions due to inertia effects, in particular the inertia of the material outside the ligament which must be pulled in radially by the sudden reduction in the ligament diameter.

A second subsurface microcrack is visible in Fig. 39. It runs approximately parallel to the fracture surface and extends over a few millimeters. Again, this crack is seen to extend further under observation with SEM. Figure 39(b) shows the tip of the crack shown in Figure 39(a). The microcracks in Figure 39(b) may be surrounding the prior austenite grains.

Subsurface cracks are seen in the most brittle of the three tempers (200°C), but not in the most ductile (425°C). In the case of the 350°C temper, only the horizontal subsurface crack can occur, i.e., the one running parallel to the fracture surface.

### III.5 Void Initiation Strains

Tensile testing and subsequent metallographic study of the circumferentially notched specimens described earlier, and shown in Fig. 8, was carried out to investigate the strains at which voids initiate at submicron carbide particles in the high triaxial stress field. The ductility of the tensile specimens is found to depend predominantly on test temperature: as the temperature increases the true fracture strain increases for all tempers, as indicated in Table 5. The areal density of voids associated with submicron carbide particles ( $A_v$ ) is plotted in Fig. 40 as a function of macroscopic strain ( $\epsilon_z$ ) in the necked region. The results indicate that the process of void initiation is influenced primarily by the test temperature, and that  $A_v$  increases continuously as one approaches the fracture surface (Fig. 36). Experiments at the same test temperature, show that the development of porosity is similar for all microstructures, i.e., the minimum strain at which voids appear depends quite strongly on microstructure. This strain lies in the range 0.13 to 0.17 following room temperature tests, and 0.06 to 0.10 for a test at  $-140^\circ\text{C}$ , Table 5. Thus, it is possible that the resistance to void initiation at submicron particles increases with a decrease in the test temperature and that this contributes to the level of  $K_I$ . These experimental results can be of considerable value in modelling fracture initiation at the higher temperatures, since the modelling of fracture toughness in ductile materials frequently involves the void initiation strain.

### III.6 Fracture Model

Micromechanical modeling was attempted with the goal of improving our understanding of fracture in the present steel. For this purpose we followed the approach described by Couque et al. [20] in their modeling of fracture in an AISI 1020 hot-rolled steel. For fracture behavior of the 200°C temper steel on the lower shelf, modeling gives approximately correct values of  $K_{Ic}$  and  $K_{Id}$ , and predicts trends correctly, i.e. an increase in the value of the stress intensity factor under dynamic loading conditions. In the case of fibrous fracture, modeling predicts correctly the value of  $K_{Ic}$  for static fracture of the 200°C temper steel but will require modification to take into account dynamic effects. For the 350°C temper the model is less successful and again does not account for dynamic effects. In summary, for the present steel correlations of microstructure with dynamic fracture toughness for quasi-cleavage fracture seems to be more successful than the fibrous fracture and warrants further study.

#### (a) Fibrous Fracture Initiation

In the 4340 VAR steel the average spacing between the larger MnS particles was in the range of 90  $\mu\text{m}$ , whereas the average alloy carbide spacing was about 3  $\mu\text{m}$ . Crack opening displacement at room temperature for all three tempers lies in the range of 4 to 20  $\mu\text{m}$ . In view of the relatively wide spacing of the MnS particles it seems unlikely that these inclusions would play an important role in fracture initiation, except perhaps at higher temperatures where crack opening displacement may be larger.

To interpret the fracture results at room temperature, where the initiation mode is fibrous, the model adopted is the one proposed by Rice and Johnson [32] for ductile fracture beneath a sharp crack. This model accounts for ductile crack extension via void growth and coalescence with a blunting crack tip. To apply the

fracture model, we made use of the numerical solutions obtained by McMeeking [33] for the stress and deformation fields at blunting crack tips. McMeeking's calculations are applicable to materials with various values of the strain hardening index  $n$  and of the ratio of yield stress to elastic modulus  $\sigma_y/E$ . In the particular case of  $n = 0$  and  $\sigma_y/E = 1/100$  an approximate value of crack-tip opening displacement  $\delta_t$  is provided by the equation

$$\delta_t \approx 0.67 J/\sigma_y \quad (1)$$

Couque et al [20] applied small scale yielding in plane strain to relate the critical crack tip opening  $\delta_t^*$  required to initiate crack extension to the critical stress intensity factor  $K_{Ic}$ . When this fracture criterion is combined with equation (1), the critical fracture initiation stress intensity factor becomes

$$K_{Ic} \approx \sqrt{\frac{1.64 \sigma_y E r^*}{(r/\delta_t)^*}} \quad (2)$$

where  $r^*$  is the critical microstructural distance over which a critical strain must be achieved, and  $(r/\delta_t)^*$  is the critical value of  $(r/\delta_t)$  corresponding to an equivalent strain  $\epsilon^D = \epsilon^*$ . Values of  $K_{Ic}$  calculated by means of equation (2) are presented in the next to last column in Table 6a. Equation (2) was employed to model only room temperature tests, since the void initiation strain was determined only at room temperature. In the calculations, the values used for the axial yield stress  $\sigma_y$  are based on the stress-strain behavior in shear by setting  $\sigma_y$  equal to  $\sqrt{3} \tau_y$ , Fig. 9-13. For reasons presented previously, the value employed for  $r^*$  is the measured spacing of the alloy carbides. As indicated in Table 6a the value of  $K_{Ic}$  based on equation (2) are in close agreement with the measured value in the case of the 200°C temper tested under static loading. However, under dynamic loading the fracture toughness is considerably greater than it is quasi-statically, and this is not reflected in the calculated value of  $K_{Ic}$ . This may be explained, at least in part, by the

fact that only static values are available for the various parameters in equation (2). The only exception is  $\sigma_y$  whose value is based on the yield-stress in shear obtained at a strain rate of  $10^3/s$ . It seems likely that the void nucleation and coalescence process involved in ductile fracture will be time-dependent. This means that the coefficient relating  $\delta_t$  to  $J/\sigma_y$  in equation (1) is itself rate-dependent. For the proposed model to predict an increase of 50% in the plane strain fracture toughness at the dynamic loading rate, requires that this coefficient be reduced from 0.67 to about 0.25. This would be the case, for instance, if the value of the dynamic  $\delta_t$  were set by keeping the ratio of crack mouth opening displacement  $\delta$  to crack tip opening displacement  $\delta_t$  the same for dynamic fracture as for quasi-static, rather than being derived directly from equation (1). This would make the calculated value of  $K_{Id} = 67 \text{ MPa}\sqrt{\text{m}}$ .

For the 350°C temper, the agreement between calculated and measured values of  $K_I$  is not as good, even for static fracture. The dimensions of the cementite particles that precipitate during the tempering treatment were approximately  $0.3\mu\text{m}$ . These correlate well with the size of undissolved carbides and are large enough to initiate the microvoids near the sharp cracks. Therefore, a significantly lower value for calculated fracture toughness is expected due to a decrease in the spacing of carbides including cementite particles. However, it also appears that competing mechanisms exist in this case; a decrease in  $K_{Ic}$  brought about by decreased particle spacing is accompanied by the beneficial effect of softening on tempering at 350°C. The values of  $K_{Ic}$  calculated using this model is different from the measured values when either the mode of fracture initiation is not entirely fibrous or the coefficient relating  $\delta_t$  to  $J/\sigma_y$  in equation (1) is not available for the dynamic loading rate. However, the values of  $K_{Ic}$  calculated employing this model is in close agreement with the measured value when values are available for various parameters used in equation (2).

### (b) Quasi-Cleavage Fracture Initiation

Quasi-cleavage was observed in the fractographs of tests performed at lower temperatures. Frequently, in steels, quasi-cleavage is initiated by prior microcracking at carbide or other inclusions. The critical microstructural feature involved in the quasi-cleavage of martensitic steel is the submicron size alloy carbide from which a crack initiates and then propagates catastrophically. Measurements based on the fractographic results indicate that the distance between the ridges of the cleaved facets lie approximately in the range of 2  $\mu\text{m}$  to 7  $\mu\text{m}$ , values consistent with the measured spacing of alloy carbide particles. The critical crack size for quasi-cleavage crack initiation would be very small with a mean size of 0.125 $\mu\text{m}$  because alloy carbides are in the range from 0.05 $\mu\text{m}$  to 0.2 $\mu\text{m}$ .

An attempt was made to model fracture in the quasi-cleavage mode following the work of Couque et al [20] in which a quasi-cleavage fracture is assumed to occur when the applied tensile stress reaches a critical value,  $\sigma_f^*$ . When critical crack size is 0.125 $\mu\text{m}$ ,  $\sigma_f^*$  is approximately 5600 MPa [34,35,36].

Rice and Johnson [32], employing power law stress-strain relation, obtained numerical values of the expected stress increase of a blunting crack. Their analysis includes both the effects of a strain hardening exponent  $n$  and of an initial yield strain  $\sigma_y/E$  to show that local stresses can reach a maximum of from 3 to 5 times the yield stress of the material. In particular, the maximum stress attained is 3 times the yield stress for a yield strain of 0.0075 and for  $n = 0.01$ , which represents a very low hardening rate. These values approximate the conditions seen at fracture initiation either statically or dynamically for the 200°C temper steel tested at -100°C. The values of  $\sigma_f^*$  at these data points are 5950 MPa for quasi-static loading and 5400 MPa for dynamic loading.

Once  $\sigma_f^*$  is known with some certainty, it is possible to estimate the resulting value of  $K_{IC}$  and its dependence on temperature and loading rate. As mentioned

above, the model postulates that fracture initiation, and thus  $K_{Ic}$ , will be determined by the requirement that the maximum principal stress at the crack tip,  $\sigma_{yy}$ , equals or exceeds  $\sigma_f^*$  over some microstructurally significant distance. The stress analysis used in the present study is due to Ostergren's finite element solution for a non-hardening material under conditions of SSY (Fig. 6a of ref. [34]). This analysis gives the stress intensification (the ratio of maximum tensile stress to uniaxial yield stress), at a point  $X$  ahead of the crack tip, as a function of the dimensionless quantity  $X/(K/\sigma_y)^2$ . A fracture toughness value was calculated using the value of  $\sigma_f^* \approx 5600$  MPa, critical distance of  $X = 3\mu\text{m}$  and the value of yield stress,  $\sigma_y = 1803$  MPa under dynamic loading and  $\sigma_y = 1983$  MPa under quasi-static loading. Results of calculations for the 200°C temper at the test temperature of -100°C are given in Table 6b and compared with experimental values. It shows that this model predicts a large difference in quasi-static and dynamic stress intensity factors at -100°C. At this temperature the yield stress is high so that the stress intensification ahead of a sharp crack is approximately 3. The calculated value of  $K_{Id}$  is lower than the measured value at this temperature since the model assumes that cleavage is the dominant mode of initiation, whereas there is a considerable increase in the percentage of fibrous fracture in the initiation zone at the higher loading rate (Fig. 34). This favorable correlation between measured and calculated values of  $K_{Ic}$  and  $K_{Id}$  for this high-strength steel is encouraging and warrants further investigations of the application of this quasi-cleavage fracture initiation model introduced by RKR and subsequently employed by Couque et al. [20, 34]. In particular, the model should be applicable to fractures at lower temperatures. At these temperatures, fracture initiation will be entirely by cleavage, and the model will give lower values for  $K_{Id}$  and  $K_{Ic}$ , since the yield stress is higher, stress intensification is lower and in turn the ratio  $X/(K/\sigma_y)^2$  is larger.



#### IV. CONCLUSIONS

Quasi-static and dynamic fracture initiation tests were performed with specimens of three different tempers of an AISI 4340 VAR steel, having hardnesses of 55, 49, and 45 on the Rockwell C scale. The specimens consisted of prefatigued notched round bars loaded in tension, thus providing plane strain conditions at the fracture site. Tests were performed over the temperature range  $-140^{\circ}\text{C}$  to  $+100^{\circ}\text{C}$ . For dynamic fracture, the fracture site was loaded by a sharp-fronted tensile pulse initiated explosively at the end of the bar. The dynamic loading rate attained by this method provides a value of  $\dot{K}_I$  of about  $10^6 \text{ MPa}\sqrt{\text{m}}/\text{s}$  as compared with  $1 \text{ MPa}\sqrt{\text{m}}/\text{s}$  in a quasi-static test. The above fracture initiation tests were supplemented by Charpy tests, as well as by static and dynamic stress-strain tests performed at  $-100^{\circ}\text{C}$ , room temperature, and  $+100^{\circ}\text{C}$ .

The results show that this AISI 4340 VAR steel is tougher under dynamic loading than for static loading for all three tempers and, with one exception, over the entire temperature range. In fact, at the higher test temperatures the steel is considerably tougher dynamically than statically. The results presented establish the lower and upper shelf levels for all three tempers, although under dynamic loading the lower shelf is more clearly defined than the upper. As expected, dynamic loading results in a shift of the ductile-to-brittle transition temperature toward higher temperatures.

One of the tempering temperatures ( $350^{\circ}\text{C}$ , RHC = 49) was chosen to provide a steel whose properties would be characteristic of tempered martensite embrittlement (TME). The Charpy test results for this steel show a trough in the CVN energy as a function of tempering temperature, although the difference between the energy value for the  $350^{\circ}\text{C}$  temper is only slightly lower than for the  $200^{\circ}\text{C}$  temper. In

contrast, plane strain fracture testing does not provide a trough in tests at room temperature but does for tests at lower temperatures with a more pronounced trough under dynamic loading.

The influence of strain rate on the flow stress level in shear is not pronounced, with the possible exception of the 200°C temper at the lower and higher test temperatures. However, strain rate does have a strong influence on the ductility of the material. For instance, for the 200°C temper at room temperature, deformation at a rate of  $10^3/s$  results in fracture at a shear strain of about 20%, whereas in quasi-static deformation the specimen fractures only at strains greater than 50%.

Microscopic observations of the fracture surface of the specimen reveal that the effect of loading rate on the mode of fracture initiation is small. As expected, specimens tempered at 350°C and tested at the lower temperatures showed a higher percentage of intergranular fracture initiation than specimens tempered at 200°C or 425°C. In addition, transmission electron microscopy revealed the presence of cementite along the lath boundaries of the steel tempered at 350°C. An attempt was made to model the fracture behavior based on microstructural parameters. Some success was attained in modeling fracture on the lower shelf. It appears, that for ductile fracture, a more sophisticated model is required to represent the more complicated microstructure of the present steel.

### Acknowledgements

The research support of the Army Research Office under Grant DAAL03-88-K-0015 and the NSF Materials Research Laboratory at Brown University are gratefully acknowledged. The technical assistance of G.J. LaBonte, Jr., is also appreciated.

## References

- [1] L.S. Costin, J. Duffy and L.B. Freund: "Fracture Initiation in Metals Under Stress Wave Loading Conditions", *ASTM STP 627*, 1977, p. 301.
- [2] L.S. Costin, W.L. Server and J. Duffy: "Dynamic Fracture Initiation: Comparison of Two Experimental Methods", *Trans. of ASME 101, J. of Eng. Mat. and Tech.*, 1979, p. 168.
- [3] M.L. Wilson, R.H. Hawley and J. Duffy: "The Effect of Loading Rate and Temperature on Fracture Initiation in 1020 Hot-Rolled Steel", *Eng. Frac. Mech.*, 1980, Vol. 13, p. 371.
- [4] H. Couque, J. Duffy and R.J. Asaro: "Effects of Prior Austenite and Ferrite Grain Size on Fracture Properties of a Plain Carbon Steel", Brown University Technical Report DAAG29-81-K-0121/7, 1984.
- [5] R. Dormeival, J.M. Chevallier and M. Stelly: "Fracture Initiation of Metals at High Loading Rates", presented at the Fifth International Conference on Fracture, Cannes, France, 1981.
- [6] D.A. Shockey, H. Hemma and Y. Murayama: "Response of Cracks in Structural Materials to Short Pulse Loads", Poulter Laboratory Technical Report 005-82, SRI International, Menlo Park, California, September, 1982.
- [7] T. Nakamura, C.F. Shih and L.B. Freund: "Elastic-Plastic Analysis of a Dynamically Loaded Circumferentially Notched Round Bar", *Eng. Frac. Mech.*, Vol. 22, 1985, p. 437.
- [8] E.M. Hackett: "An Investigation of the Environmental Cracking Susceptibility of a High Strength Steel Using J-integral Techniques", Ship Materials Engineering Department Research and Development Report, March 1985.
- [9] S.K. Banerji, C.J. McMahon, Jr. and H.C. Feng: "Intergranular Fracture in 4340-Type Steels: Effects of Impurities and Hydrogen", *Met. Trans. A.*, Vol. 9A, 1978, p. 237.
- [10] J.P. Materkowski and G. Krauss: "Tempered Martensite Embrittlement in SAE 4340 Steel", *Met. Trans.A.*, Vol. 10A, 1979, p. 1643.
- [11] C.L. Briant and S.K. Banerji: "Tempered Martensite Embrittlement in Phosphorus Doped Steels", *Met. Trans. A*, Vol. 10A, 1979, p. 1729.
- [12] J. Duffy, J.D. Campbell and R.H. Hawley: "On the Use of a Torsional Split Hopkinson Bar to Study Rate Effects in 1100-0 Aluminum", *J. Appl. Mech.*, 1971, Vol. 38, p. 83.
- [13] L.S. Costin, E.E. Crisman, R.H. Hawley and J. Duffy: *Proc. 2nd Conf. Mechancial Properties at High Rates of Strain*, ed. J. Harding, 1979, p. 90.
- [14] Y.V. Murty, J.E. Morral, T.Z. Kattamis, and R. Mehrabian: "Initial Coarsening of Manganese Sulfide Inclusions in Rolled Steel During Homogenization", *Met. Trans. A*, Vol. 6A, 1975, p. 2031.

- [15] C.F. Hickey and A.A. Anctil: "Split Heat Mechanical Property Comparison of ESR and VAR 4340 Steel", AMMRC TR83-27, 1983.
- [16] H. Kolsky: *Proc. Phys. Soc. London*, 62-B, 1949, p. 676.
- [17] H. Tada, P.C. Paris and G.R. Irwin: in *The Stress Analysis of Cracks Handbook*, Del Research Corp. Hellertown, Pennsylvania, 1973.
- [18] P.C. Paris: in written discussion to J.A. Begley and J.D. Landes: *ASTM STP 514*, 1972, p. 1.
- [19] J.R. Rice, P.C. Paris and J.G. Merkle: "Some Further Results of J-Integral Analysis and Estimates", *ASTM STP 536*, 1973, p. 231.
- [20] H. Couque, R.J. Asaro, J. Duffy and S. Lee: "Correlations of Microstructure with Dynamic and Quasi-Static Fracture in a Plain Carbon Steel", to appear in *Met. Trans. A*.
- [21] S. Tanimura and J. Duffy: "Strain Rate Effects and Temperature History Effects for Three Different Tempers of 4340 VAR Steel", *Int. J. of Plasticity*, 2, 1986, p. 21.
- [22] D.P. Kendall and T.E. Davidson: "The Effect of Strain Rate on Yielding in High Strength Steels", *J. of Basic Eng.*, 1966, p. 37 Vol. 9A, 1978, p. 237.
- [23] M.J. Manjoine: "Influence of Rate of Strain and Temperature on Yield Stresses of Mild Steel", *J. Appl. Mech.*, 1944, A211.
- [24] G. Ravichandran and R.J. Clifton: "Dynamic Fracture Under Plane Wave Loading," to appear in *Int. Journal of Fracture*.
- [25] R. Godse, G. Ravichandran and R.J. Clifton: "Micromechanisms of Dynamic Crack Propagation in an AISI 4340 Steel", Brown University Technical Report DAAL03-88-K-0015, 1988.
- [26] J.E. King, R.F. Smith and J.F. Knott: "Toughness Variations During the Tempering of a Plain Carbon, Martensitic Steel", *Fracture 1977*, Vol. 2, ICF4, Waterloo, Canada, 1977, p. 279.
- [27] E.B. Kula and A.A. Anctil: "Tempered Martensite Embrittlement and Fracture Toughness in SAE 4340 Steel", *J. of Mater.*, Vol. 4, 1969, p. 817.
- [28] S. Lee, L. Majno and R.J. Asaro: "Correlation of Microstructure and Fracture Toughness in Two 4340 Steels", *Met. Trans. A.*, Vol. 16A, 1985, p. 1633
- [29] S. Lee: "Correlation of Microstructure and Fracture Toughness in Two 4340 Steels", Ph.D. Thesis, Brown University, May 1986.
- [30] M.F. Carlson, B.V. Narasimha Rao and G. Thomas: "The Effect of Austenitizing Temperature upon the Microstructure and Mechanical Properties of Experimental Fe/Cr/C Steels", *Met. Trans. A.*, Vol. 10A, 1979, p. 1273.

- [31] N. Bandyopadhyay and C.J. McMahon: "The Micro-Mechanisms of Tempered Martensite Embrittlement in 4340-Type Steels", *Met. Trans. A*, Vol. 14A, 1983, p. 1313.
- [32] J.R. Rice and M.A. Johnson: "The Role of Large Crack Tip Geometry Change in Plane Strain Fracture", in *Inelastic Behavior of Solids*, ed. M.F. Kanninen et al., McGraw-Hill, New York, NY, 1970.
- [33] R.M. McMeeking: "Finite Deformation Analysis of Crack-Tip Opening in Elastic-Plastic Materials and Implications for Fracture", *J. Mech. Phys. Solids*, Vol. 25, 1977, p. 357
- [34] R.O. Ritchie, J.F. Knott and J.R. Rice: "On the Relationship Between Critical Tensile Stress and Fracture Toughness in Mild Steel", *J. Mech. Phys. Solids*, Vol. 21, 1973, p. 395.
- [35] J.D.G. Groom and J.F. Knott: "Cleavage Fracture in Prestrained Mild Steel", *Metal Science*, Vol. 9, 1975, p. 390.
- [36] J.F. Knott: "Some Effects of Hydrostatic Tension on the Fracture Behavior of Mild Steel", *J. Iron Steel Inst.*, 204, 1966, p. 104.

B:Chi/rpt.wp  
Imp 8/02/88  
Peg's machine

Table 1. Chemical composition of the AISI 4340 VAR steel. Data from Republic Steel:  
Heat No. 3841687 (Weight percent of 4340 steel alloy).

C	Mn	P	S	Si	Cu	Ni	Cr	Mo	Al	N	O	H ppm
.42	.46	.009	.001	.28	.19	1.74	.89	.21	.031	.005	.001	1.0

Table 2. Heat Treatments.

	Temperature (°C)	Time (hours)	Cooling	Rockwell Hardness C
Normalize	900	1	Air Cool	
Austenitize	845	1	Oil Quench	
Temper	200	1	Air Cool	55
	350	1	Oil Quench	49
	425	1	Oil Quench	45

Table 3. Values of the axial flow stress for the three different tempers based on results of shear tests with the torsional Kolsky bar, Figure 7. Axial stress values are calculated from the corresponding shear stress using  $\sigma = \sqrt{3}\tau$ . The strain hardening exponent  $n$  is defined by  $\sigma/\sigma_y = \alpha(\epsilon/\epsilon_y)^n$ .

TEMPER ( ° C)	TEST TEMP ( ° C)	$\sigma_d$ (MPa)				$\sigma_s$ (MPa)			
		$n$	.2%offset	$\bar{\epsilon} = .05$	ultimate	$n$	.2%offset	$\bar{\epsilon} = .05$	ultimate
200	-100	0.12 to 0.01	1803	2125	2245	0.01	1983	2460	2771
	RT	0.1 to 0.01	1708	2018	2103	0.01	1637	1983	2220
	+100	0.1 to 0.01	1350	1648	1671	0.01	1558	2006	2305
350	-100	0.06	1576	1671	1671	0.01	1469	1648	1708
	RT	0.04	1469	1612	1654	0.01	1368	1576	1613
	+100	0.06	1432	1576	1600	0.01	1254	1505	1613
425	-100	0.06	1541	1565	1625	0.01	1350	1529	1637
	RT	0.04	1456	1433	1469	0.01	1195	1326	1338
	+100	0.035	1337	1433	1469	0.01	1170	1373	1493



Table 4. Results of the SEM fractography showing the mode of fracture initiation. F, Q, and I refer to the appearance of the fracture surface i.e., fibrous, quasi-cleavage or intergranular.

Temper & Loading Rate	Testing Temp. (°C)	Specimen Number	Stress Intensity Factor, $K_I$ (MPa $\sqrt{m}$ )	Mode of Fracture	Percent Fracture		
					F	Q	I
200 °C dynamic	-140	VF 40-1	47	F (+Q)	15	82	2
	-100	VF 33-1	54	F (+Q)	50	47	3
	-50	VF 29-1	60	F (+Q)	70	27	3
	RT	VF 12-1	69	F	97	0	3
	+100	VF 101-1	94	F	100	0	0
200 °C static	-140	VS 53-1	21	F (+Q)	10	87	3
	-100	VS 54-1	21	F (+Q)	12	85	3
	-50	VS 50-1	34	F (+Q)	30	65	5
	RT	VS 4-1	46	F (+I)	85	0	15
	+100	VS 71-1	42	F (+I)	80	0	20
350 °C dynamic	-140	VF 86-3	34	Q + I	0	55	45
	-100	VF 93-3	31	Q + I	0	50	50
	-50	VF 83-3	41	Q + F + I	20	40	40
	RT	VF 81-3	89	F (+I)	85	0	15
	+100	VF 82-3	115	F	90	0	10
350 °C static	-140	VS 76-3	18	Q + I	0	60	40
	-100	VS 78-3	23	Q + I	10	50	40
	-50	VS 75-3	31	Q + F + I	20	40	40
	RT	VS 77-3	59	F (+I)	90	0	10
	+100	VS 95-3	52	F (+I)	90	0	10
425 °C dynamic	-140	VF 21-2	42	Q + I	5	70	25
	-100	VF 11-2	45	Q + I	10	60	30
	-50	VF 2-2	55	F + Q + I	35	40	25
	RT	VF 15-2	130	F	96	0	4
425 °C static	-140	VS 68-2	23	Q + I	5	60	35
	-100	VS 60-2	34	Q + I	20	50	30
	-50	VS 65-2	88	F + Q + I	60	20	20
	RT	VS 70-2	98	F	95	0	5

**Table 5. Results of tensile tests with the circumferentially notched specimens  
(see Figure 8).**

Tempering Temp., °C	Testing Temp., °C	True Fracture Strain	Void Nucleation Strain
200	-140	0.14	0.10
	-50	0.29	0.17
	RT	0.30	0.17
350	-140	0.11	0.07
	RT	0.31	0.15
425	-140	0.24	0.06
	RT	0.35	0.13

Table 6. Calculated and measured fracture toughness values (a) employing a fibrous fracture initiation model and (b) employing a quasi-cleavage fracture initiation model.

(a)

Tempering Temp. (°C)	Loading Rate	$\sigma_y$ (MPa)	Equiv. Strain $\epsilon^*$	$(r / \delta_t)^*$	%Fib	Calculated $K_{Ic}$ or $K_{Id}$ (MPa $\sqrt{m}$ )	Measured $K_{Ic}$ or $K_{Id}$ (MPa $\sqrt{m}$ )
200	Static	1637	0.20	0.73	85	47	46
	Dynamic	1708	0.20	0.73	97	49	69
350	Static	1368	0.17	0.82	90	41	59
	Dynamic	1469	0.17	0.82	80	42	89

TESTED AT ROOM TEMPERATURE

$$K_{Ic} \approx \sqrt{\frac{1.64 \sigma_y E r^*}{(r / \delta_t)^*}} \quad r^* = 3 \mu m$$

(b)

Tempering Temp. (°C)	Loading Rate	$\sigma_y$ (MPa)	% of quasi-cleavage	$\sigma_f^* / \sigma_y$	$\frac{x}{(K / \sigma_y)^2}$	Calculated $K_{Ic}$ or $K_{Id}$ (MPa $\sqrt{m}$ )	Measured $K_{Ic}$ or $K_{Id}$ (MPa $\sqrt{m}$ )
200	Static	1983	85	2.8	0.015	28	21
	Dynamic	1803	47	3.1	0.004	49	54

TESTED AT -100 °C

$$\sigma_f^* \approx \sqrt{\frac{4 E \delta_{eff}}{\pi (1 - \nu^2) c}} \approx 5600 \text{ MPa} \quad c \approx 0.125 \mu m \quad x \approx 3 \mu m$$

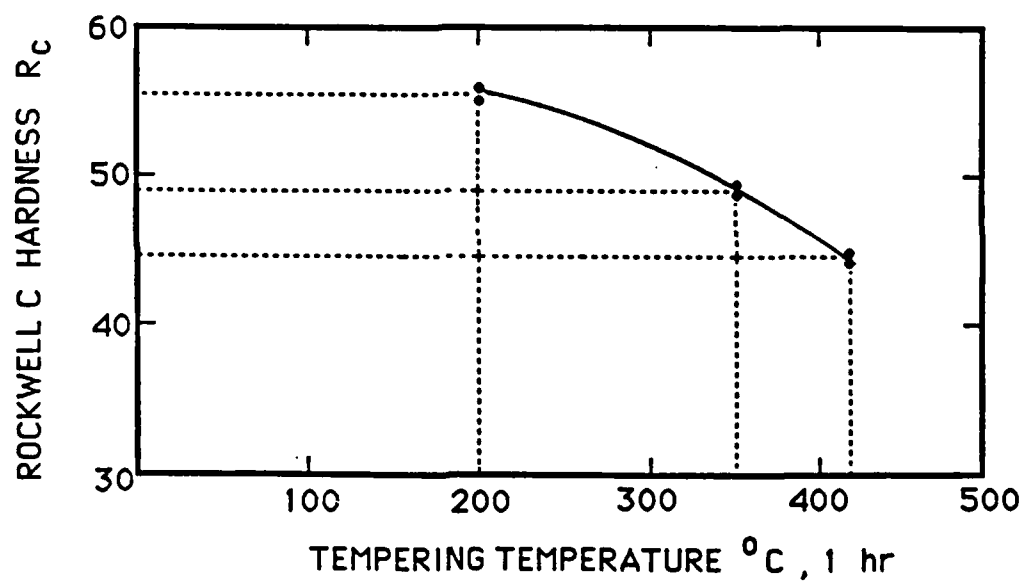
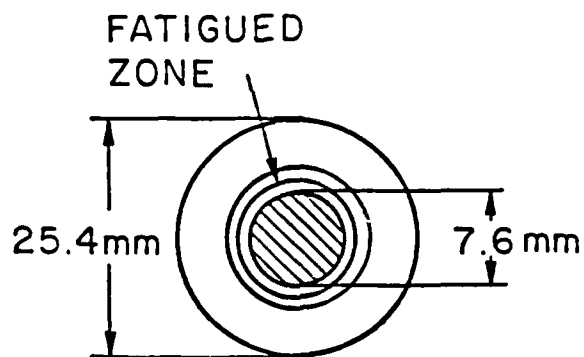
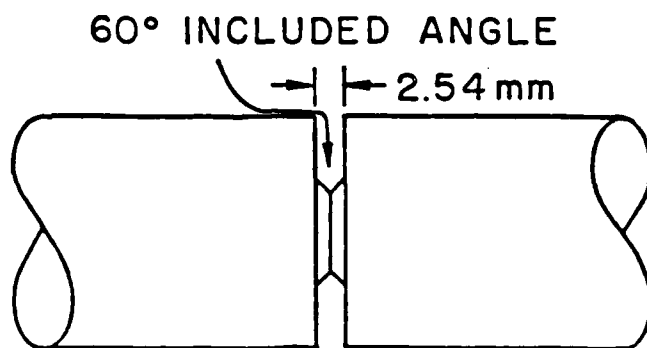


Fig. 1. The effect of tempering temperature on the hardness of the 4340 VAR steel.



#### SECTION THROUGH NOTCH

Fig. 2. The notched section of the specimen, showing the ligament remaining after fatigue (7.6 mm in diameter).

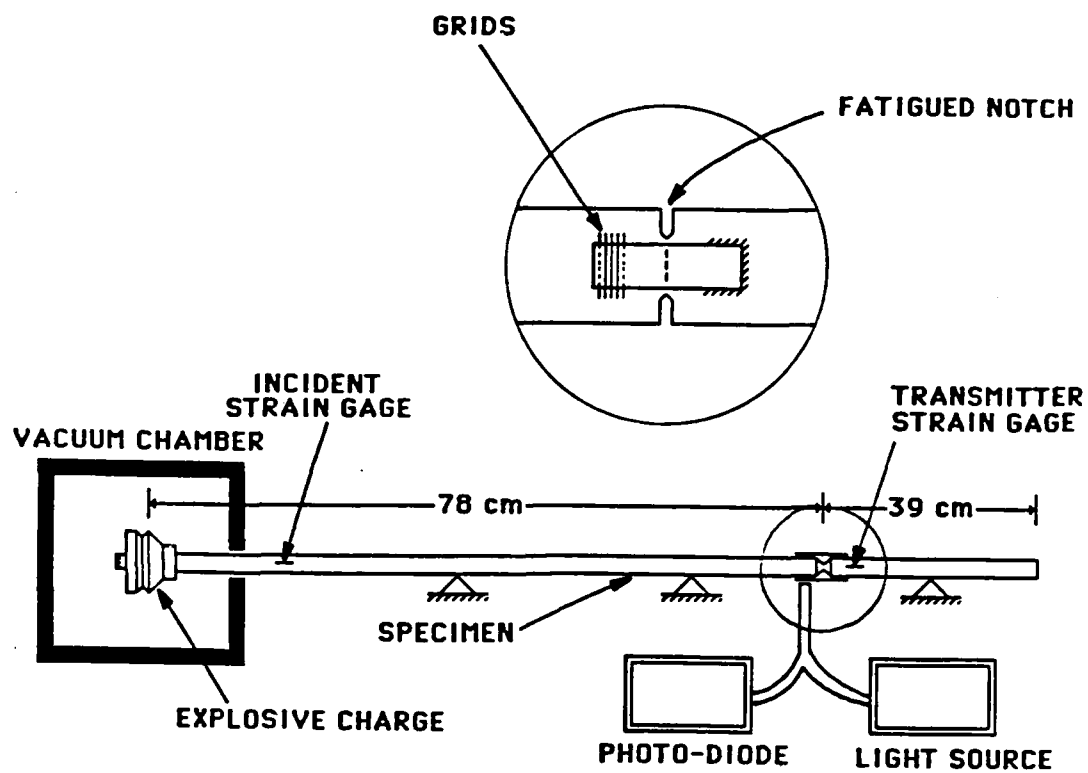


Fig. 3. Schematic diagram of the apparatus employed for the dynamic fracture initiation experiments.

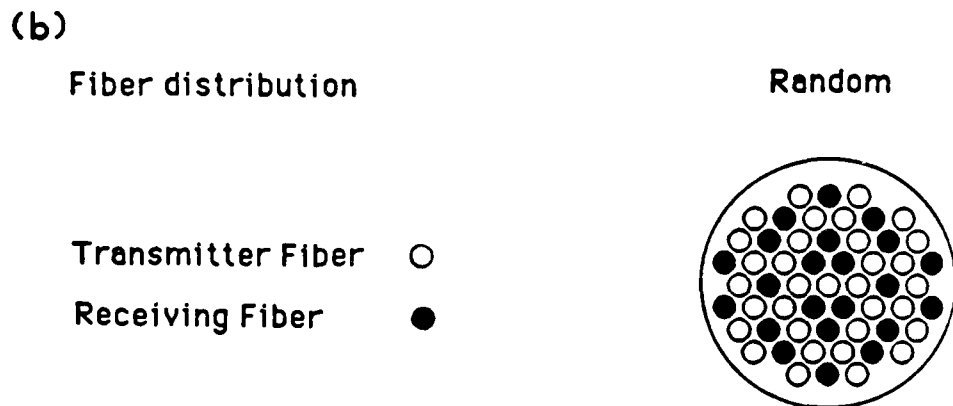
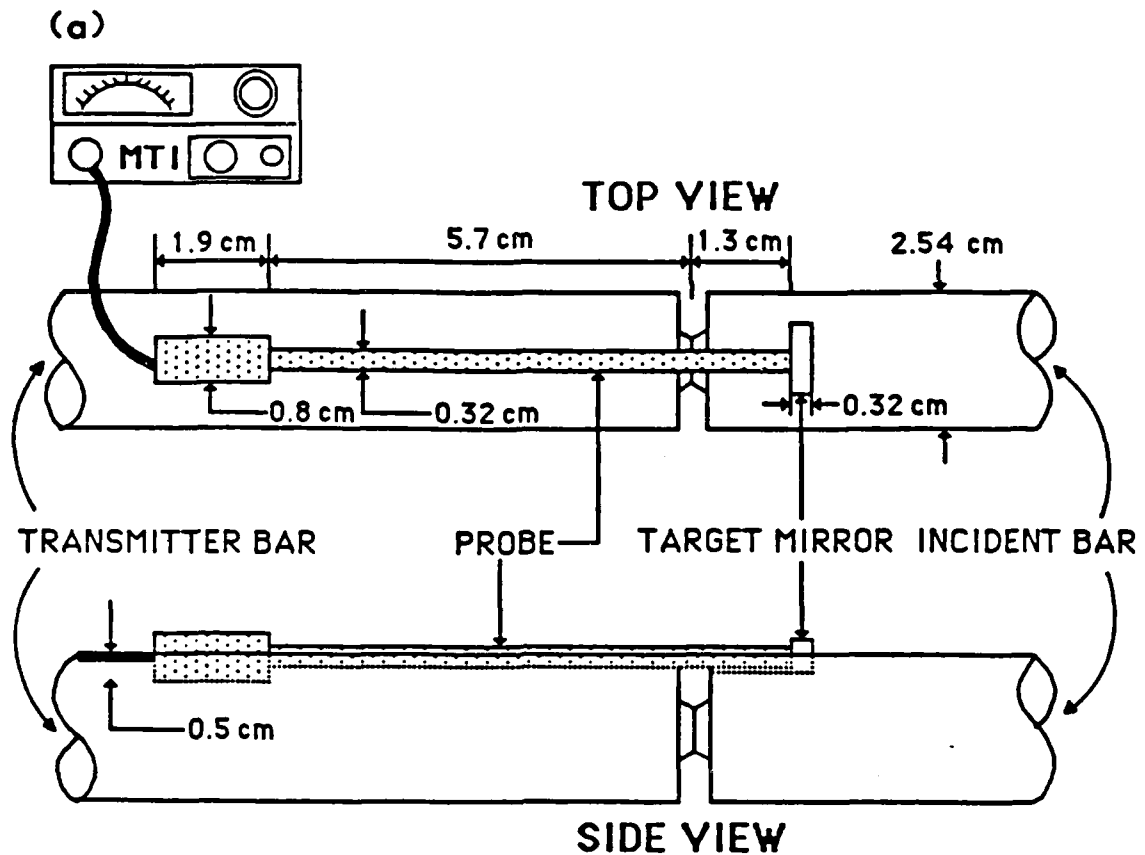


Fig. 4. (a). Schematic diagram showing an MTI photonic sensor used to measure the crack opening displacement (The figure shows the arrangement used for dynamic testing when the probe is placed within a groove cut in the bar. In static tests the apparatus is fixed to the curved surface of the bar). (b). Fiber distribution of the MTI optical probe employed.

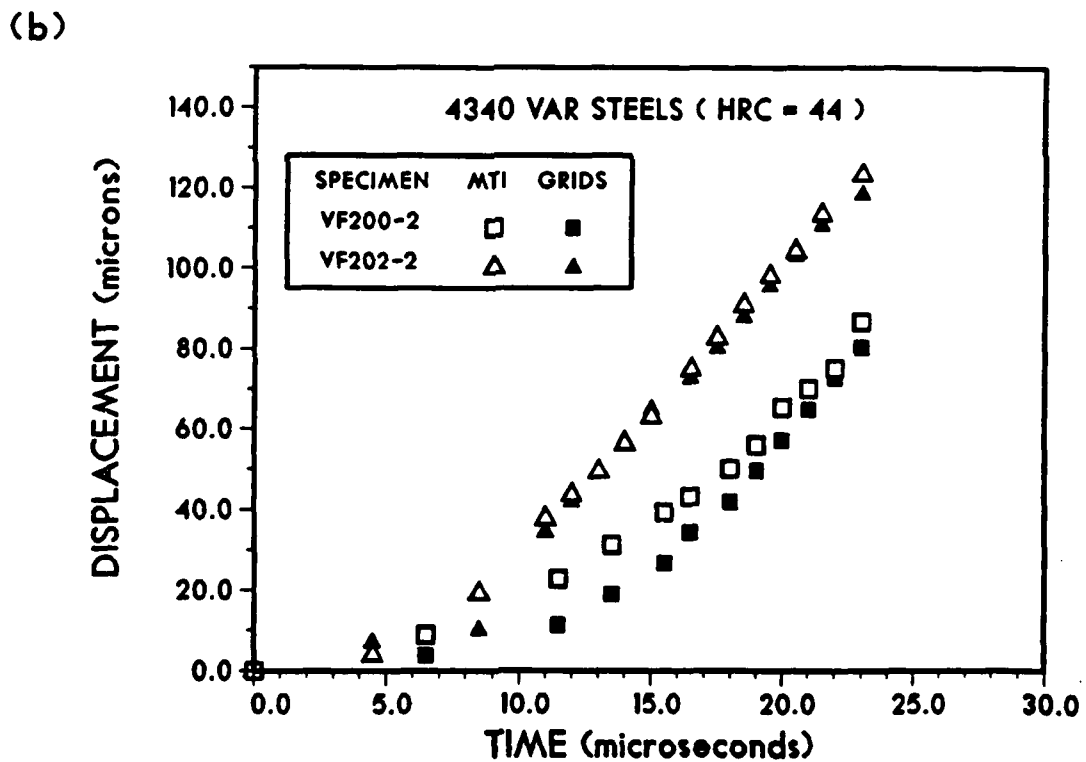
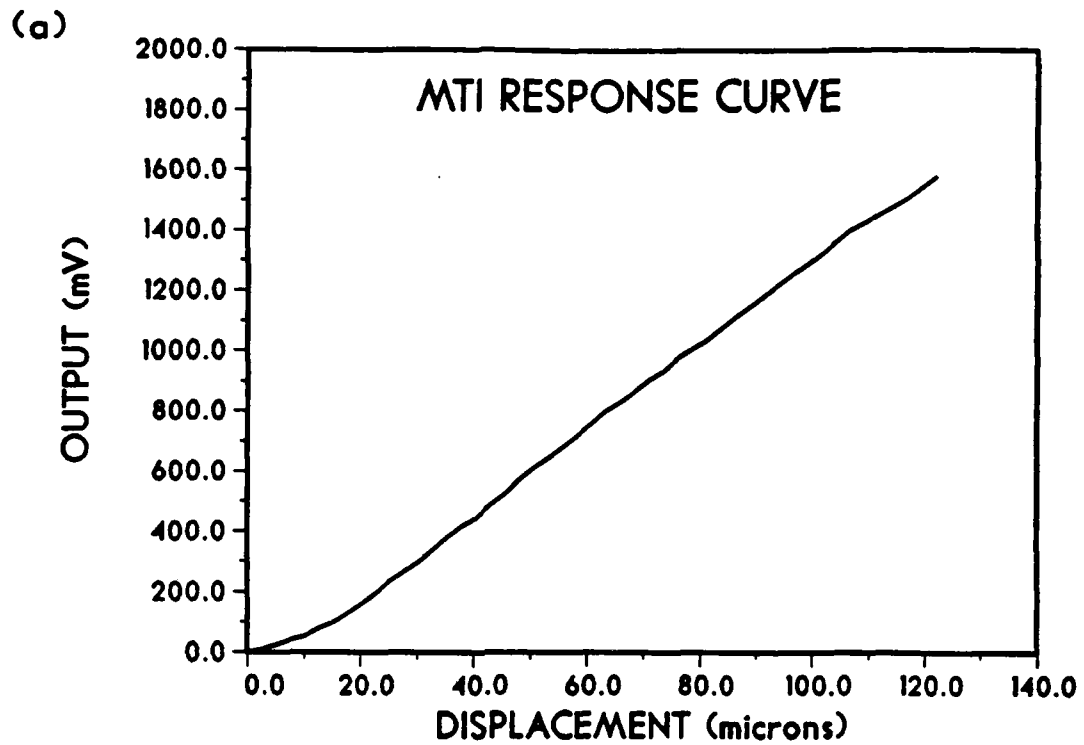


Fig. 5. (a). Response curve of the MTI photonic sensor in the region of our interest.  
(b). A comparison of the displacement response of the MTI sensor with the moire grids in two dynamic fracture tests.



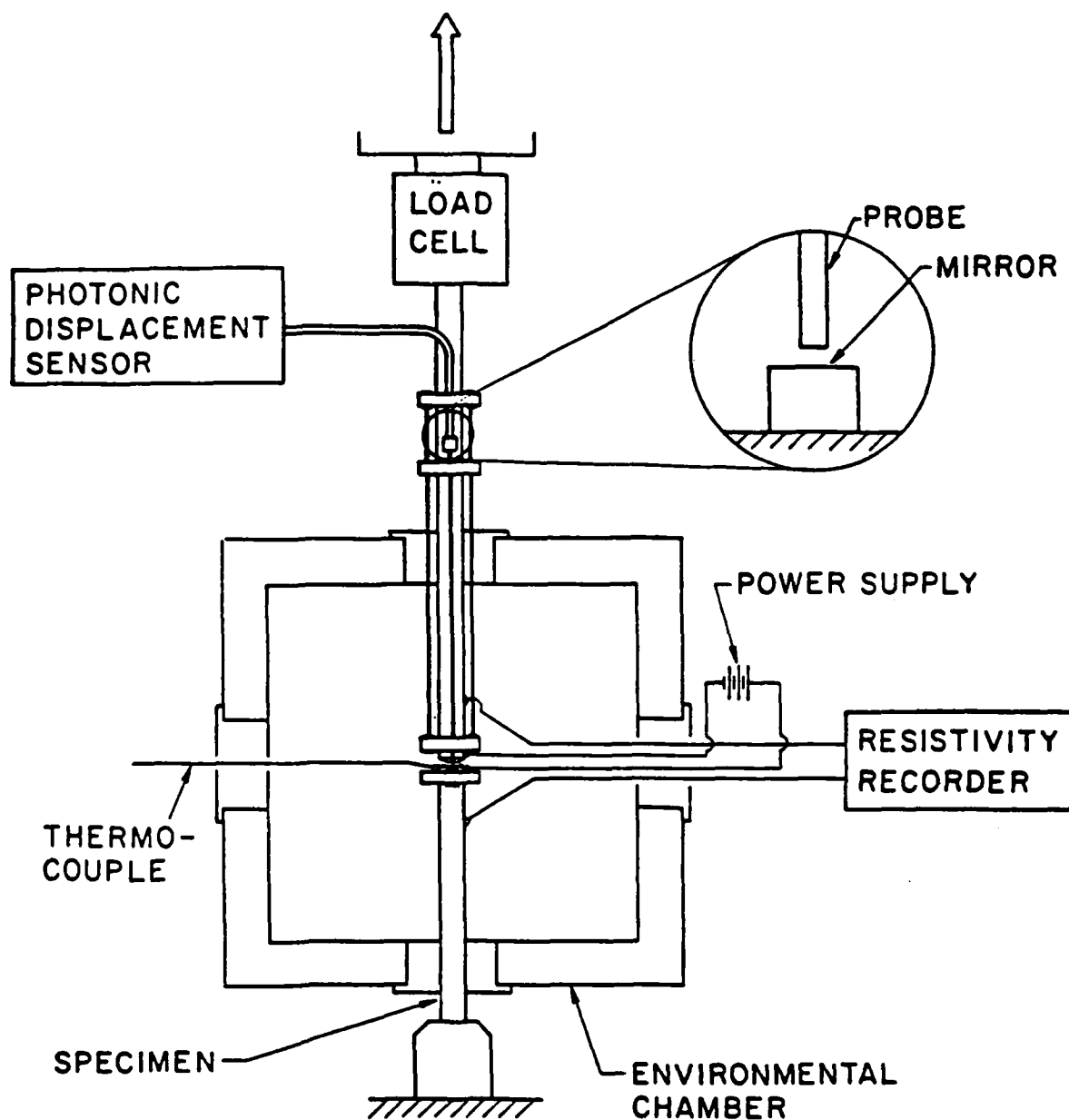
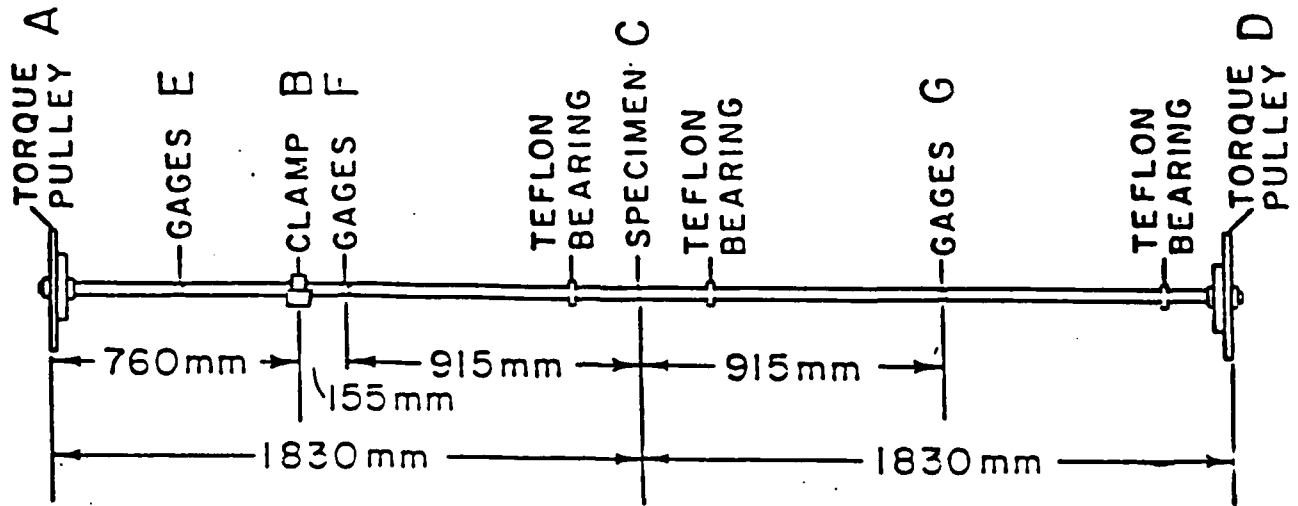
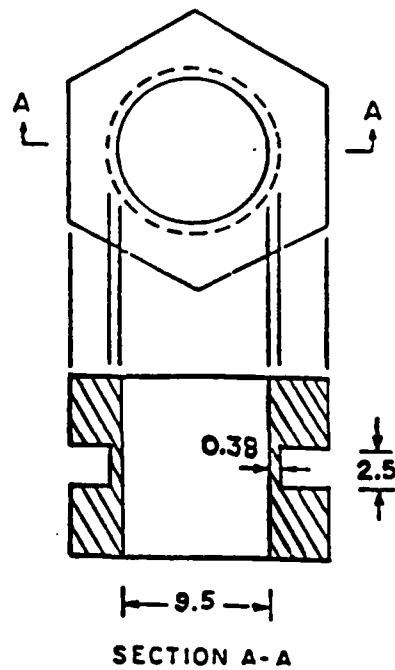


Fig. 6. Schematic diagram of the apparatus employed for the static fracture initiation experiment. The load is applied in a Riehle testing machine. Crack opening displacement is measured by means of the MTI probe shown in the inset.



(a) Torsional Kolsky bar



(b) Torsion specimen

Fig. 7. Schematic diagram showing: (a) The torsional Kolsky bar used to determine the dynamic stress-strain behavior of the steels and (b) the specimen used in this apparatus. The dimensions are in millimeters.

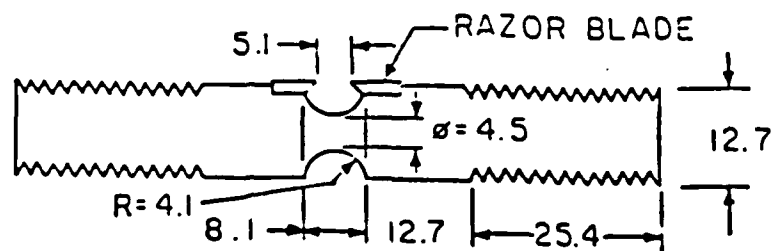


Fig. 8. The circumferentially notched tensile specimen employed to determine the strain at which voids initiate. The dimensions are in millimeters.

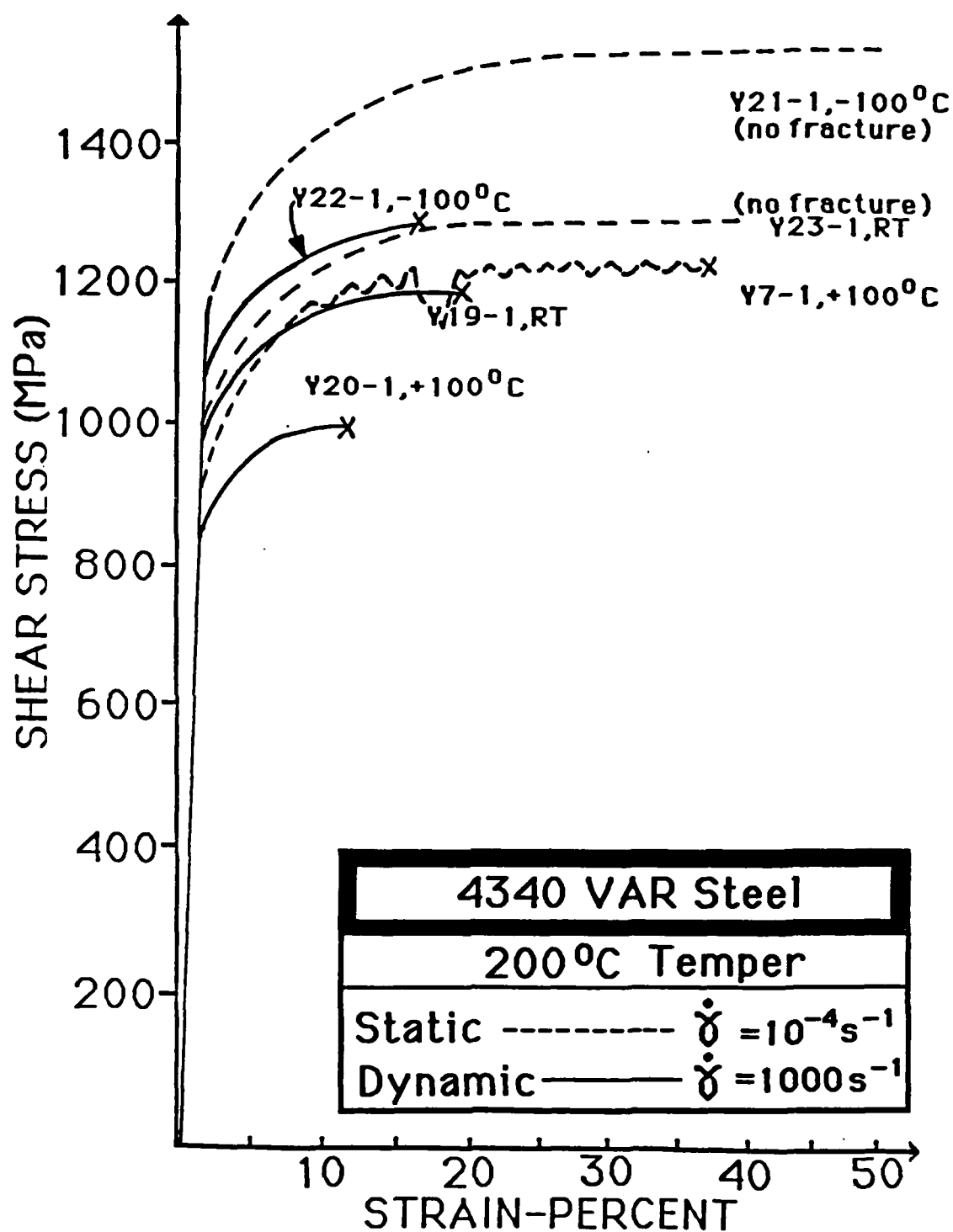


Fig. 9. Static and dynamic stress-strain behavior in shear for the 200°C temper.

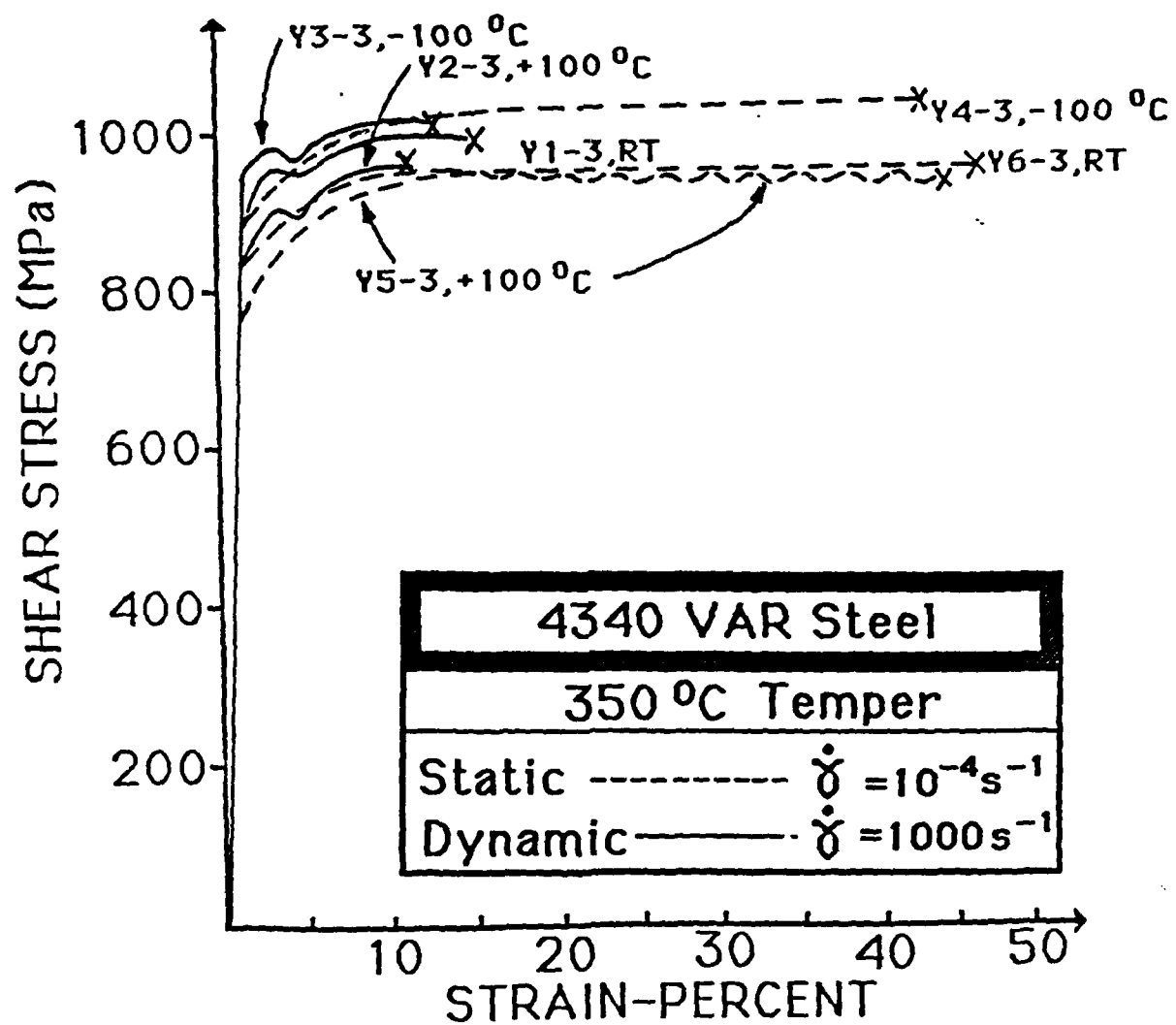


Fig. 10. Static and dynamic stress-strain behavior in shear for the 350°C temper.

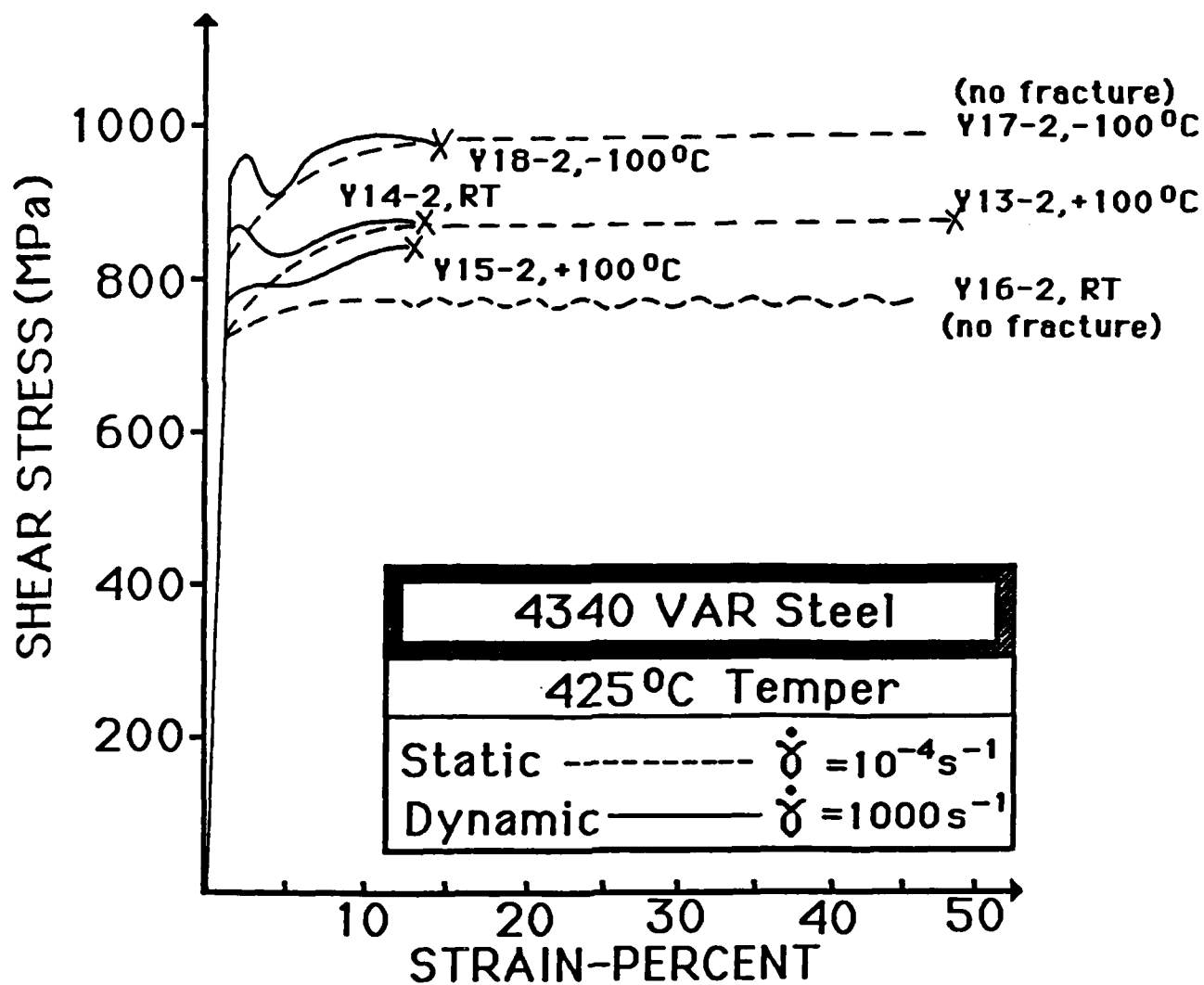


Fig. 11. Static and dynamic stress-strain behavior in shear for the 425°C temper.

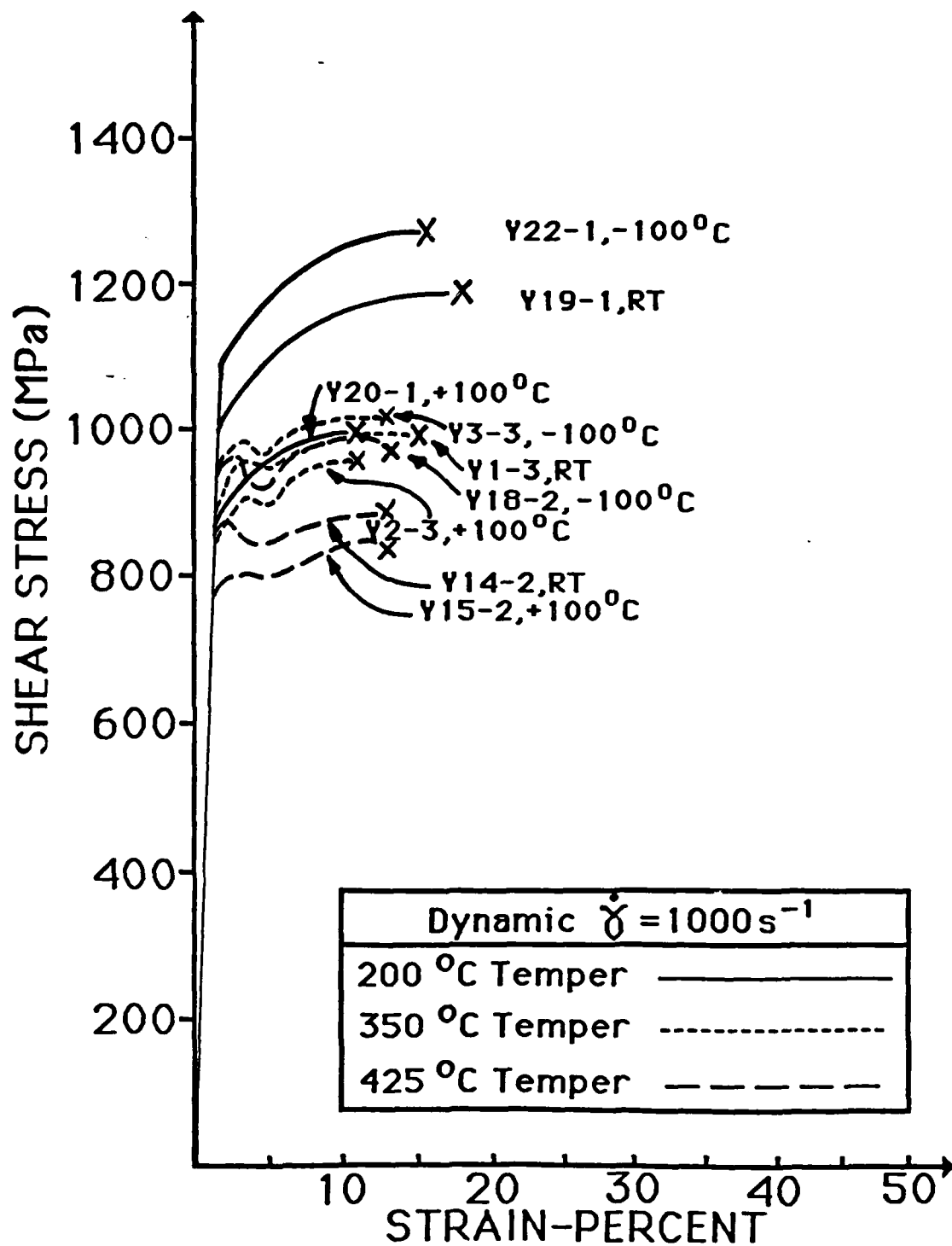


Fig. 12. Dynamic stress-strain behavior in shear for the three tempers of the 4340 VAR steel.

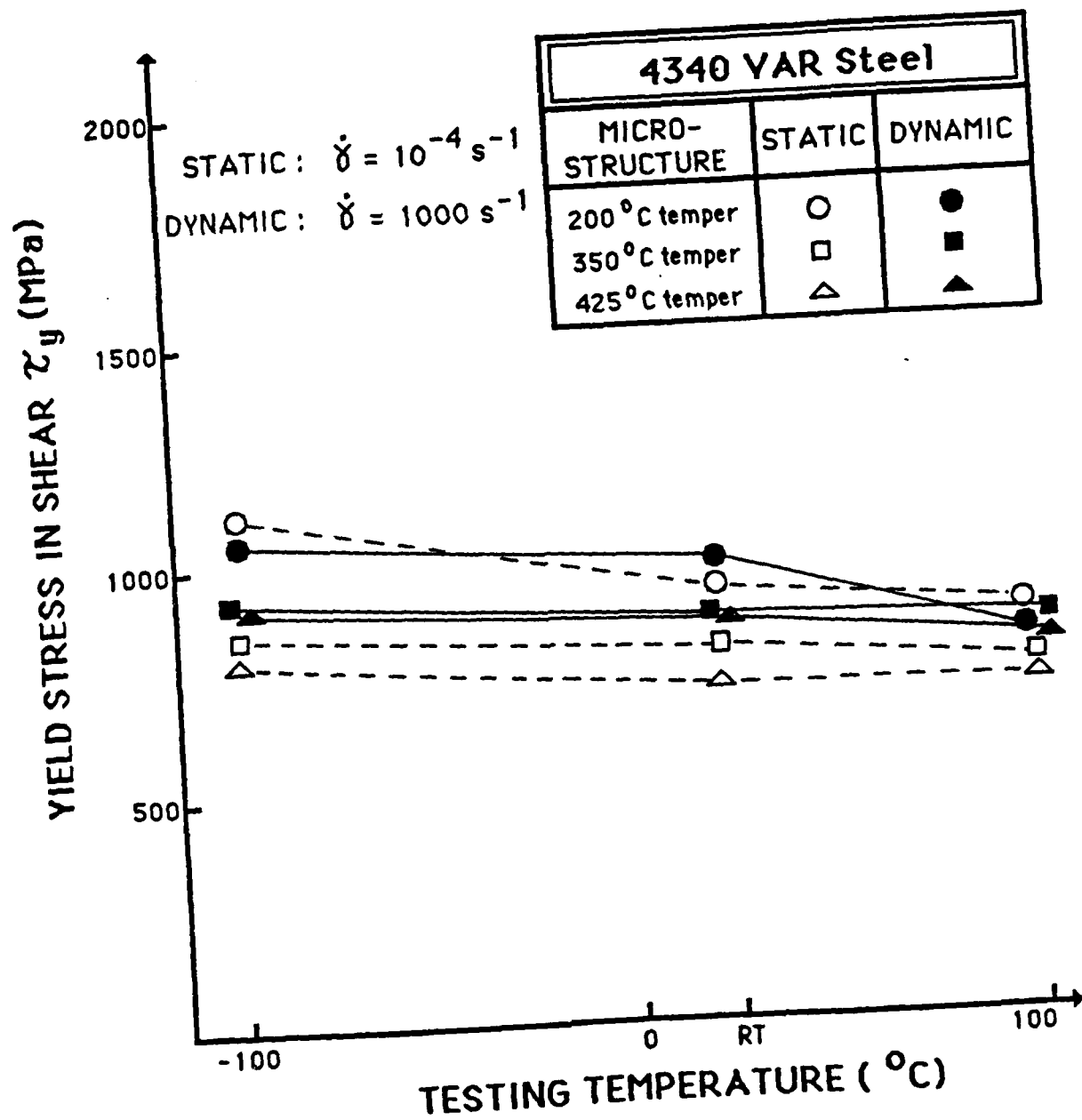


Fig. 13. The yield stress in shear at a 0.2 percent offset as a function of test temperature.



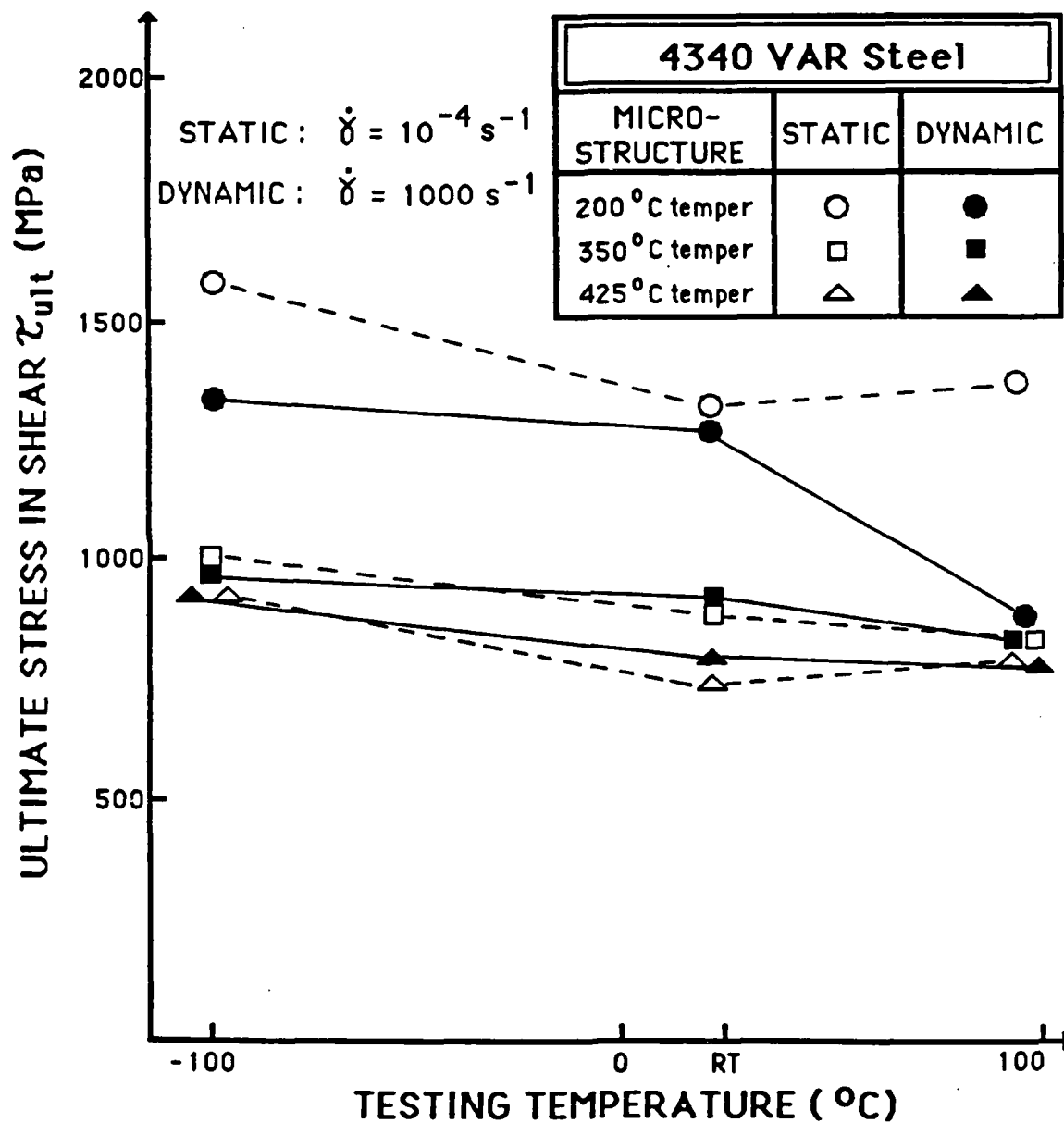


Fig. 14. The ultimate stress in shear as a function of test temperature.

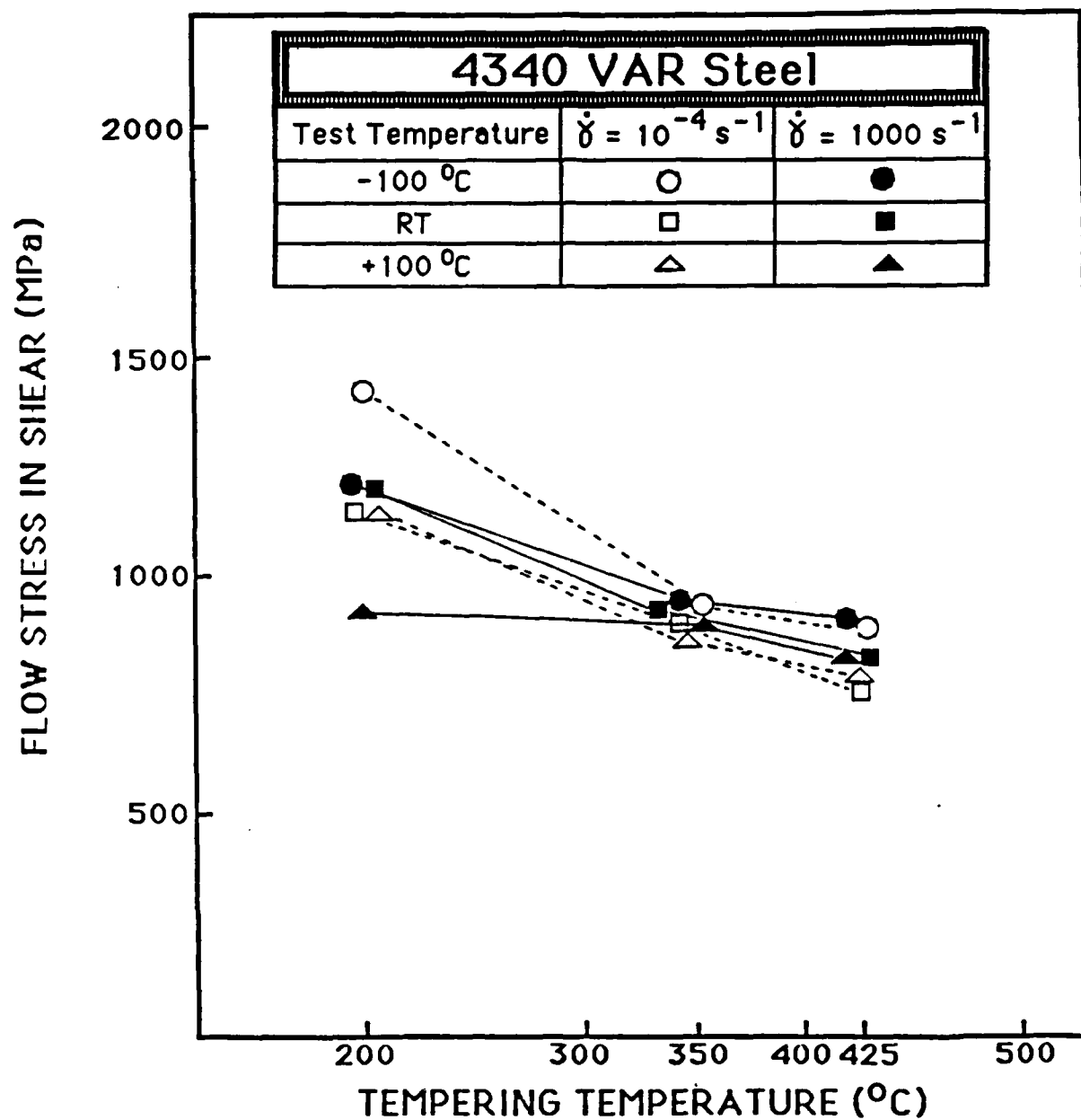


Fig. 15. The influence of tempering temperature on the flow stress at  $\gamma = 0.05$ .

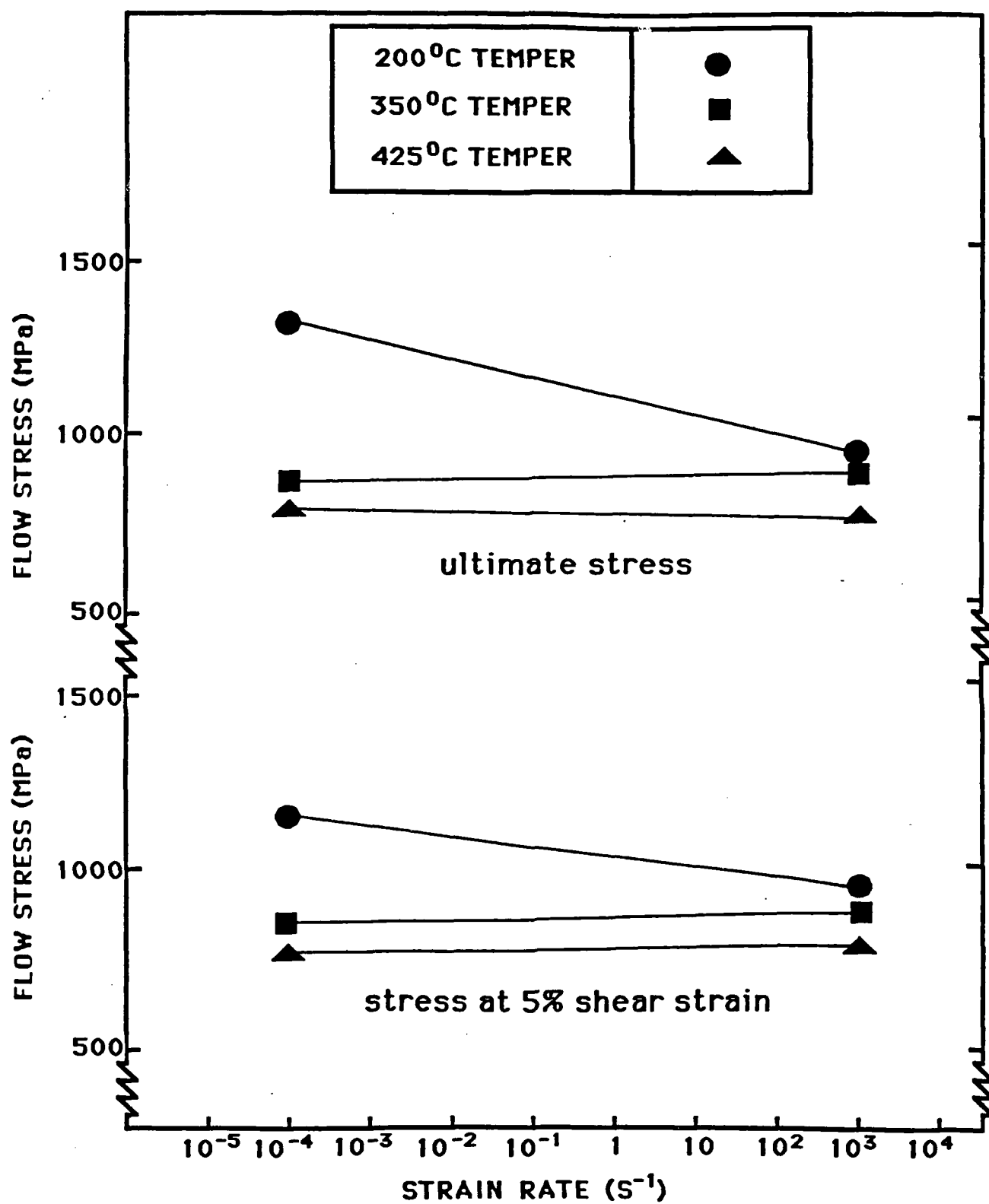


Fig. 16. The influence of strain rate on the flow stress in shear for 4340 VAR steel at +100°C.

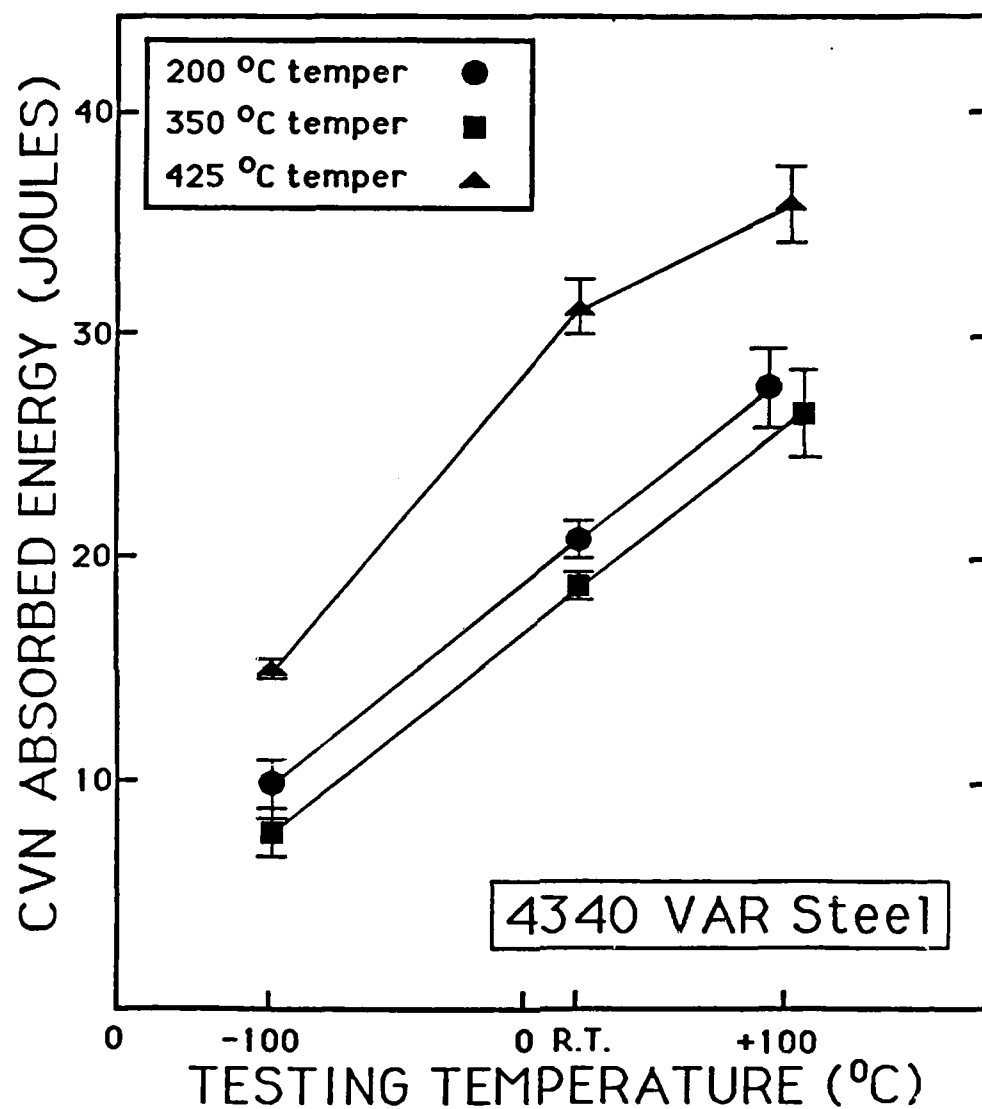


Fig. 17. Results of Charpy tests for the three different tempers as a function of testing temperature.

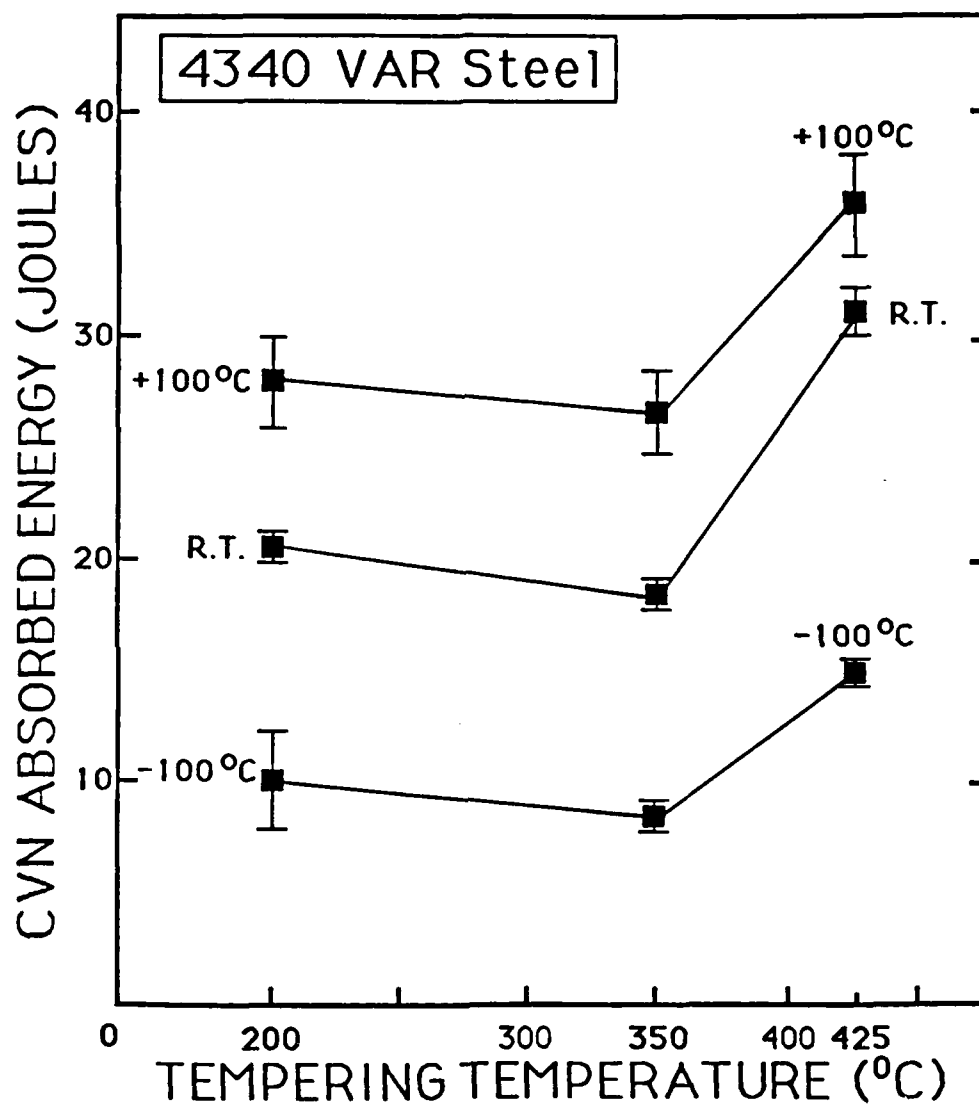


Fig. 18. Results of Charpy tests at three different testing temperatures as a function of tempering temperature.

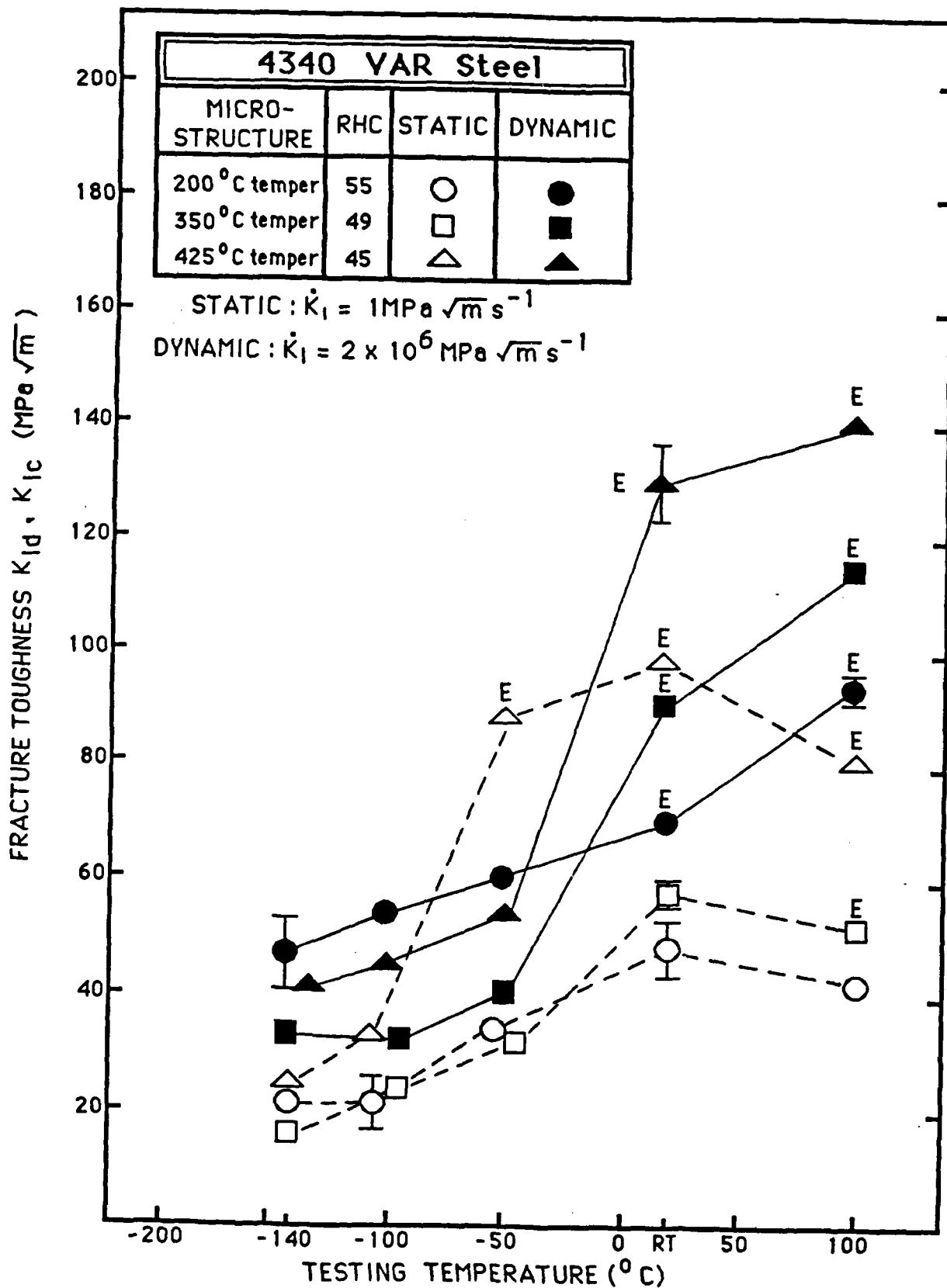


Fig. 19. Fracture toughness as a function of testing temperature for three different tempers of 4340 VAR steel. The letter E identifies those tests in which the ASTM criterion for a valid  $K_{Ic}$  test is not met and an equivalent  $K_{Ic}$  value is calculated using Equation (5).

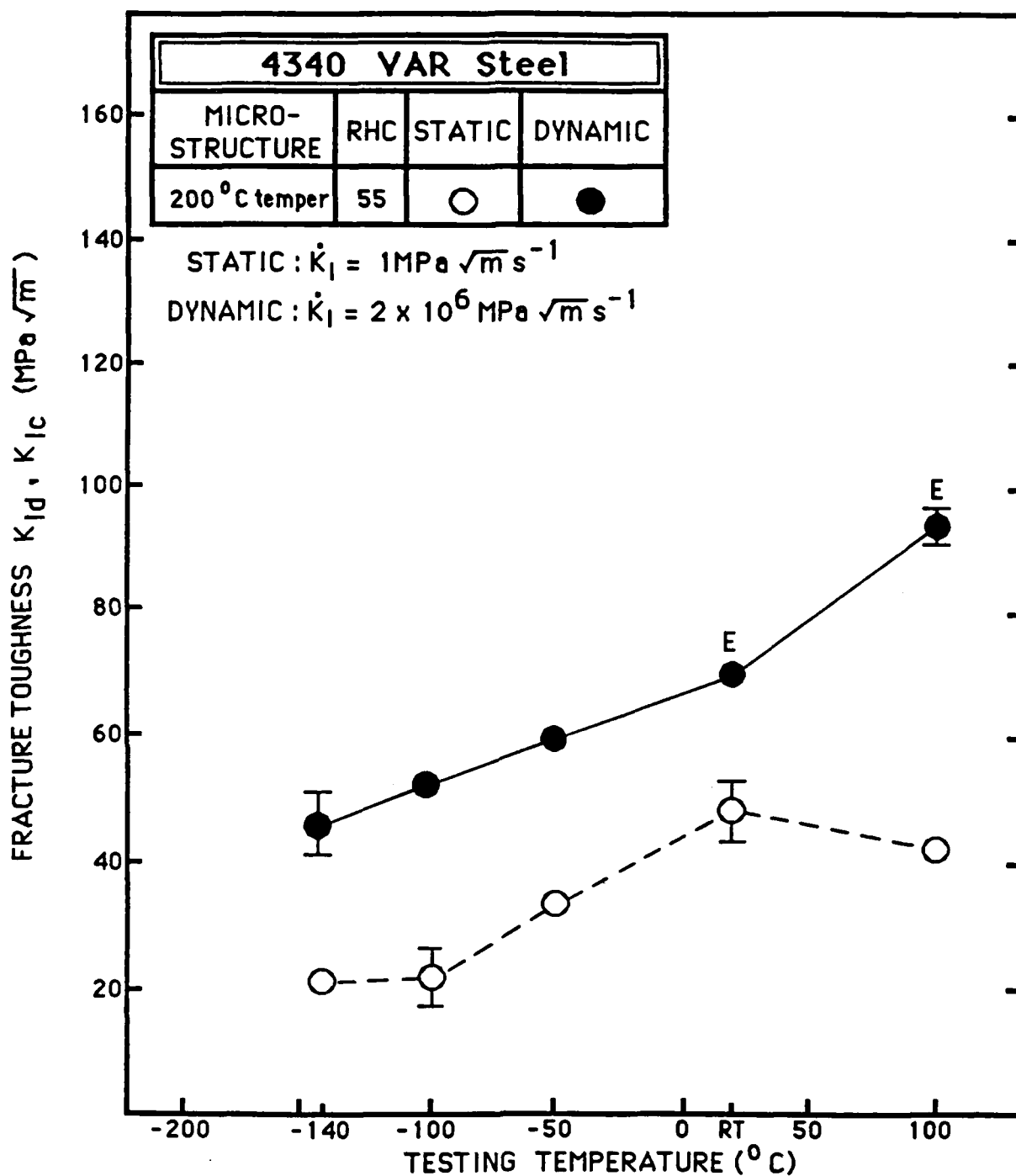


Fig. 20. Fracture toughness as a function of testing temperature for the 200° C temper (HRC=55). The letter E identifies those tests in which the ASTM criterion for a valid  $K_{Ic}$  test is not met and an equivalent  $K_{Ic}$  value is calculated using Equation (5).

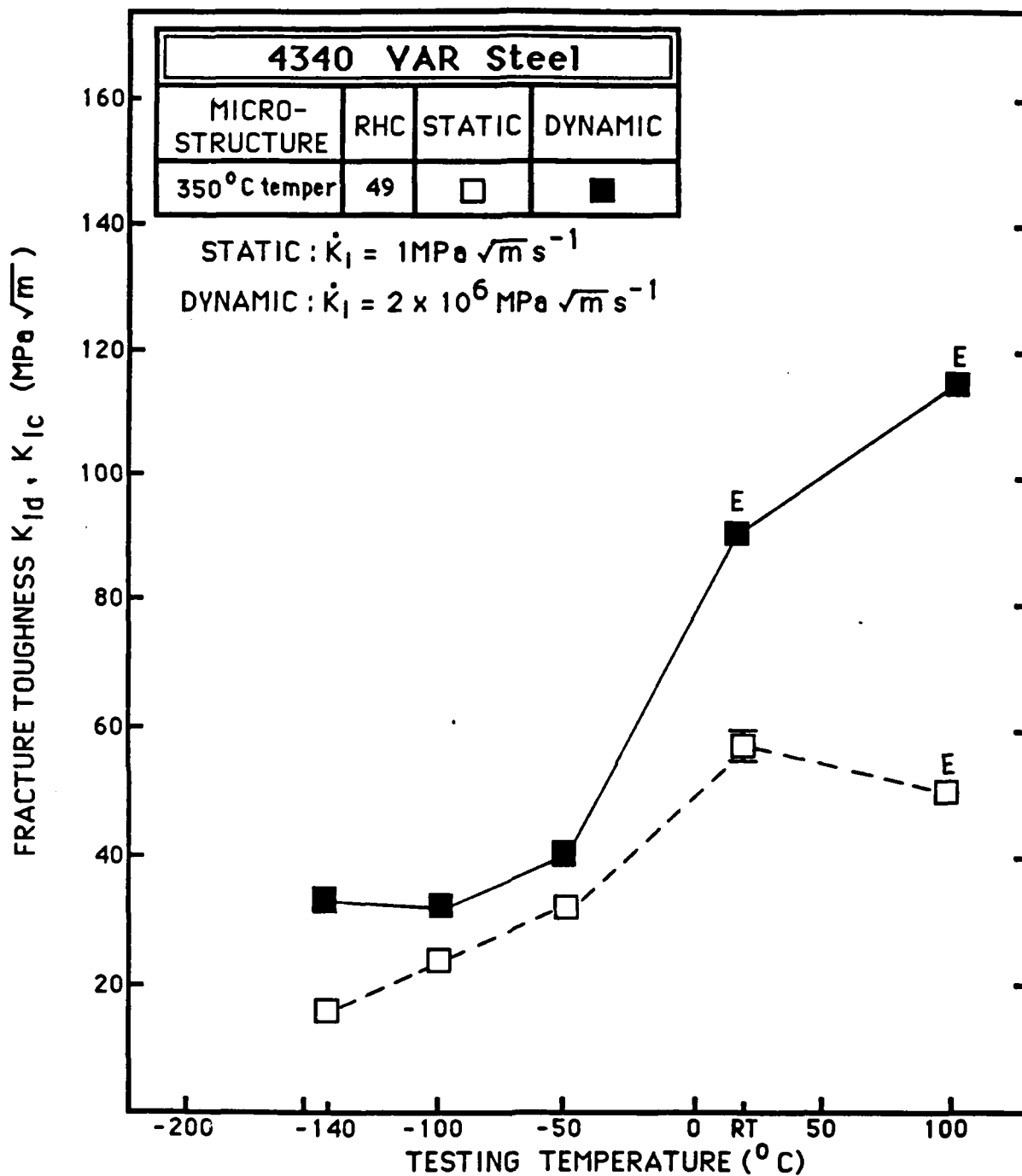


Fig. 21. Fracture toughness as a function of testing temperature for the 350° C temper (HRC=49). The letter E identifies those tests in which the ASTM criterion for a valid  $K_{Ic}$  test is not met and an equivalent  $K_{Ic}$  value is calculated using Equation (5).



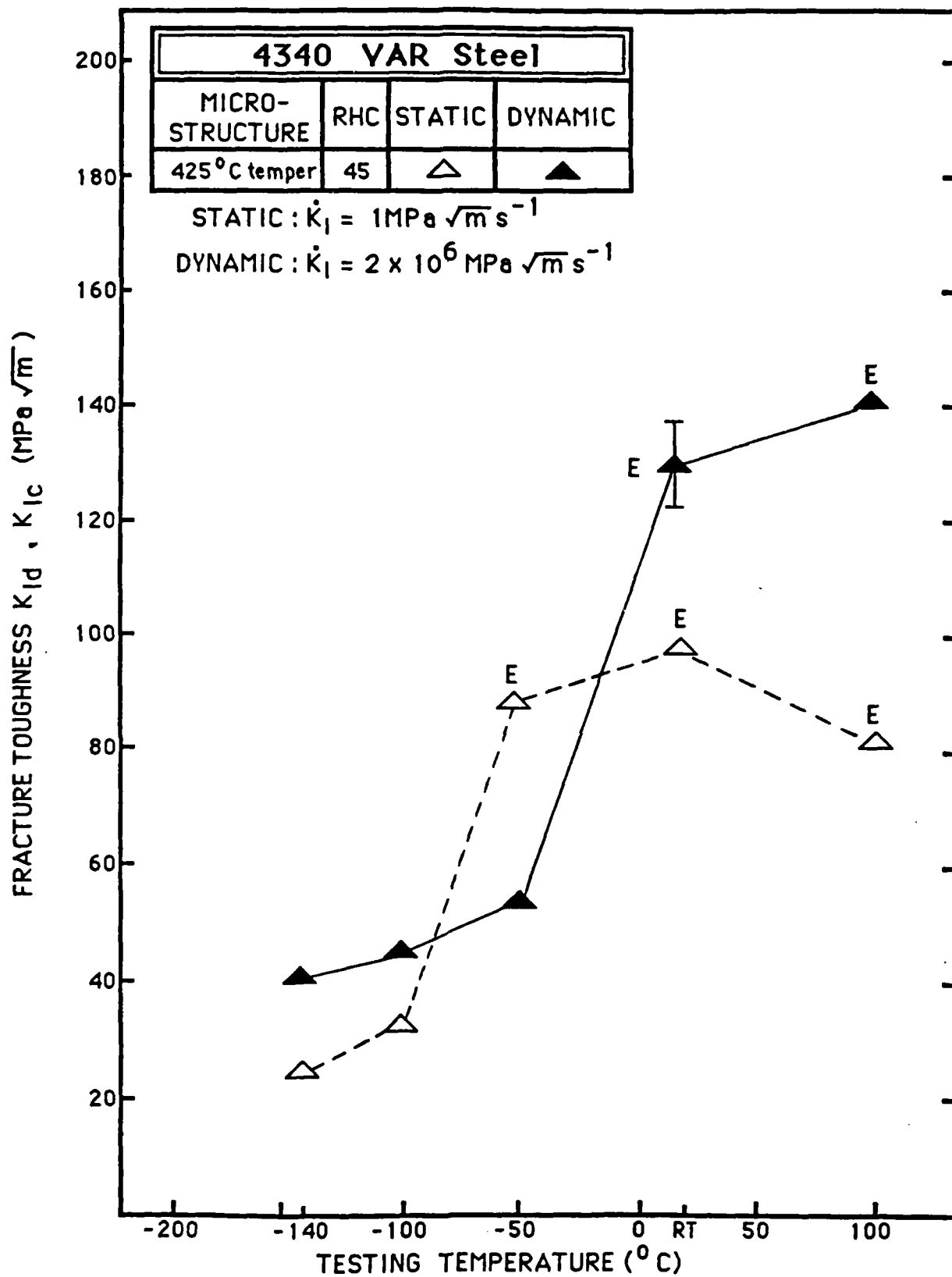


Fig. 22. Fracture toughness as a function of testing temperature for the 425° C temper (HRC=45). The letter E identifies those tests in which the ASTM criterion for a valid  $K_{Ic}$  test is not met and an equivalent  $K_{Ic}$  value is calculated using Equation (5).

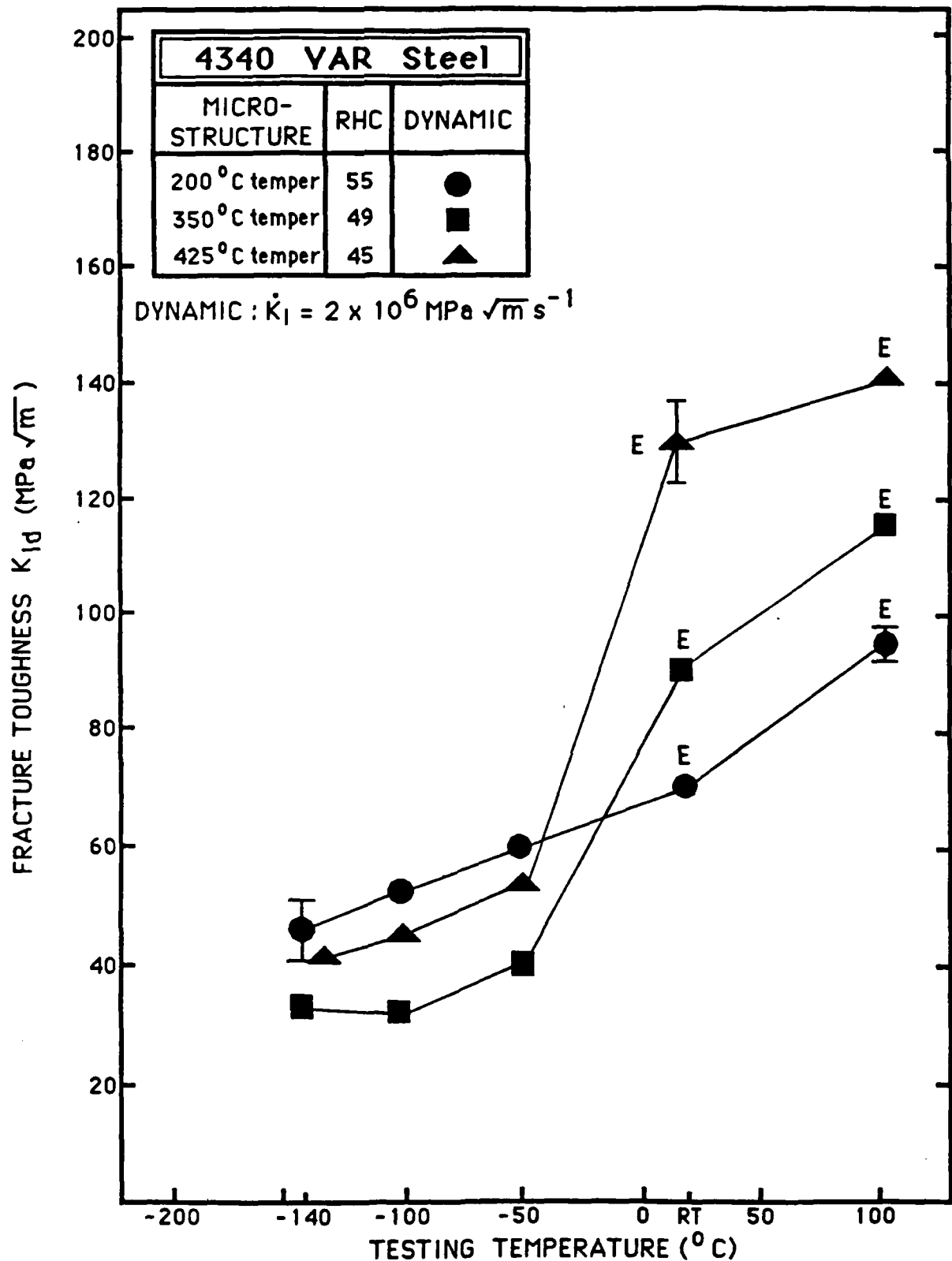


Fig. 23. Dynamic fracture toughness as a function of testing temperature for three different tempers of 4340 VAR steel. The letter E identifies those tests in which the ASTM criterion for a valid  $K_{Ic}$  test is not met and an equivalent  $K_{Ic}$  value is calculated using Equation (5).

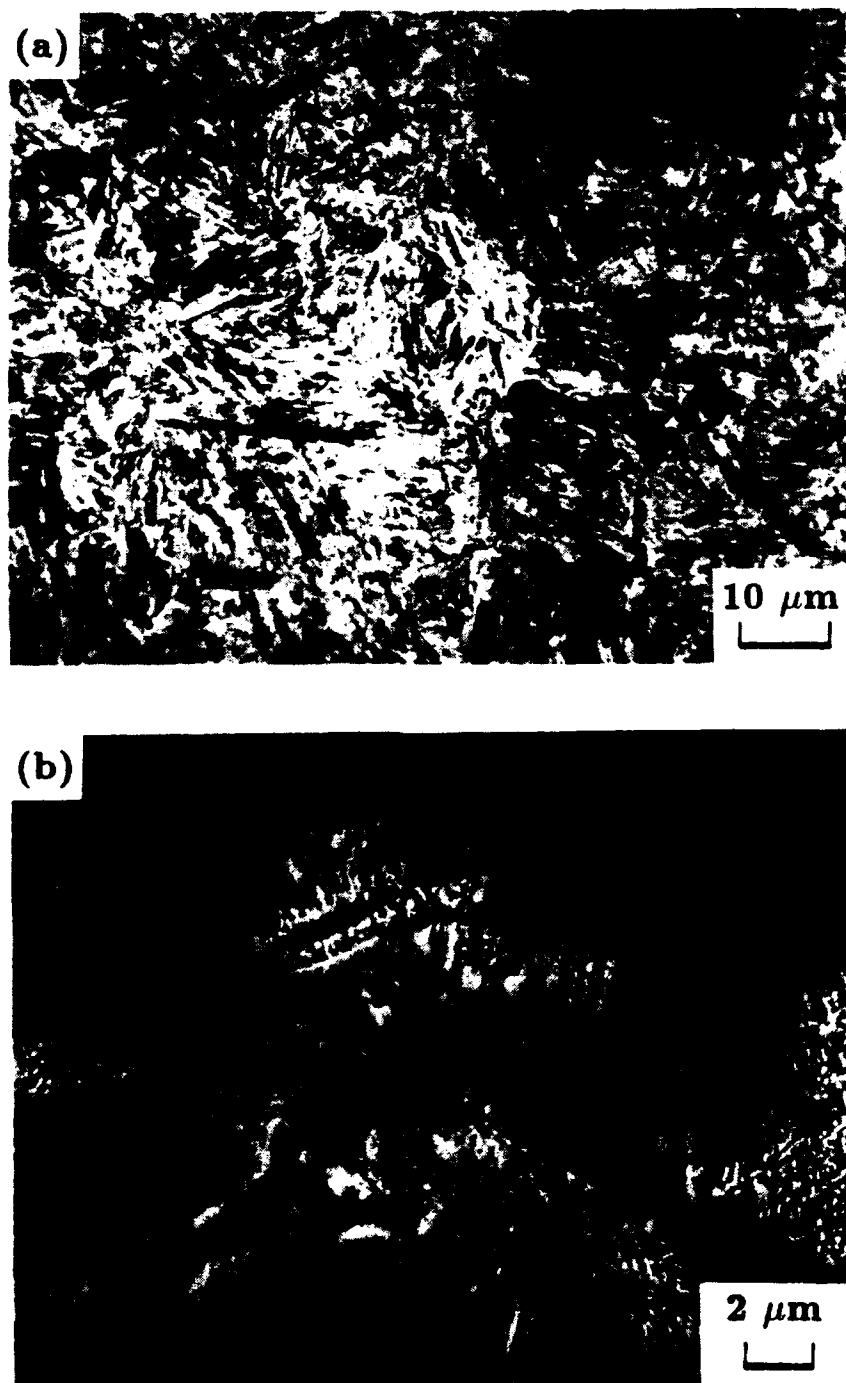


Fig. 24. (a). Optical micrograph of undeformed 4340 VAR steel tempered at 200° C (RHC=55) showing a tempered martensite with no evidence of upper bainite. (b). Scanning Electron micrograph reveals microcracks in upper bainite in the specimen examined by Godse et al.[25].

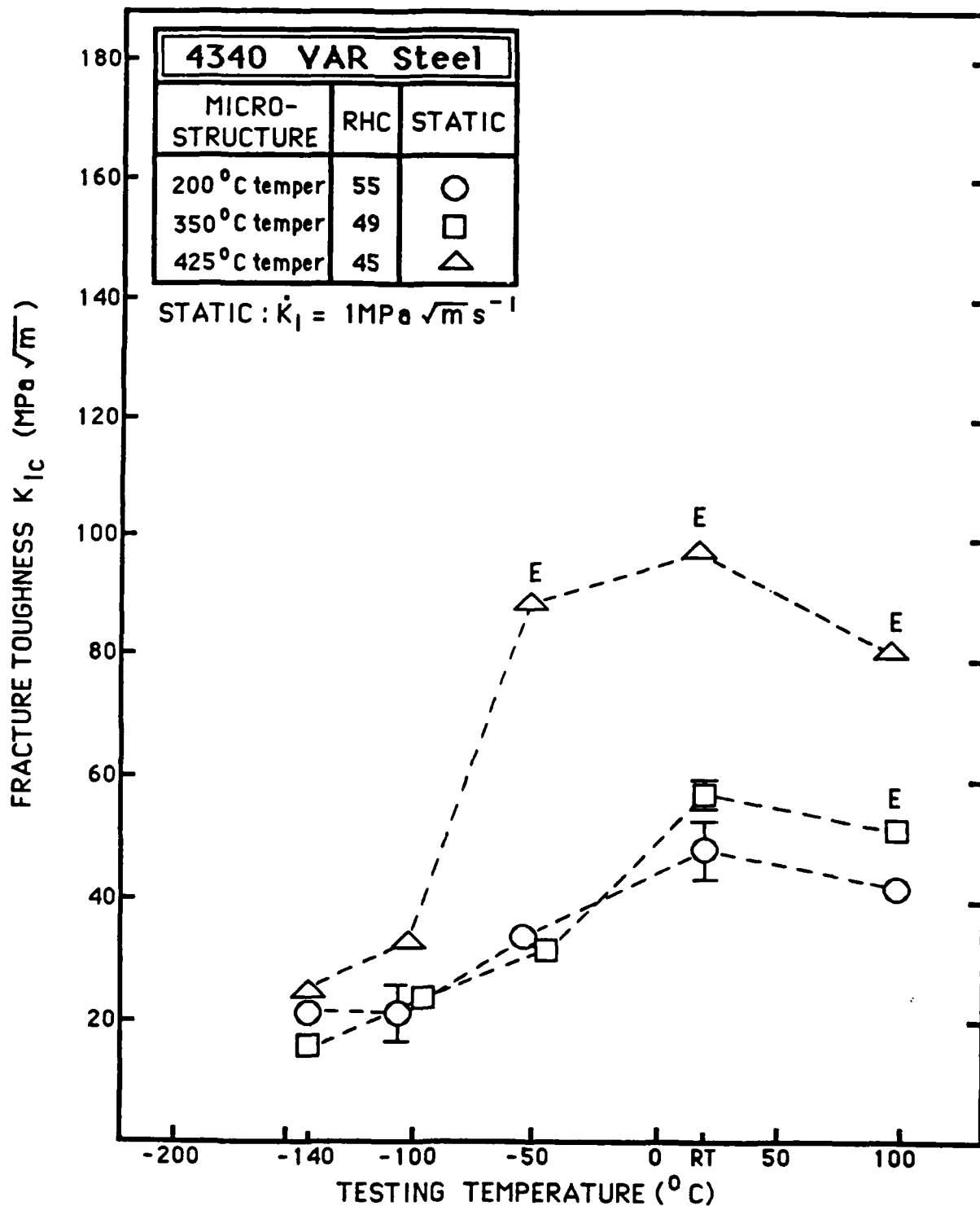
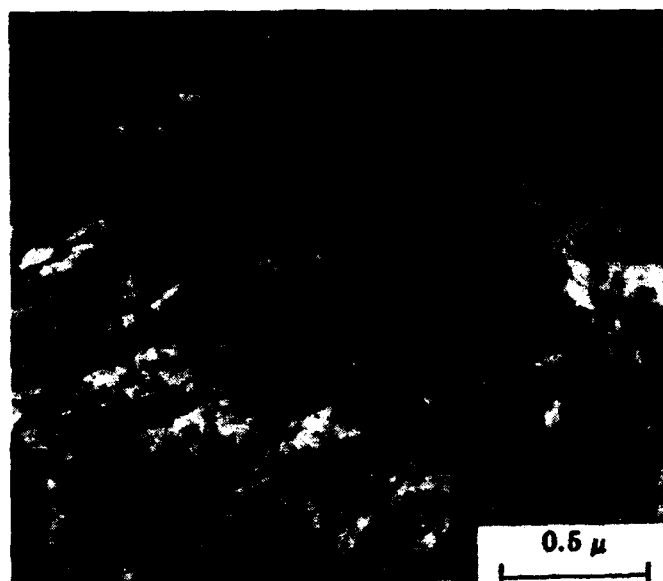


Fig. 25. Quasi-static fracture toughness as a function of testing temperature for three different tempers of 4340 VAR steel. The letter E identifies those tests in which the ASTM criterion for a valid  $K_{Ic}$  test is not met and an equivalent  $K_{Ic}$  value is calculated using Equation (5).

(a)



(b)

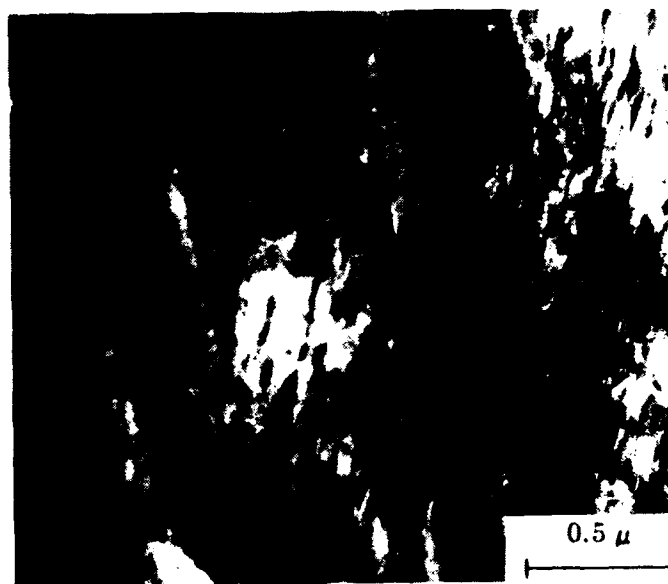


Fig. 26. Transmission electron micrographs of 4340 VAR steel tempered at 350° C (37500X).

(a) Cementites and carbide films at lath boundaries (b) Cementite precipitation on microtwins.

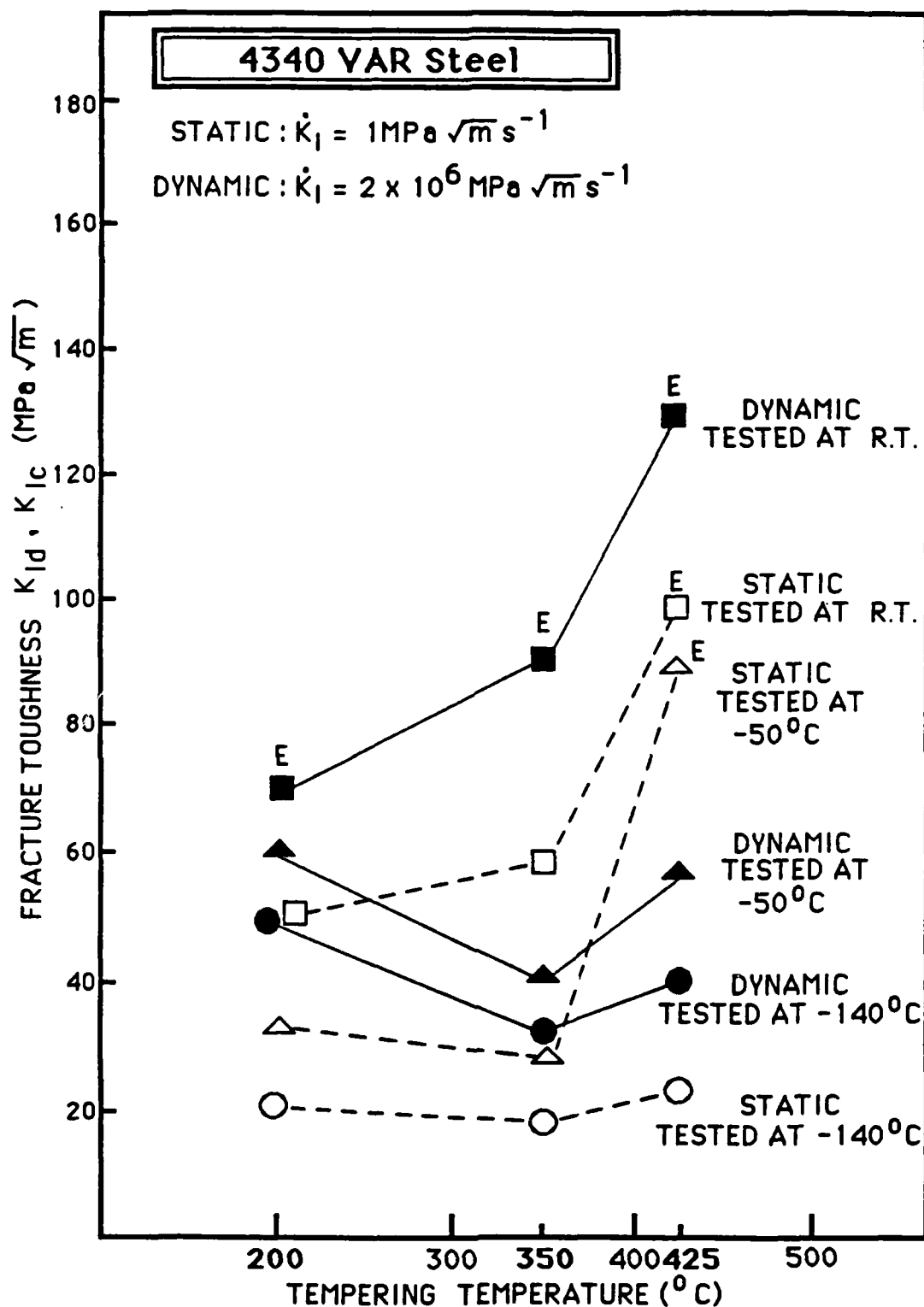


Fig. 27. Fracture toughness as a function of tempering temperature showing the effect of tempered martensite embrittlement (TME) in the steel tempered at 350° C (HRC=49). The letter E identifies those tests in which the ASTM criterion for a valid  $K_{Ic}$  test is not met and an equivalent  $K_{Ic}$  value is calculated using Equation (5).

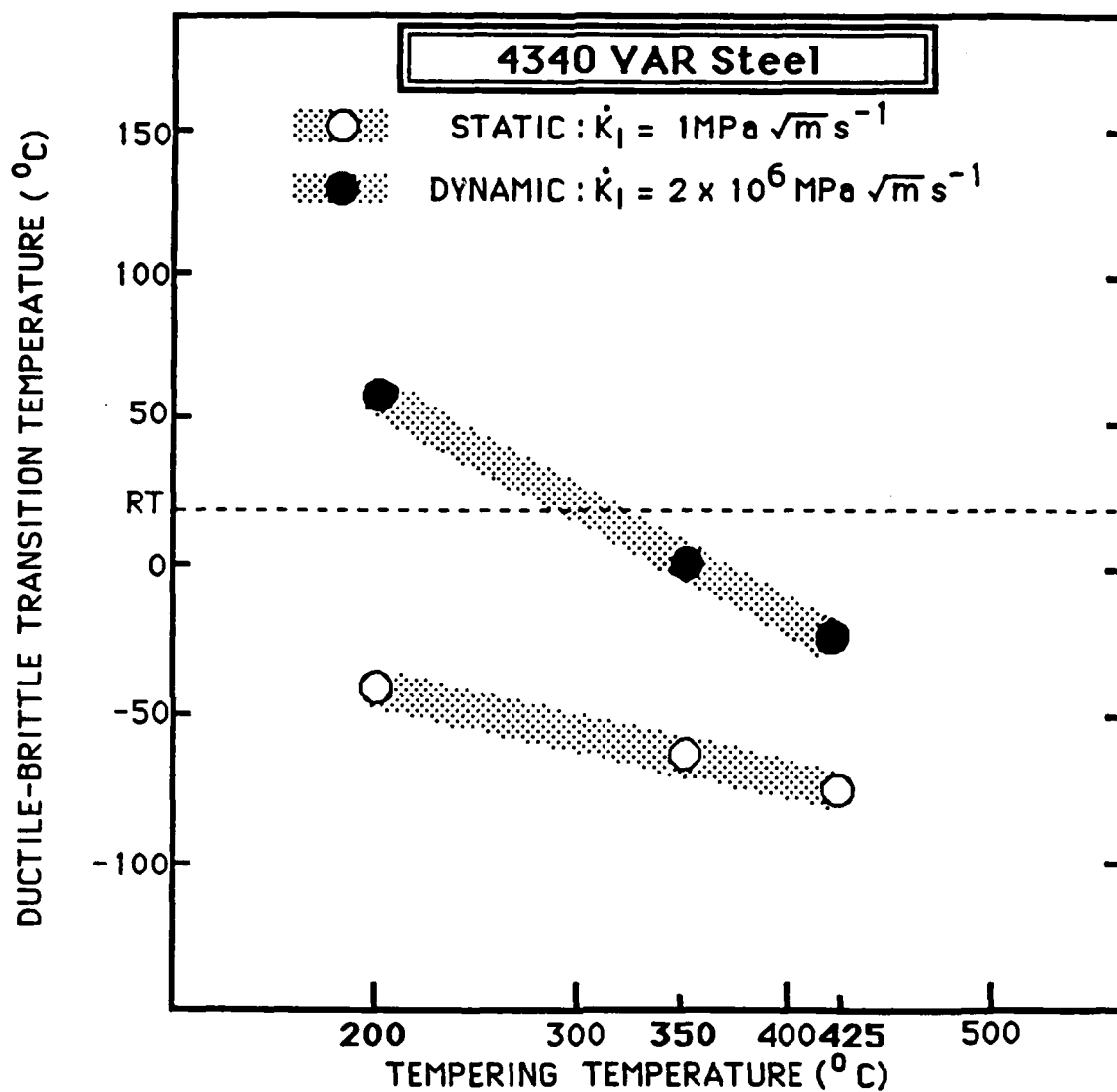
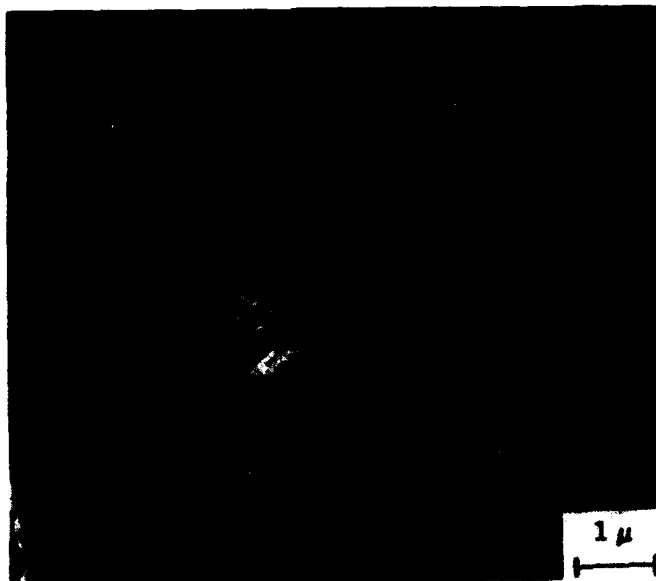


Fig. 28. The ductile-to-brittle transition temperature for the 4340 VAR steel as a function of tempering temperature as determined in the plane strain fracture initiation test.

(a)



(b)

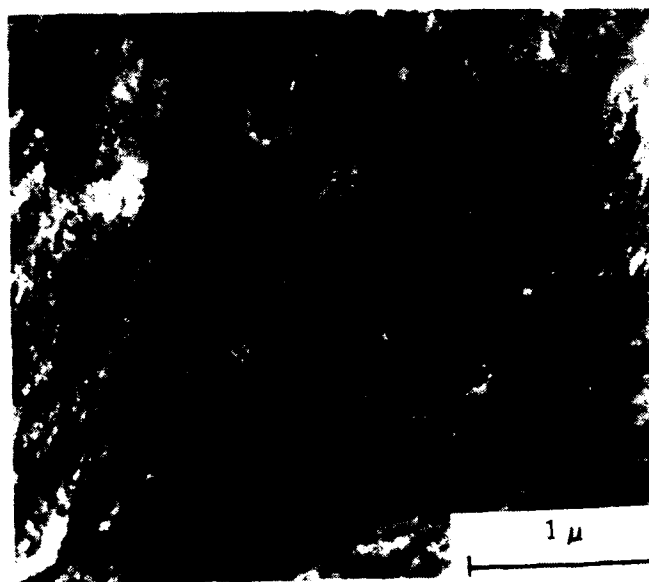


Fig. 29. Transmission electron micrographs of 4340 VAR steel tempered at 200° C, with magnification at (a) 10500X and (b) 24000X.



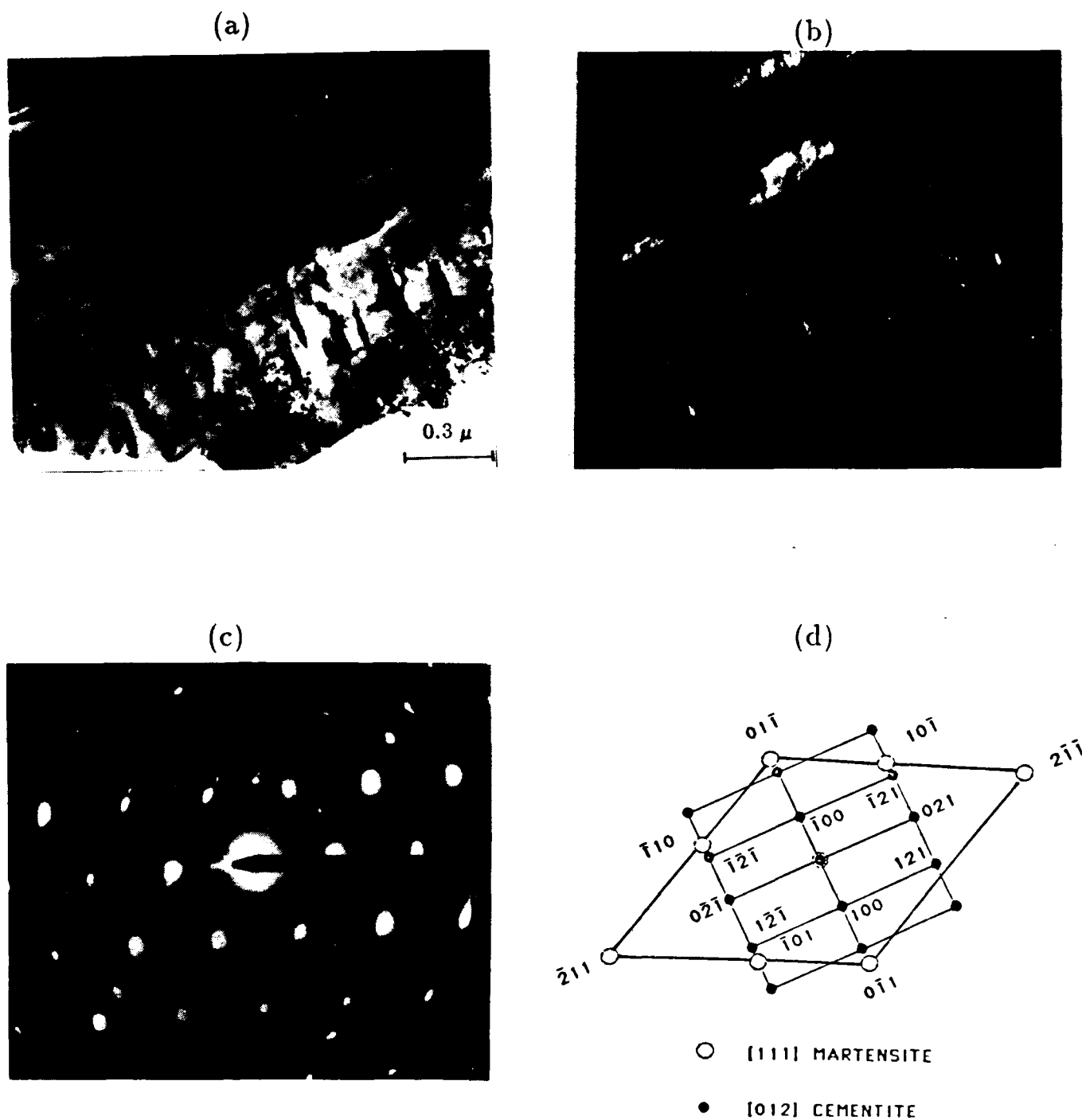
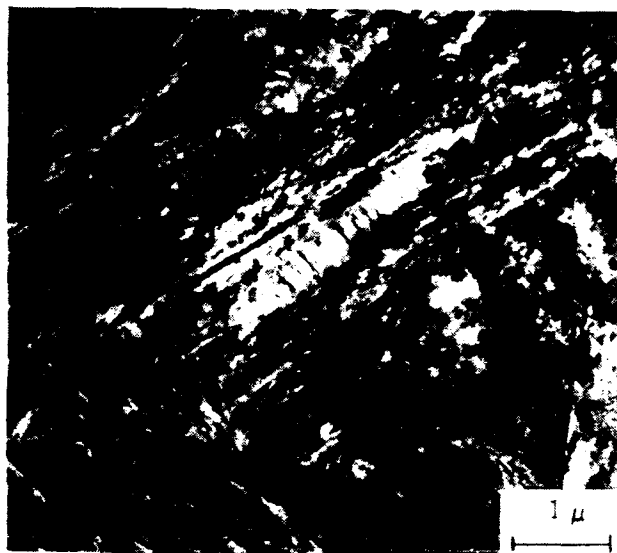


Fig. 30. Transmission electron micrographs of 4340 VAR steel tempered at 350° C. (a) bright field image (51000X), (b) dark field image (51000X), (c) selected area diffraction pattern from (a), (d) analysis of the selected area diffraction pattern in (c).

(a)



(b)

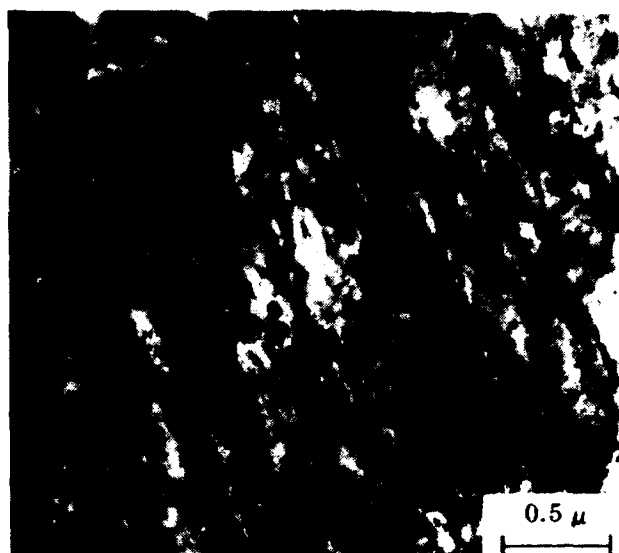
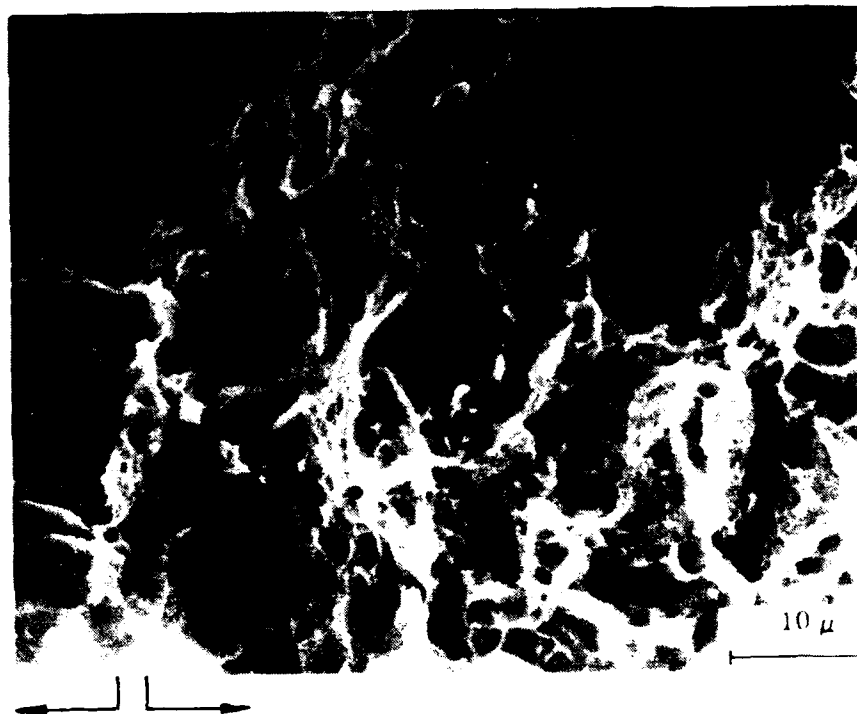
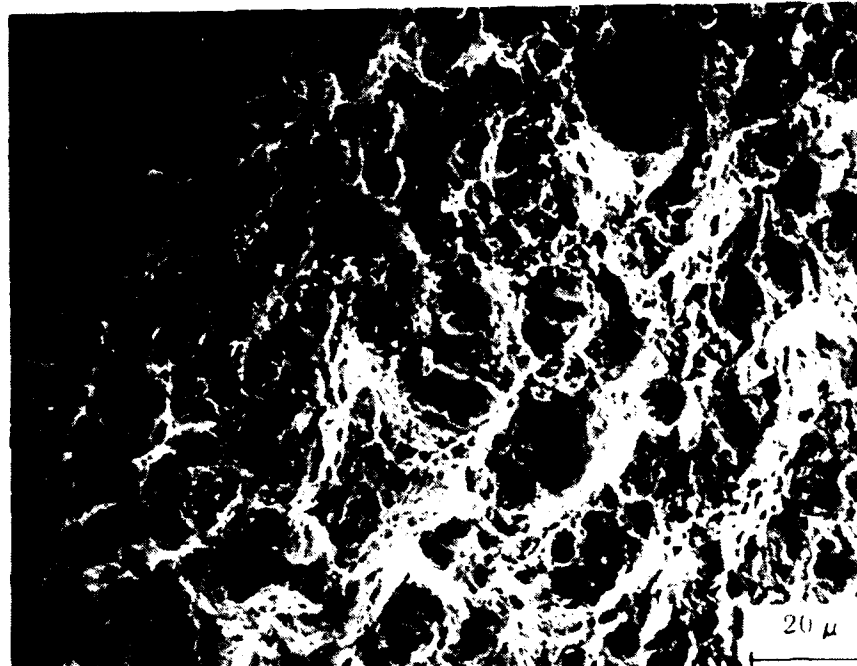


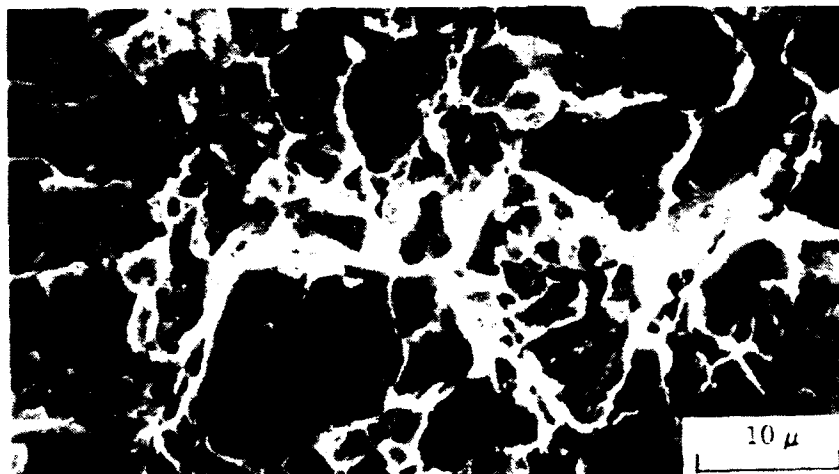
Fig. 31. Transmission electron micrographs of 4340 VAR steel tempered at 425° C, with magnification at (a)10500X and (b) 31000X.



**prefatigued crack fracture initiation zone**

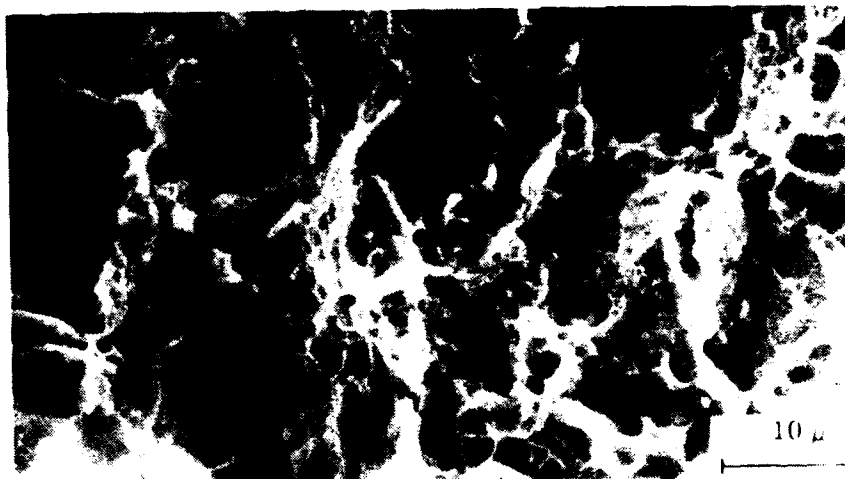
Fig. 32. The appearance of the fracture surface following plane strain fracture testing at room temperature under quasi-static loading. The 4340 VAR steel was tempered at 350° C.

(a)



VS 4-1 (200° C temper) static test at R.T.

(b)



VS 77-3 (350° C temper) static test at R.T.

(c)



VS 70-2 (425° C temper) static test at R.T.

Fig. 33. The appearance of the fracture surface following plane strain fracture testing at room temperature under quasi-static loading. The 4340 VAR steel was tempered at (a) 200° C, (b) 350° C, and (c) 425° C.

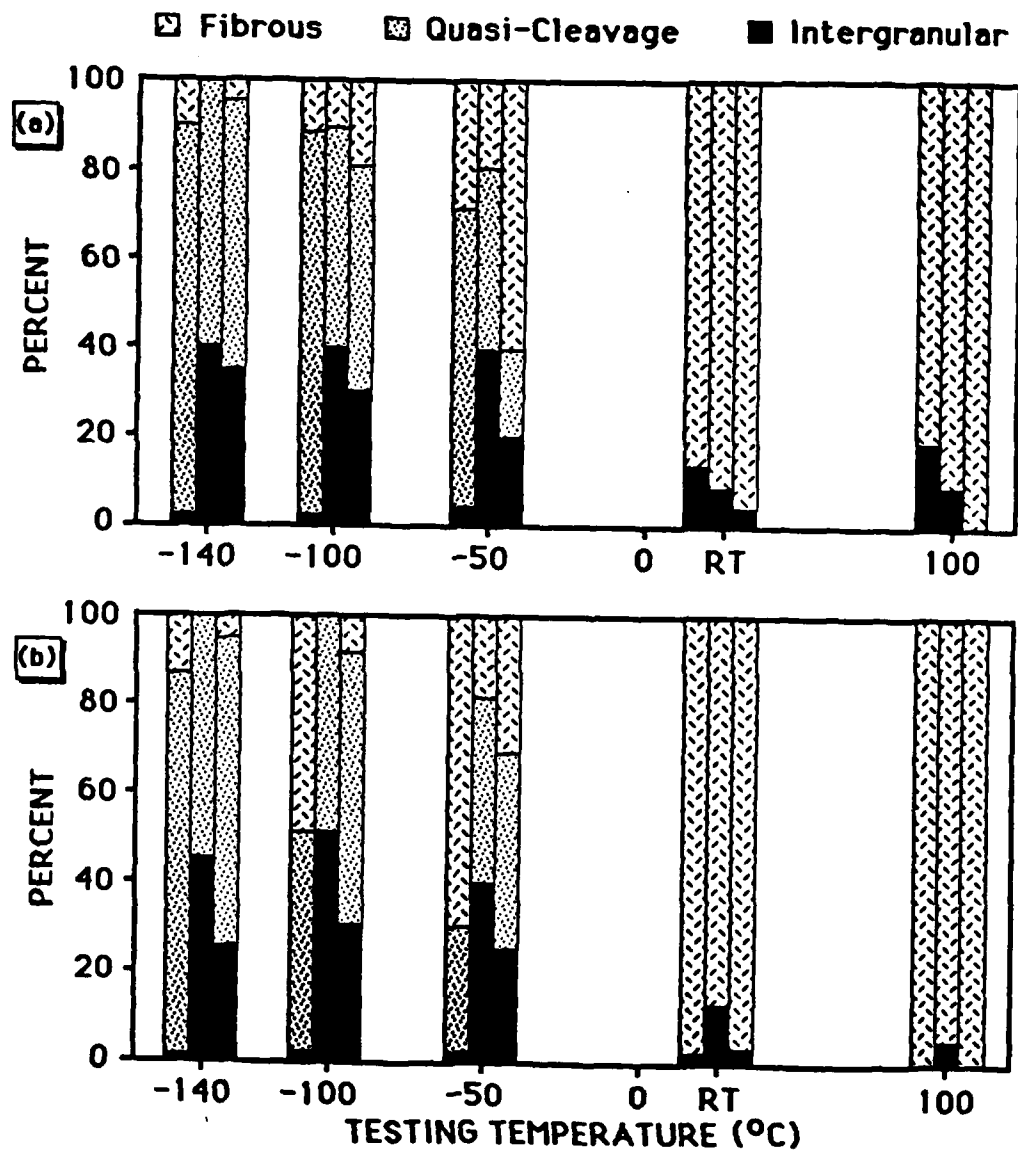


Fig. 34. Bargraphs giving the percentage of each fracture initiation mode as determined by SEM. At each test temperature, the first bar corresponds to the 200° C temper, the second bar to the 350° C, and the third bar to the 425° C temper. (a) represents quasi-static loading, and (b) dynamic loading.

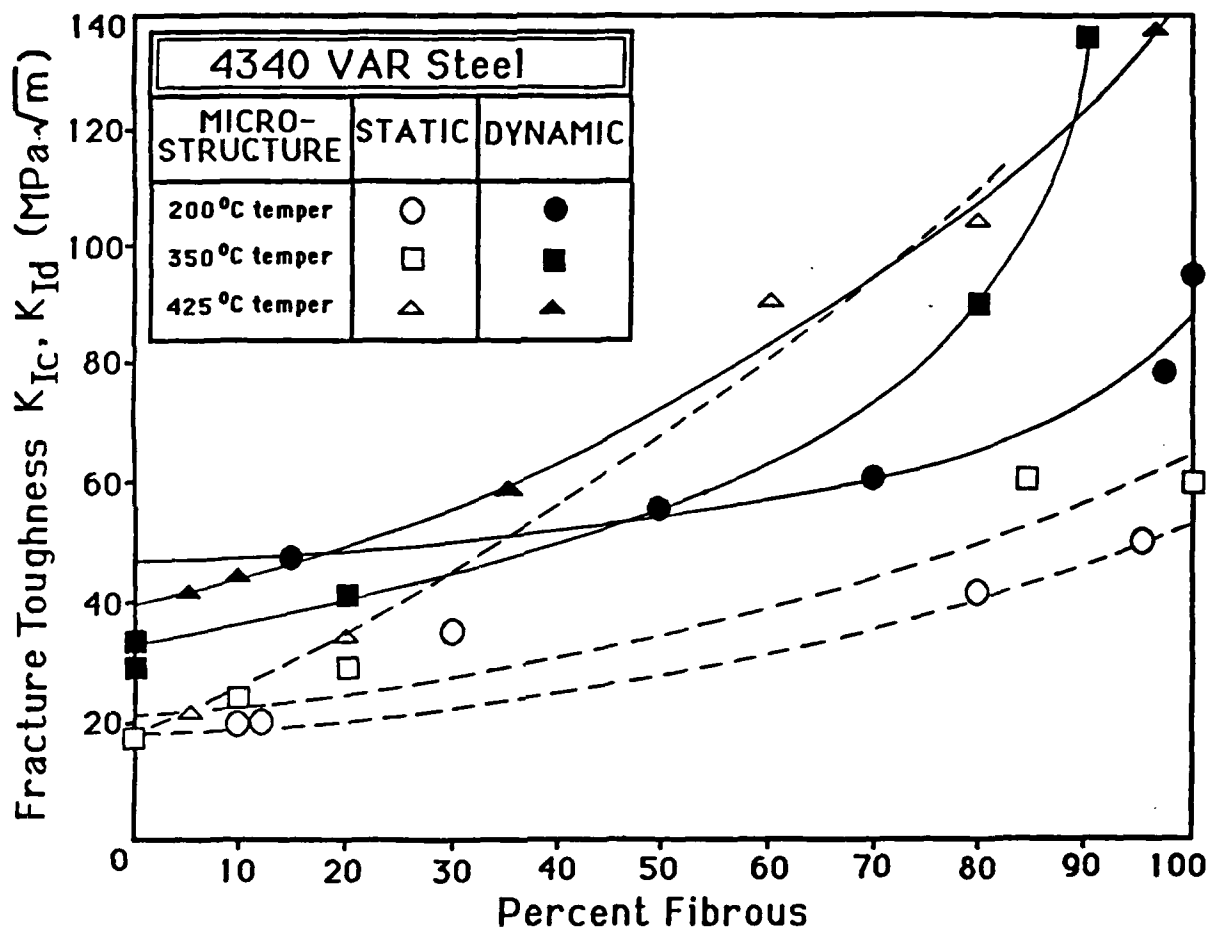
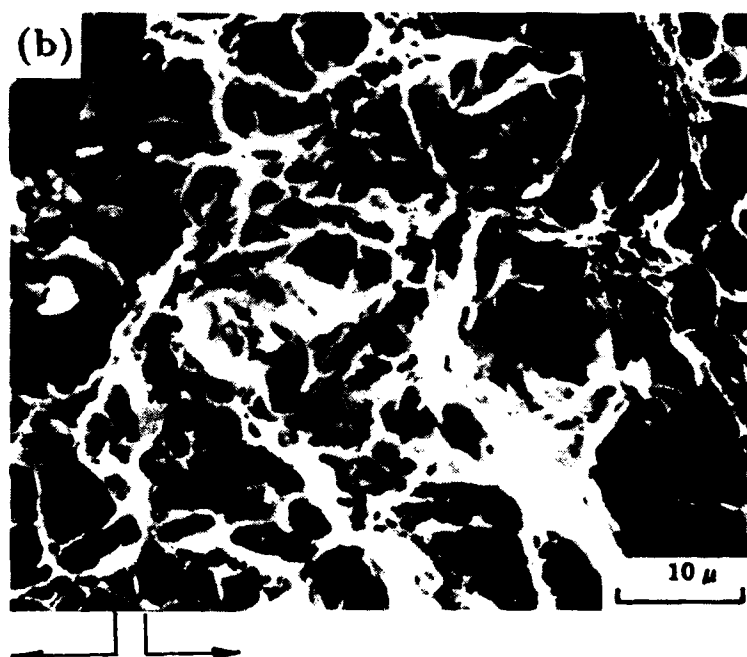
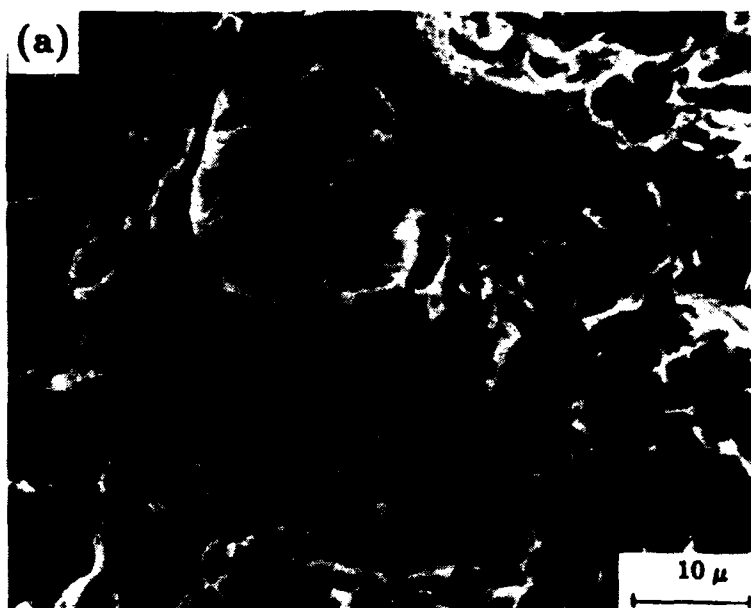


Fig. 35. The fracture toughness as a function of percent fibrous mode of fracture initiation for three different tempers.



← prefatigued crack fracture initiation zone →

Fig. 36. The appearance of the fracture surface following plane strain fracture testing at  $-140^{\circ}\text{C}$  under dynamic loading. The 4340 VAR steel was tempered at (a)  $350^{\circ}\text{C}$  and (b)  $200^{\circ}\text{C}$ .

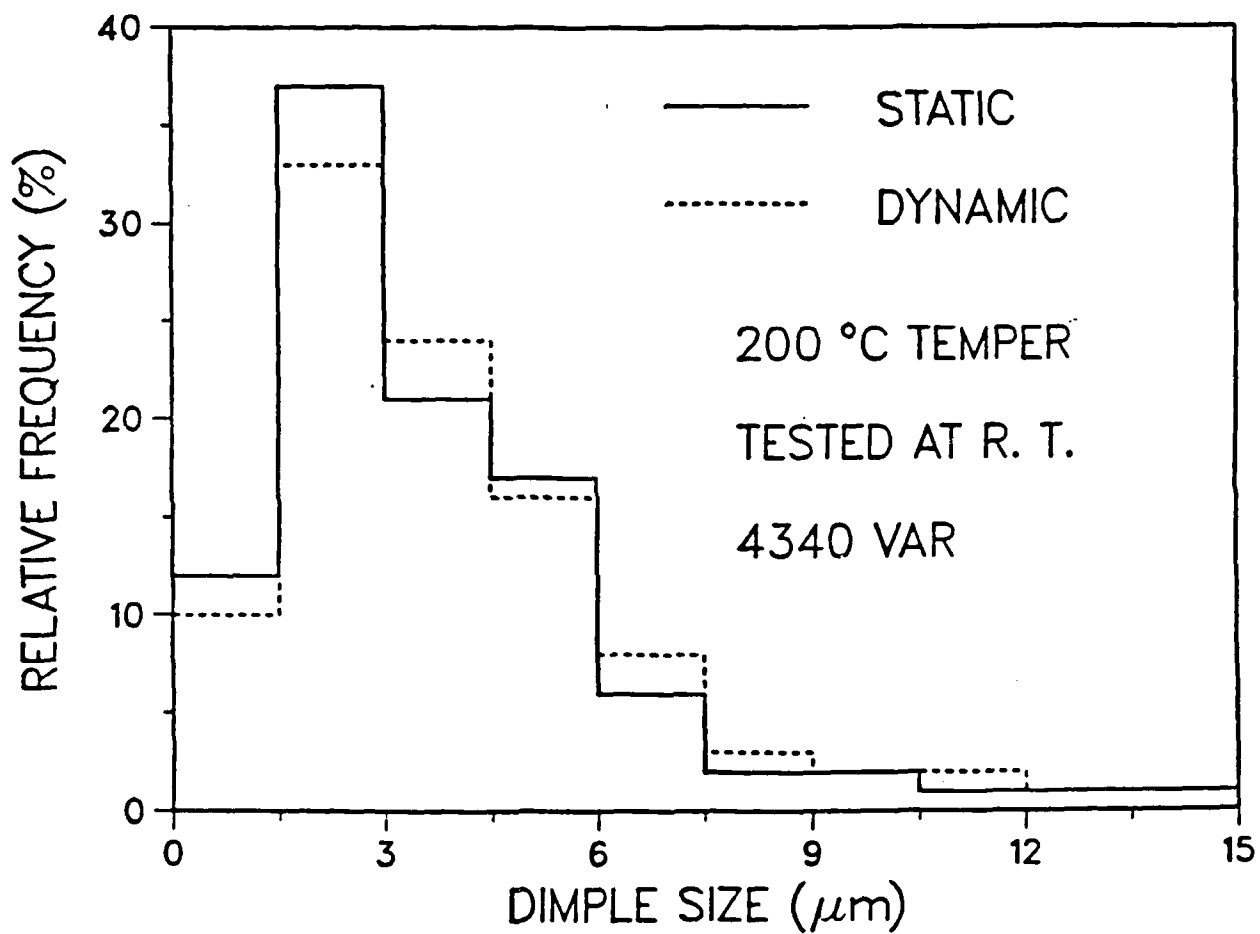


Fig. 37. Relative frequencies of dimple sizes for the 200 C temper when tested at room temperature.



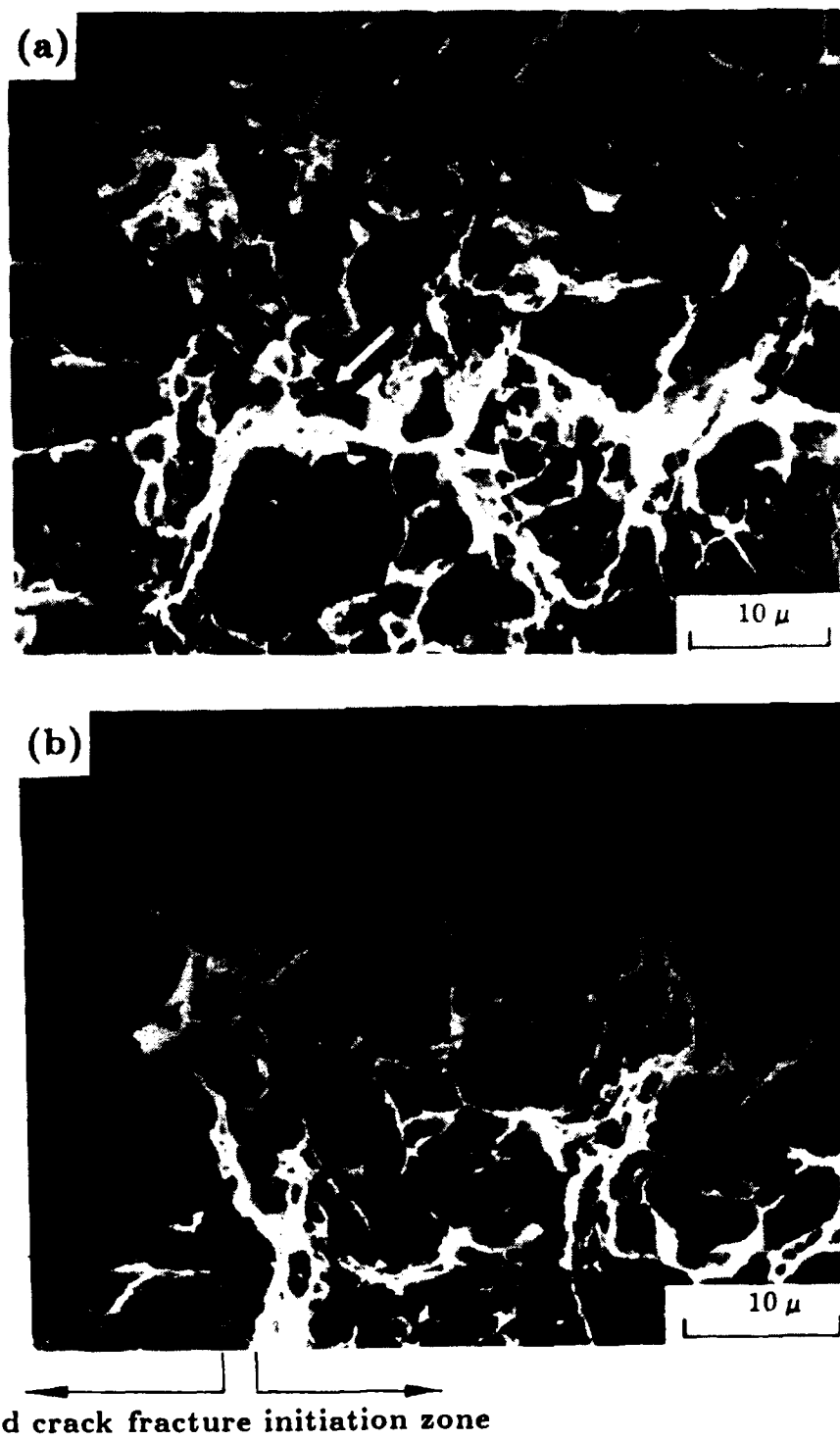


Fig. 38. The appearance of the fracture surface following plane strain fracture testing at room temperature under (a) quasi-static loading and (b) dynamic loading. The 4340 VAR steel was tempered at 200° C. Note the presence of MnS inclusions inside dimples indicated by an arrow.

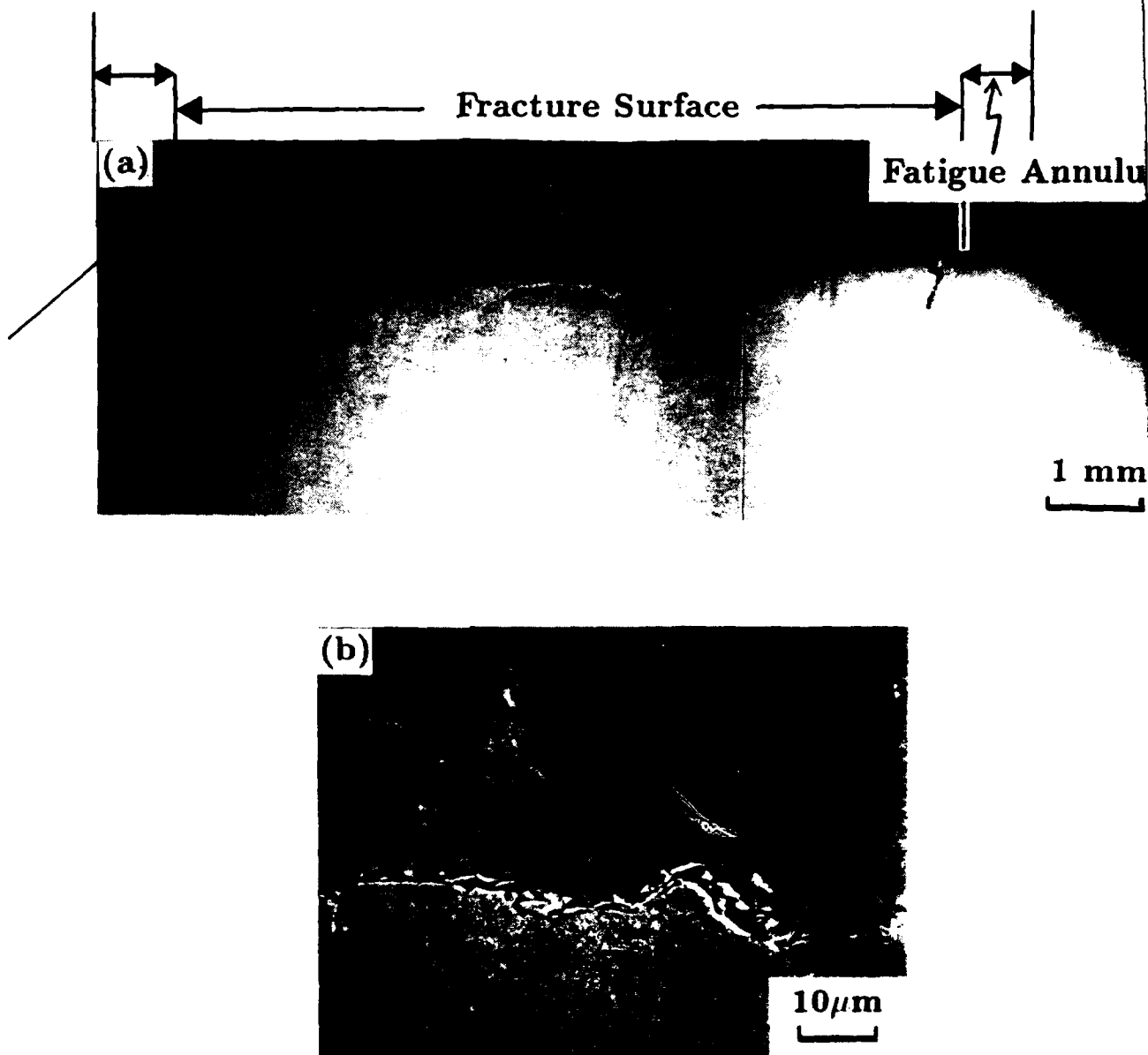


Fig. 39. (a). Optical micrograph of the 200° C temper dynamic specimen tested at room temperature showing internal secondary microcracks under the fracture surface. (b). The microcracks surrounding the prior austenite grains at the tip of the crack shown in (a).

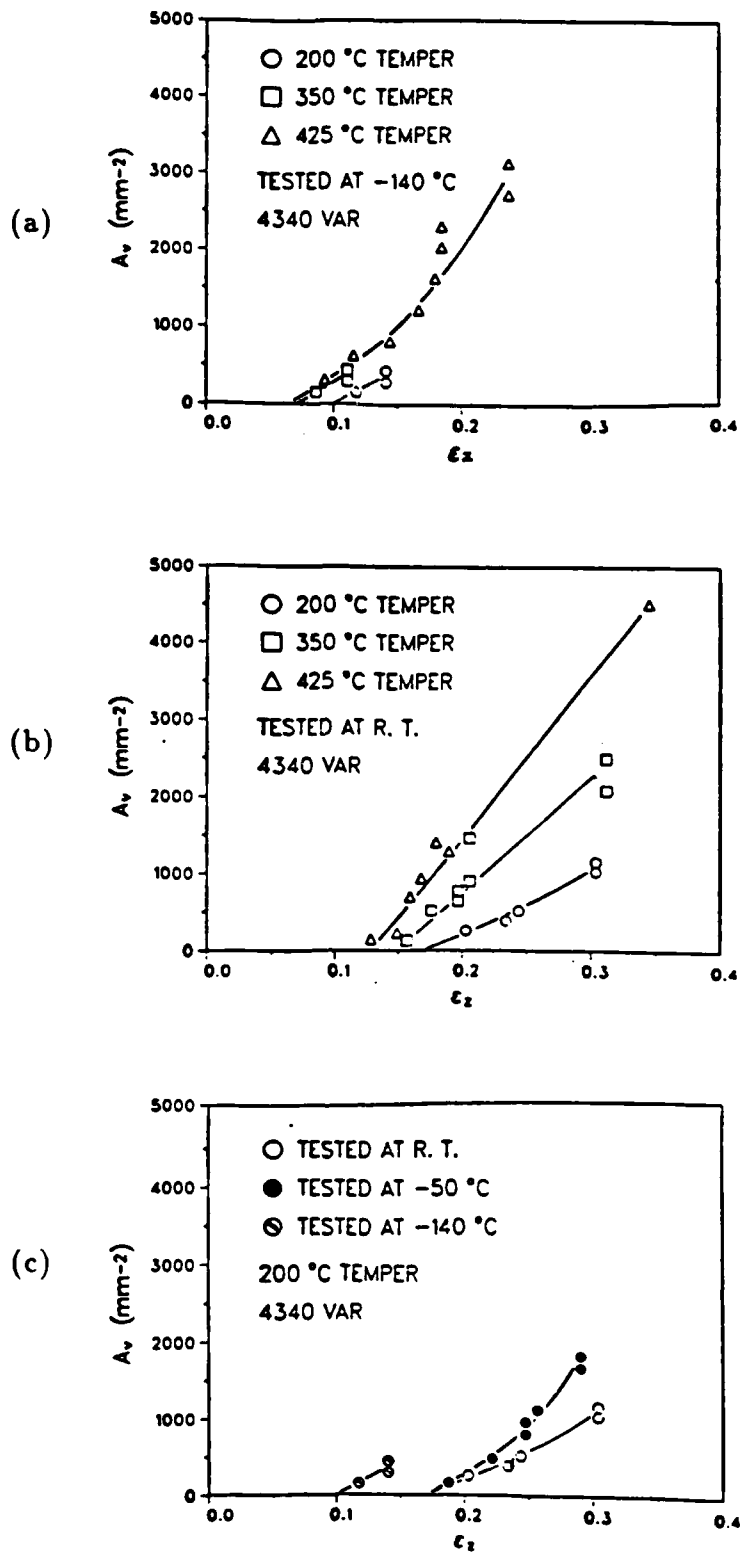


Fig. 40. Areal density of voids associated with submicron carbide particles ( $A_v$ ) versus true strain ( $\epsilon_z$ ) in the notched tensile specimens shown in Fig. 8. The test temperatures are as follows: (a)  $-140^\circ\text{C}$ , (b) room temperature, and (c) room temperature,  $-50^\circ\text{C}$ , and  $-140^\circ\text{C}$ .